

AD-A231 964

REPORT DOCUMENTATION PAGE			Form Approved OMB No. 0704-0188	
<small>Public reporting burden for this collection of information is estimated to average 1 hour per response, including the time for reviewing instructions, searching existing data sources, gathering and maintaining the data needed, and completing and reviewing the collection of information. Send comments regarding this burden estimate or any other aspect of this collection of information, including suggestions for reducing this burden, to Washington Headquarters Services, Directorate for Information Operations and Reports, 1215 Jefferson Davis Highway, Suite 1204, Arlington, VA 22202-4302, and to the Office of Management and Budget, Paperwork Reduction Project (0704-0188), Washington, DC 20503.</small>				
1. AGENCY USE ONLY (Leave blank)		2. REPORT DATE 9/31/90		3. REPORT TYPE AND DATES COVERED Final 1 Oct 87 - 30 Sep 90
4. TITLE AND SUBTITLE "Effect of Transversely Low-Velocity Impact on Graphite/ Epoxy Laminated Composites"			5. FUNDING NUMBERS DAAL 03-87-15 0115	
6. AUTHOR(S) Hyung-Yun Choi and Fu-Kuo Chang			DTIC ELECTE	
7. PERFORMING ORGANIZATION NAME(S) AND ADDRESS(ES) Department of Aeronautics and Astronautics Stanford University, Stanford, CA 94305-4035			8. PERFORMING ORGANIZATION REPORT NUMBER	
9. SPONSORING / MONITORING AGENCY NAME(S) AND ADDRESS(ES) U. S. Army Research Office P. O. Box 12211 Research Triangle Park, NC 27709-2211			10. SPONSORING / MONITORING AGENCY REPORT NUMBER ARO 24538.5-EG	
11. SUPPLEMENTARY NOTES The view, opinions and/or findings contained in this report are those of the author(s) and should not be construed as an official Department of the Army position, policy, or decision, unless so designated by other documentation.				
12a. DISTRIBUTION / AVAILABILITY STATEMENT Approved for public release; distribution unlimited.			12b. DISTRIBUTION CODE	
13. ABSTRACT (Maximum 200 words) <p>An investigation was performed to study the damage in Graphite/Epoxy laminated composites resulting from transversely low-velocity impact. Matrix cracking and delaminations were the primary concern of the study. This research was divided into two sequential steps: (1) characterization of impact damage, and (2) development of an analytical model for estimating impact damage in composites.</p> <p>A unique impact tester was developed for the study. The major characteristic of the tester is the design of a rectangular barrel so that the impactor can be designed in two parts: a nose and a base. Accordingly, different types of impact damage can be produced by appropriately selecting the nose shape of the impactor.</p> <p>Both line-nosed and point-nosed impactors were selected for the study. The use of line-nosed impactors can considerably simplify impact damage from a complicated three-dimensional pattern to a two-dimensional one. As a result, both experiments and analysis on line-loading impact were performed for characterizing impact damage in composites. Based on the knowledge gained from the line-loading impact study, a model was developed for estimating the extent of impact damage in laminated composites resulting from point-nosed impact. Point-loading impact experiments were also conducted to verify the model. A user-friendly computer code designated as "3DIMPACT" was developed based on the model for predicting point-loading impact damage in laminated composites.</p>				
14. SUBJECT TERMS Composite Materials; Impact Damage; Matrix Cracking; Delaminations			15. NUMBER OF PAGES 173	
			16. PRICE CODE	
17. SECURITY CLASSIFICATION OF REPORT UNCLASSIFIED	18. SECURITY CLASSIFICATION OF THIS PAGE UNCLASSIFIED	19. SECURITY CLASSIFICATION OF ABSTRACT UNCLASSIFIED	20. LIMITATION OF ABSTRACT UL	

**EFFECT OF TRANSVERSELY LOW-VELOCITY IMPACT ON
GRAPHITE/EPOXY LAMINATED COMPOSITES**

FINAL REPORT

**BY
HYUNG-YUN CHOI AND FU-KUO CHANG**

SEPTEMBER 31, 1990

U.S. ARMY RESEARCH OFFICE

CONTRACT: DAAL03-87-K-0115

STANFORD UNIVERSITY

**APPROVED FOR PUBLIC RELEASE;
DISTRIBUTION UNLIMITED.**

Accession For	
NTIS GRA&I	<input checked="" type="checkbox"/>
DTIC TAB	<input type="checkbox"/>
Unannounced	<input type="checkbox"/>
Justification	
By	
Distribution /	
Availability Codes	
Dist	Availability / or Special
A-1	

THE VIEW, OPINIONS, AND/OR FINDINGS CONTAINED IN THIS REPORT ARE THOSE OF THE AUTHOR(S) AND SHOULD NOT BE CONSTRUED AS AN OFFICIAL DEPARTMENT OF THE ARMY POSITION, POLICY, OR DECISION, UNLESS SO DESIGNATED BY OTHER DOCUMENTATION.

CONTENTS

TABLE OF CONTENTS	i
LIST OF TABLES	v
LIST OF FIGURES	vi
1 INTRODUCTION	1
2 METHOD OF APPROACH	4
2.1 THE OBJECTIVES	4
2.2 THE MAJOR TASKS	5
2.2.1 Generation of Simplified 2-Dimensional Impact Test Data	5
2.2.2 Analysis of Simplified 2-Dimensional Impact Test Data	6
2.2.3 Development of Point-nose Impact Damage Model	6

3	2-DIMENSIONAL LINE-LOADING IMPACT EXPERIMENT	7
3.1	INTRODUCTION	7
3.2	A NEW IMPACT TESTER	8
3.3	EXPERIMENTS	11
3.4	EXPERIMENTAL RESULTS	13
3.4.1	Matrix Cracks and Delaminations	13
3.4.2	Impact Energy Threshold	25
3.4.3	Pre-existing Micro-cracks Due to Thermal Residual Stresses	29
3.5	CONCLUSION	31
4	2-DIMENSIONAL LINE-LOADING IMPACT ANALYSIS	33
4.1	INTRODUCTION	33
4.2	STATEMENT OF PROBLEM	34
4.3	ANALYSIS	34
4.3.1	Stress Analysis	35
4.3.2	Finite Element Formulation	37
4.3.3	Failure Analysis	47
4.4	VERIFICATION	52
4.5	COMPARISON	55
4.5.1	Initial Impact Damage	55

4.5.2	Impact Energy Threshold	68
4.5.3	Delamination and Micro-cracks	70
4.6	CONCLUSION	75
5	EFFECTS OF IMPACT PARAMETERS	78
5.1	INTRODUCTION	78
5.2	EXPERIMENTS	78
5.3	RESULTS AND DISCUSSIONS	80
5.3.1	Stacking Sequence Effect	83
5.3.2	Thickness Effect	89
5.3.3	Mass Effect	93
5.4	CONCLUSION	99
6	3-DIMENSIONAL POINT-LOADING IMPACT ANALYSIS AND EXPERIMENTS	100
6.1	INTRODUCTION	100
6.2	STATEMENT OF PROBLEM	100
6.3	ANALYTICAL MODEL	101
6.3.1	Stress Analysis	101
6.3.2	Failure Analysis	105
6.4	EXPERIMENTS	115

6.5 SENSITIVITY STUDY	118
6.6 RESULTS AND DISCUSSIONS	120
6.7 CONCLUSION	134
 7 COMPUTER CODE	 139
 LIST OF PUBLICATIONS RESULTING FROM ARO SUPPORT	 140
 LIST OF ALL PARTICIPATING SCIENTIFIC PERSONNEL	 140
 REFERENCES	 141
 APPENDICES	
 A THE STIFFNESS MATRIX	 150
 B DETERMINATION OF THE DISPLACEMENT OF IMPACTOR	 152
 C DATA OF POINT-LOADING IMPACT EXPERIMENTS	 154
 D USER-FRIENDLY INPUT-OUTPUT OF "3DIMPACT" CODE	 158

LIST OF TABLES

3.1	Ply orientations and geometries of the test specimens	12
4.1	Material properties of T300/976 used in the calculations	57
4.2	Prediction of impact velocity threshold	69
5.1	Ply orientations and geometries of the test specimens	79
6.1	Ply orientations and geometries of the test specimens	116
C.1	Measured delamination sizes of T300/976 $[45_4/ - 45_8/45_4]$	154
C.2	Measured delamination sizes of T300/976 $[0_3/90_3/0_3/90_3/0_3]$	155
C.3	Measured delamination sizes of T300/976 $[0_4/45_2/ - 45_4/45_2/0_4]$. . .	156

LIST OF FIGURES

2.1	Description of the problem	5
3.1	A schematic of the impact test facility	9
3.2	Description of the problems and impactors	10
3.3	Cure cycles used in the test	14
3.4	A schematic of a typical damage pattern of $[0_n/90_m/0_n]$ composites .	15
3.5	Photographs of an undamaged and a damaged $[0_6/90_4/0_6]$ composite	16
3.6	Photographs of an undamaged and a damaged $[0_7/90_2/0_7]$ composite	19
3.7	Photographs of a damaged $[0_3/\pm 45_4/90_3]_s$ composite	21
3.8	Photographs of a damaged $[0_4/\pm 45_4/90_2]_s$ composite	22
3.9	A schematic of a typical damage pattern of $[0_n/90_m/0_n/90_m/0_n]$ composites	23
3.10	Photographs of a damaged $[0_4/90_4/0_4/90_4/0_4]$ composite	24
3.11	Photographs of a damaged $[0_3/90_3/0_3/90_3/0_3/90_3/0_3]$ composite . . .	26
3.12	Photographs of a damaged $[90_3/0_3/90_3]$ composite	27

3.13 Illustration of the relationships between impact damage size and the impact energy	28
3.14 Photographs of an impacted specimen of a $[0_6/\pm 45_4/90_5]_s$ composite	30
4.1 A typical finite element mesh used in the analysis	37
4.2 A schematic of the 8-node serendipity quadrilateral element	38
4.3 The stress components for transverse matrix cracking	49
4.4 Comparison between the calculated and the analytical solutions . . .	53
4.5 Comparison between the calculated and the analytical solutions . . .	54
4.6 Comparison of the calculations between the 2DIMPACT and IMPACT	56
4.7 The calculated maximum strength ratios of e_M for a $[0_6/90_4/0_6]$. . .	58
4.8 The calculated maximum strength ratios of e_M for a $[0_3/\pm 45_4/90_3]_s$	59
4.9 Comparison of the locations of the initial matrix cracks	61
4.10 The instantaneous stress distributions	62
4.11 The calculated interlaminar shear stress distribution	64
4.12 Comparison of the interlaminar shear stress distribution between the static and the transient dynamic calculations	65
4.13 Comparison of the in-plane tensile stress distribution	66
4.14 Comparison of the locations of the initial matrix cracks	67
4.15 Comparison of the instantaneous out-of-plane normal stress distributions	71
4.16 Comparison of the instantaneous interlaminar shear stress distributions	72

4.17	A schematic description of the impact damage mechanism	73
4.18	Comparison of the instantaneous in-plane transverse normal stress distributions	74
4.19	Comparison of the instantaneous out-of-plane, interlaminar shear stress, and in-plane normal stress distributions	76
4.20	A schematic description of two basic impact damage growth mechanisms	77
5.1	Description of the geometry and the boundary conditions of the test specimens	81
5.2	A summary of the test results	82
5.3	The effect of stacking sequence on the impact velocity threshold . . .	84
5.4	A photograph of a life-size $[0_2/90/0_2/90/0/90/0]$, specimen	85
5.5	The effect of stacking sequence on the location of the initial matrix crack	87
5.6	Photographs of three typical life-size tested specimens	88
5.7	The calculated on-set interlaminar shear stress/strength and transverse tensile stress/strength ratios	90
5.8	The effect of laminate thickness on impact velocity threshold	92
5.9	The effect of laminate thickness on the location of the critical matrix crack	94
5.10	Photographs of three typical life-size tested specimens	95
5.11	The calculated on-set interlaminar shear stress/strength and transverse tensile stress/strength ratios	96
5.12	The effect of impactor's mass on the impact velocity threshold	97

5.13	The effect of impactor's mass on the impact velocity threshold	98
6.1	The finite element calculations of the impact force and the central deflection	104
6.2	Basic impact damage mechanism of fiber-reinforced laminated composites subjected to 2-dimensional line loading impact	106
6.3	A typical delamination shape in laminated composites induced by a point nose impact	109
6.4	Measured delamination area within the $[0_6/90_6/0_6]$ laminated composite plates resulting from 2-dimensional line loading impact	110
6.5	Measured delamination area within the $[90_4/0_{10}/90_4]$ laminated composite plates resulting from 2-dimensional line loading impact	110
6.6	A schematic description of the delamination growth mechanism induced by a shear crack	112
6.7	A schematic description of the delamination growth mechanism induced by a bending crack	113
6.8	The sensitivity evaluation of the effect of D_a value on the predicted delamination size	119
6.9	The sensitivity evaluation of the effect of finite element mesh size on the calculated delamination sizes	121
6.10	Three X-Radiographs of $[45_4/-45_4/45_4]$ composites	122
6.11	Comparison of the delamination sizes of T300/976 $[45_4/-45_8/45_4]$ composites	124
6.12	The predicted delamination sizes of $[45_4/-45_8/45_4]$ composites	126

6.13 Three X-Radiographs of $[0_3/90_3/0_3/90_3/0_3]$ composites	127
6.14 Comparison of the delamination sizes of T300/976 $[0_3/90_3/0_3/90_3/0_3]$ composites	128
6.15 The predicted delamination sizes of $[0_3/90_3/0_3/90_3/0_3]$ composites . .	130
6.16 Three X-Radiographs of $[0_4/45_2/-45_4/45_2/0_4]$ composites	132
6.17 Comparison of the delamination sizes of T300/976 $[0_4/45_2/-45_4/45_2/0_4]$ composites	133
6.18 The predicted delamination sizes of $[0_4/45_2/-45_4/45_2/0_4]$ composites	135
6.19 Comparison of delamination sizes and shapes of $[0_4/45_4/-45_4/90_2]_S$ composites	136
6.20 Predicted delamination sizes and shapes of $[0_4/45_4/-45_4/90_2]_S$ com- posites	137

Chapter 1

INTRODUCTION

It is well known that organic matrix fiber-reinforced laminated composites are very susceptible to transverse low-velocity impact, which could cause significant damage embedded within the materials. Such damage involves extensive intraply matrix cracking and interply delaminations. Depending on the extent of the damage, the strength and stiffness of the materials can be significantly reduced [1-12]. Therefore, the knowledge of impact damage in laminated composites is critically important for the application of the materials in structural design.

Hence, this subject has attracted significant attention among researchers recently. Considerable work both experimental and analytical has been performed [13-52], and most of the studies are focused on the damage resulting from a point-nose projectile. With point-nose impact the damage pattern is very complicated and three-dimensional, involving multiple delaminations along interfaces and a considerable number of intraply matrix cracks. Because the damage is mostly embedded inside the materials, it is very difficult to detect. Although several new techniques have been cited in the recent literature [53], C-scan and X-ray machines are still most commonly used for evaluating impact damage in composites. Specimens are also frequently sliced into pieces for visual inspection of internal damage. These procedures are still very time-consuming and tedious.

Some of the prominent work in this area is briefly mentioned in the following:

Sjöblom *et al* [25] used a pendulum type impactor with strain gauges attached to obtain load histories. They found that permanent damage was indicated by jumps in measured energy loss. Clark *et al* [33] proposed a model which explained some characteristics of impact damage, such as the relative sizes of delaminations and occurrence of prominent delamination/cracking features. Gosse *et al* [30] proposed a K-rule which hypothesized that delaminations would occur at the interface bounded by the matrix cracks between two adjacent plies with different orientations. Joshi *et al* [31,46] studied experimentally impact damage in laminated composite plates for damage mechanism and characterization. They showed pictures of a cross ply plate sliced longitudinally and transversely for inspection after impact. Quantitative discussion about failure mechanism was presented. Stori *et al* [40] performed extensive impact tests to evaluate the impact resistance of carbon fiber reinforced composites with various matrix materials.

Although some progress has been made in understanding impact damage, the knowledge of impact damage is still limited by the complexity of the impact damage modes resulting from the previous experiments. Accordingly, information of the impact damage mechanisms and mechanics is still not well developed, and the governing parameters controlling the impact damage in laminated composites are also not fully understood.

In addition to experimental studies, considerable analytical work has also been performed by several investigators. Sun *et al* [20,23] developed an empirical contact law for simulating the contact force distribution of a projectile on impacted composites. A plate finite element method associated with the contact law was used to evaluate transient dynamic behavior of an impacted composite plate. Wu *et al* [13-16] performed an experimental and analytical study on the transverse impact behavior of Graphite/Epoxy laminated composite plate; a non-dimensional empirical expression was developed and used to predict the damage induced by low velocity impact. Gu *et al* [36] developed a model for estimating the impact damage size in SMC composites. However, due to the lack of understanding of the basic mechanisms and mechanics of

impact damage, so far there are no analytical models available for accurately predicting impact damage initiation and the extent of the damage in laminated composites.

Therefore, in this investigation, the major focus of the attention is first concentrated on understanding, through experiments as well as analysis, the basic impact damage mechanisms and mechanics of laminated composites resulting from low-velocity impact. The basic parameters governing the impact damage mechanics and mechanisms are then identified and thoroughly studied. The knowledge gained from the studies is then utilized to develop an analytical model for predicting damage in composites as a result of low-velocity impact.

In Chapter 2, the major approach for achieving the objectives of the investigation is briefly outlined. Chapter 3 describes the development of a new impact facility and a new testing approach for studying impact damage in laminated composites. Simplified impact damage patterns will be presented and the major characteristics of impact damage in laminated composites will be discussed. Chapter 4 presents an analytical model which consists of a stress analysis and a failure analysis for analyzing the experimental results obtained from the tests in the previous chapter. In Chapter 5, effects of impact parameters such as stacking sequence, thickness of the laminate and mass of impactor on the impact damage are studied. Both experimental and analytical results are presented. In Chapter 6, a model will be presented for predicting impact damage initiation and the extent of the damage in laminated composites resulting from a point nose impactor. The comparisons between the numerical simulations and the point nose impact test data obtained from the investigation will also be shown. The information regarding the 3-D impact computer code will be described in Chapter 7.

Chapter 2

METHOD OF APPROACH

2.1 THE OBJECTIVES

This investigation has been performed to study the impact damage in fiber-reinforced polymer matrix laminated composites subjected to low-velocity impact by a foreign point-nose projectile as shown in Figure 2.1.

The major objectives of the investigation are twofold:

1. to study impact damage mechanisms and mechanics of fiber-reinforced laminated composites due to low-velocity impact, and
2. to develop adequate models for predicting the low-velocity impact damage in the materials.

In order to achieve the objectives, this investigation was carried out in three sequential steps as follows:

1. Generation of Simplified 2-Dimensional Impact Test Data.
2. Analysis of Simplified 2-Dimensional Impact Test Data.
3. Development of Point-nose Impact Damage Model.

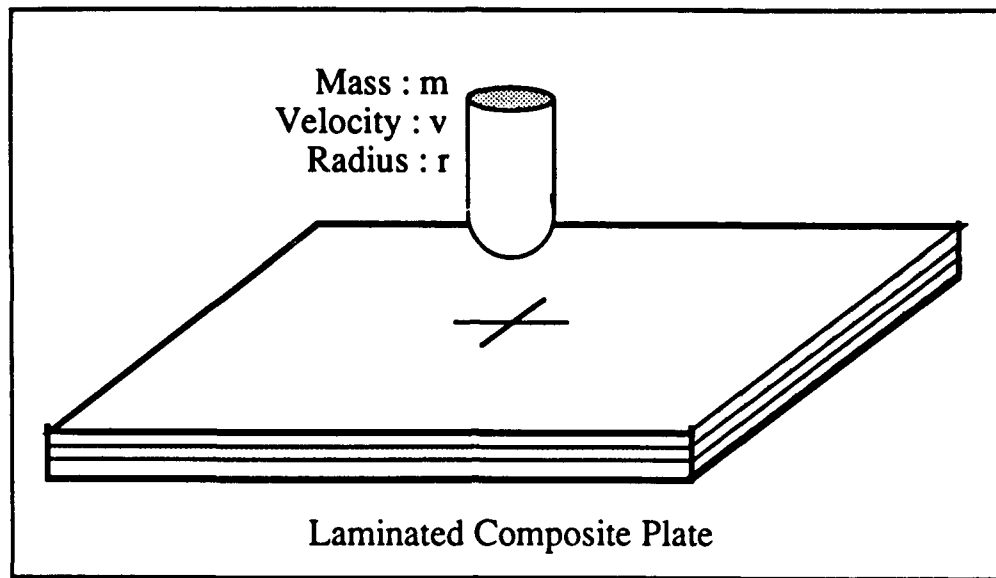


Figure 2.1: Description of the problem. A laminated composite panel subjected to transverse impact by a low-velocity spherical nose projectile.

The major tasks executed in each step are briefly outlined in the next section.

2.2 THE MAJOR TASKS

2.2.1 Generation of Simplified 2-Dimensional Impact Test Data.

A unique impact test facility was designed and built for this study. In this investigation, the line-nose impactors were selected because they could produce uniformly distributed transient dynamic load across the specimen. As a consequence, a uniform and consistent impact damage pattern could be produced in composites, significantly simplifying the impact damage pattern. Accordingly, extensive tests were performed to study the impact damage mechanisms and failure modes of laminated composites subjected to line-loading impact. The initial failure mode and failure mechanisms were thoroughly examined from the test data. The effects of ply orientation, thickness, and mass of the impactor on impact damage were also evaluated.

2.2.2 Analysis of Simplified 2-Dimensional Impact Test Data.

An analytical model was also developed for predicting damage in laminated composites resulting from the line-loading impact. Dynamic stresses and strains in composites were calculated from a transient dynamic finite element code based on a plane strain condition, which was developed during the work. A modified Hashin matrix failure criterion [54] was proposed to predict the initial damage, and a post-failure analysis after the occurrence of the initial damage was also performed to determine the effect of the initial damage on the initiation of delamination and micro-matrix cracks.

2.2.3 Development of Point-nose Impact Damage Model.

In this work, an analytical model was developed based on the previous line-loading impact results, by extending the previous two-dimensional model to predict the impact damage resulting from a point-nose impactor. The model consists of a stress analysis for determining the stress distributions inside the materials during impact, and a failure analysis for predicting the initiation and the extent of the impact damage. The information on the transient dynamic stresses is required for accurately predicting impact damage from the failure analysis. In the failure analysis, a matrix failure criterion and a delamination criterion were proposed for predicting the initial impact damage and the extent of the damage due to impact, respectively. Point-nose impact experiments were also performed during the investigation.

Chapter 3

2-DIMENSIONAL LINE-LOADING IMPACT EXPERIMENT

3.1 INTRODUCTION

The objective of this experiment is to gain a fundamental understanding of damage mechanisms and mechanics of laminated composites due to low-velocity impact and to determine essential parameters governing impact damage. It was observed from the previous experiments that impact damage can be significantly affected by the laminate configuration, including ply orientation and thickness, and the energy of the impactor. Similar phenomena have also been recorded in the literature for impact damage resulting from traditional point-nose impactors [14,30,31,44,46,47]. Apparently, there exist relationships that relate the impact damage to the material properties, geometry, ply orientation, and mass and velocity of the impactor. Because the experimental procedures for inspecting the embedded damage caused by a point-nose impactor are very tedious and time-consuming, it is very difficult to rely simply on the point-nose impact test to establish these relationships and fundamentally understand these phenomena. None of these relationships have been established experimentally or analytically in the literature. However, it is believed that the knowledge of such information is critically important to design engineers in selecting proper materials, layups and geometry for designing composite structures with better impact resistance.

In order to achieve this objective, a new impact tester was designed and built for the investigation. The impactors were designed with a line-edge nose, rather than

a point nose, which considerably reduced the complexity of the impact damage into several basic patterns. The major advantages of using the line-loading impactor are that not only can the damage pattern be simplified, but most importantly, it can be inspected easily from the sides of the specimens, without resorting to sophisticated nondestructive testing machines such as a C-scan or an X-ray.

3.2 A NEW IMPACT TESTER

The major apparatus of the facility consists of a pressure tank, a precision-made barrel, a high precision timer, optical fiber photoelectric sensors, and supporting fixtures, as shown in Figure 3.1. The essential characteristics of the design, which is different from any other available in the literature, are the use of a barrel with a rectangular cross section and the impactors. The barrel is made of four carbon-steel strips, precisely assembled with the maximum tolerance of the dimensions of the inner cross section varied along the axis of the barrel within 0.01 cm. The inner dimensions of the barrel are 7.62 cm in height and 6.35 cm in width, with a wall thickness of 1.27 cm. The length of the barrel is about 137 cm.

Because the barrel is rectangular, the impactors can be designed in two parts, a common rectangular base and a nose which can be made into different shapes, which can be easily mounted and dismounted from the base (see Figure 3.2). Thus, different damage patterns can be produced by selecting the appropriate nose shape for the impactor. For instance, the impact damage caused by a spherical nose is considerably different from that produced by a line-nose impactor.

During the test, the impactor was driven by compressed air from the air tank through the rectangular barrel. The velocity of the impactor was controlled by selecting proper weights for the base and the nose of the impactor, and by adjusting the air pressure from the air tank. The setup of the tester is designed so that once the impactor strikes the target, it immediately rebounds back into the barrel. Therefore, this facility can be used to evaluate the impact damage in composites as a function

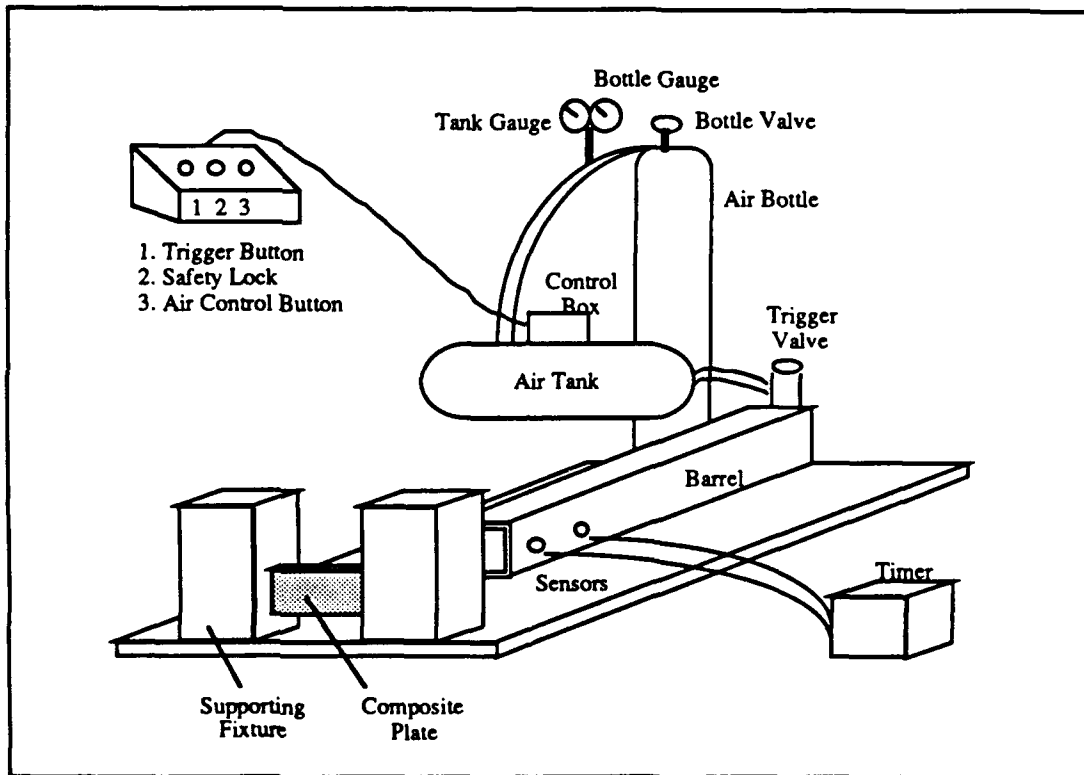


Figure 3.1: A schematic of the impact test facility.

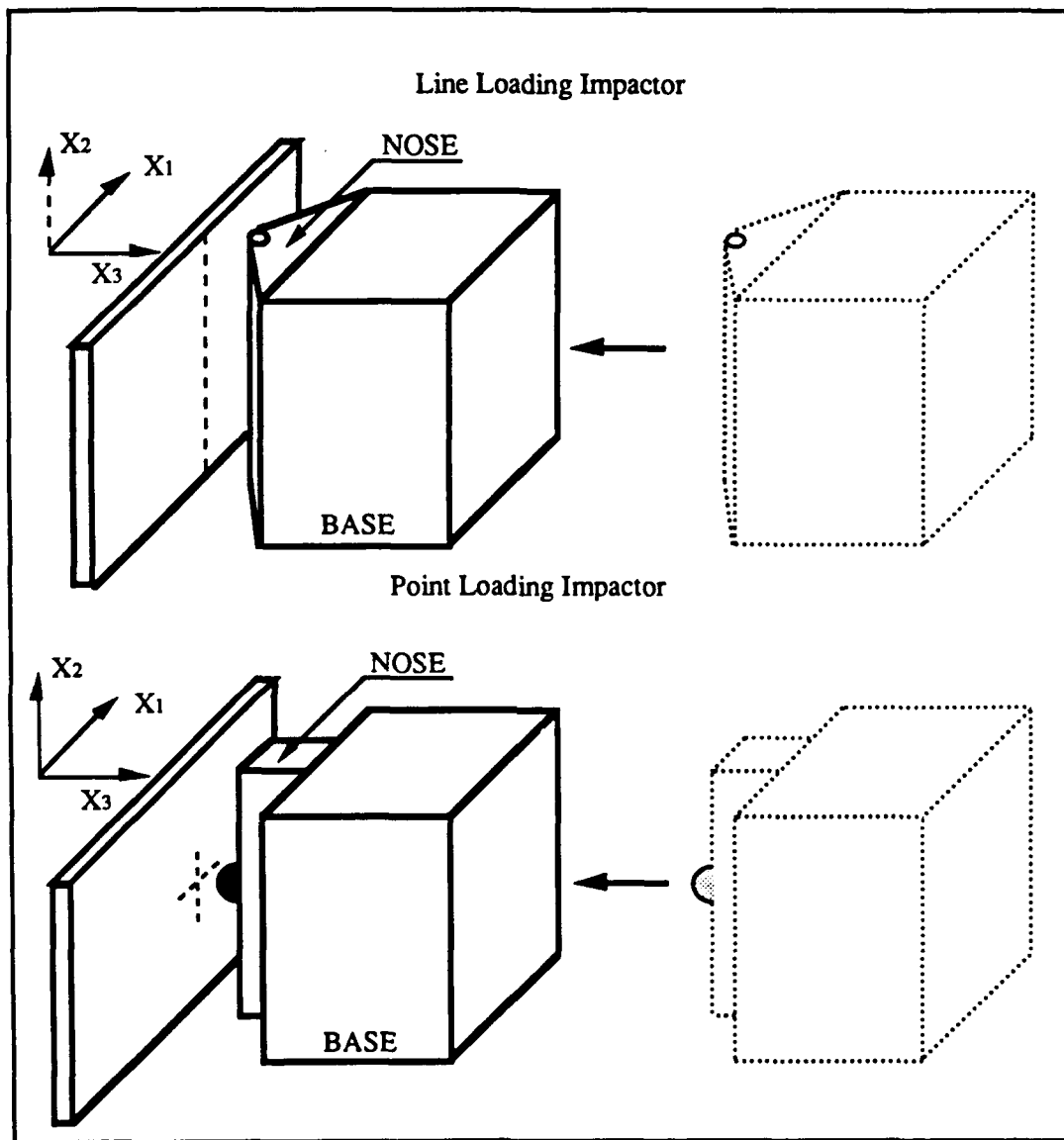


Figure 3.2: Description of the problems and impactors. (A): a line-nose impactor. (B): a point-nose impactor.

of the weight and velocity of the impactor and the nose shape of the impactor. For instance, the velocity of a 60 gram impactor can be achieved as high as 40 m/sec. The heavier the mass of an impactor, the lower the maximum velocity will be.

For this investigation, a line-nose impactor was chosen, as shown in Figure 3.2. The use of the line-nose impactor results in an uniformly distributed transient dynamic load across the specimen which is clamped on two parallel free edges. It was expected that such a uniform loading would produce a consistent and uniform damage pattern throughout the specimen width, hence substantially simplifying the impact damage mechanisms from a three-dimensional to a two-dimensional event.

3.3 EXPERIMENTS

Extensive impact tests were performed to study impact damage in laminated composites subjected to line-nose impact. Different ply orientations and various thicknesses of the specimens were selected for the tests. Table 3.1 lists the ply orientations and the geometries of the specimens. During testing, different weights and velocities of the impactors were used as additional test parameters.

T300/976 Graphite/Epoxy prepregs were selected to fabricate specimen panels. An autoclave was used to cure the panels. The dimensions of the panels were about 25.4 cm wide by 25.4 cm long. After curing, each panel was sliced with a diamond-coated saw into three specimens of 7.62 cm x 15.24 cm. All the specimens were X-rayed before testing to evaluate any internal, pre-existing damage caused by either curing or cutting.

At first, a widely used cure cycle, as shown in Figure 3.3 (A), recommended by the manufacturer was adopted to cure the $[0_6/\pm 45_4/90_5]_s$ and $[0_8/90_6/0_8]$ panels. However, when X-rayed, it was found that the $[0_6/\pm 45_4/90_5]_s$ specimens contained significant amounts of internal matrix cracks in the 0 and 90 degree layers. Furthermore, the $[0_8/90_6/0_8]$ panels were completely debonded along the 0 and 90 interfaces after being cured. Hence, it seemed the cure cycle was the culprit; the heating and

Ply Orientation	Thickness (h) (mm)	Span length (L) (cm)	Width (W) (cm)
[07/90 ₂ /07]	2.30	10.0	7.6
[06/90 ₄ /06]	2.30	10.0	7.6
[0 ₄ /±45 ₄ /90 ₄ /±45 ₄ /0 ₄]	2.88	10.0	7.6
[0 ₃ /±45 ₄ /90 ₆ /±45 ₄ /0 ₃]	2.88	10.0	7.6
[0 ₆ /±45 ₄ /90 ₁₀ /±45 ₄ /0 ₆]	4.31	7.6	7.6
[0 ₄ /90 ₄ /0 ₄ /90 ₄ /0 ₄]	2.88	10.0	7.6
[90 ₃ /0 ₃ /90 ₃]	1.30	10.0	7.6
[0 ₃ /90 ₃ /0 ₃ /90 ₃ /0 ₃ /90 ₃ /0 ₃]	3.02	10.0	7.6

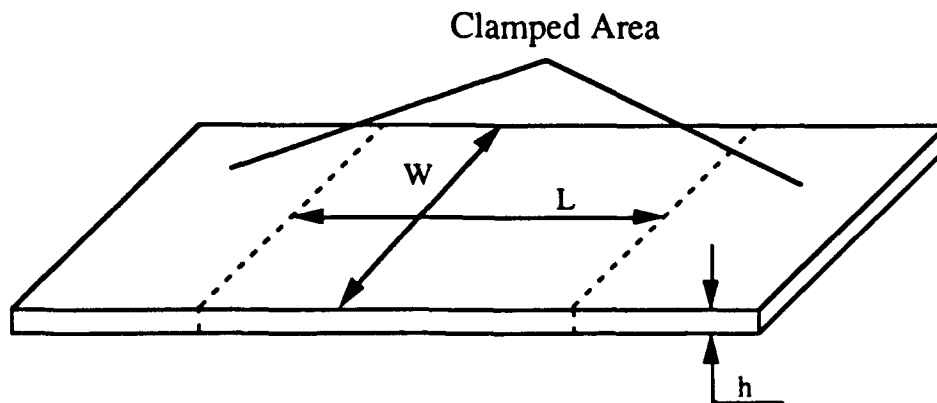


Table 3.1: Ply orientations and geometries of the test specimens.

cooling rates were too high to allow the matrix to relax from a viscous state to a solid state, which caused excessively high residual thermal stresses to build up inside the laminates. Accordingly, a new cure cycle with a slightly lower cure temperature was chosen with slower heating and cooling rates as shown in Figure 3.3 (B). No pre-matrix cracks were found in any of the panels cured under the new cycle. Overall, more than 100 specimens were tested during this investigation. The results from the tests are summarized in the following section.

3.4 EXPERIMENTAL RESULTS

3.4.1 Matrix Cracks and Delaminations

$[0_6/90_4/0_6]$

Figure 3.4 shows a typical schematic of the impact damage pattern in $[0_6/90_4/0_6]$ laminated composites impacted by a line-nose impactor. Basically, damage appeared in the three possible locations, each of which consisted of a matrix crack and a delamination; one near the center region and the other two close to the clamped boundaries. Because of line-loading impact, the resulting impact damage, matrix cracks and delaminations are clearly visible from the sides of each specimen. The damage near the center of the specimens is an instant result from the impact and is the focus of the study.

A side view photograph of the damage near the center region of a lifesize specimen of $[0_6/90_4/0_6]$ after impact is shown in Figure 3.5. Clearly, there is a matrix crack aligned about 45 degrees from the impact direction leading to delaminations along the upper and lower interfaces between the 0 degree and 90 degree plies. This crack was not located directly beneath the impacted area, but at some distance away and it always appeared near the same location in all the tested $[0_6/90_4/0_6]$ specimens.

It was discovered that if these matrix cracks did not appear in the impacted specimens, then there was no delamination. Once damage occurred, delamination

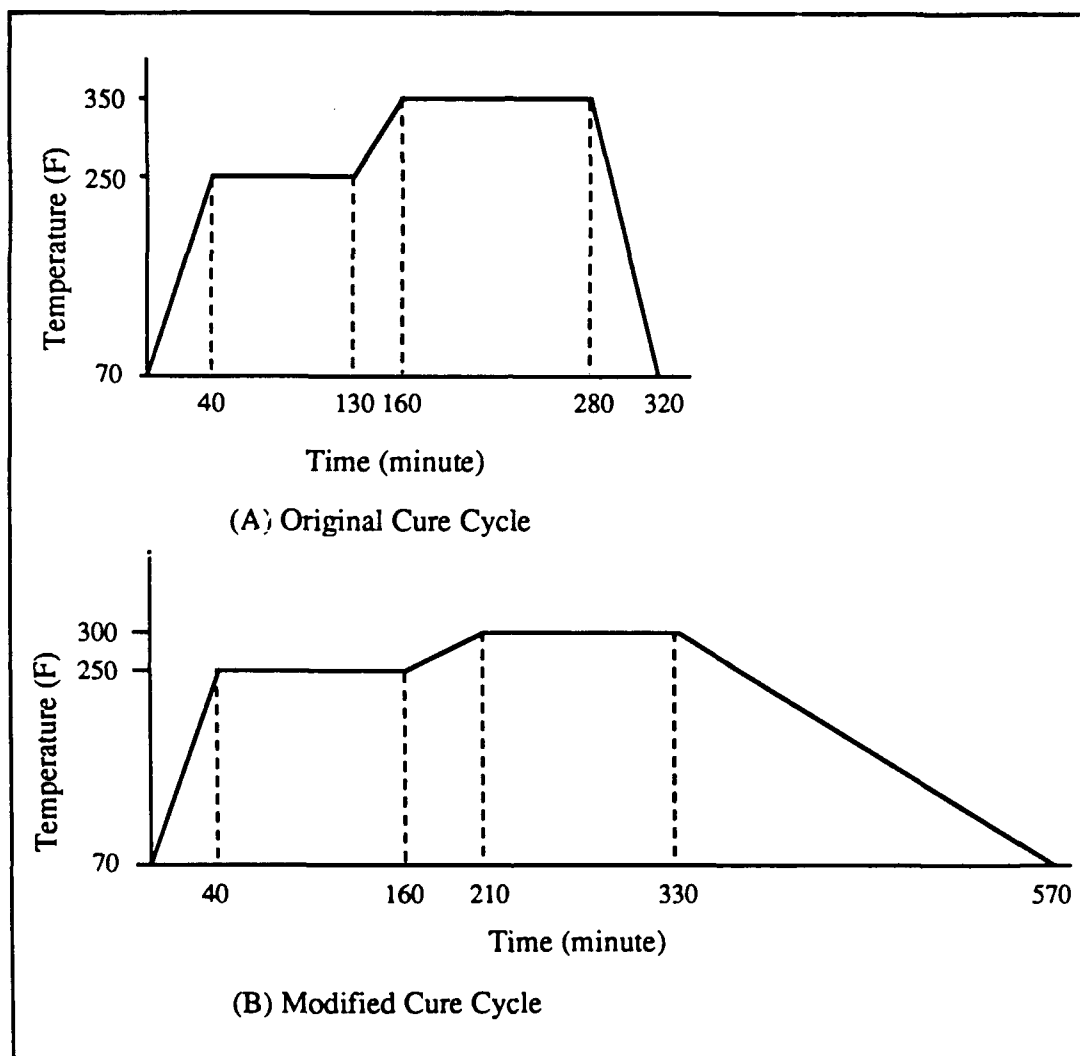


Figure 3.3: Cure cycles used in the test. (A): the original manufactures' recommended cure cycles. (B): the modified cure cycle.

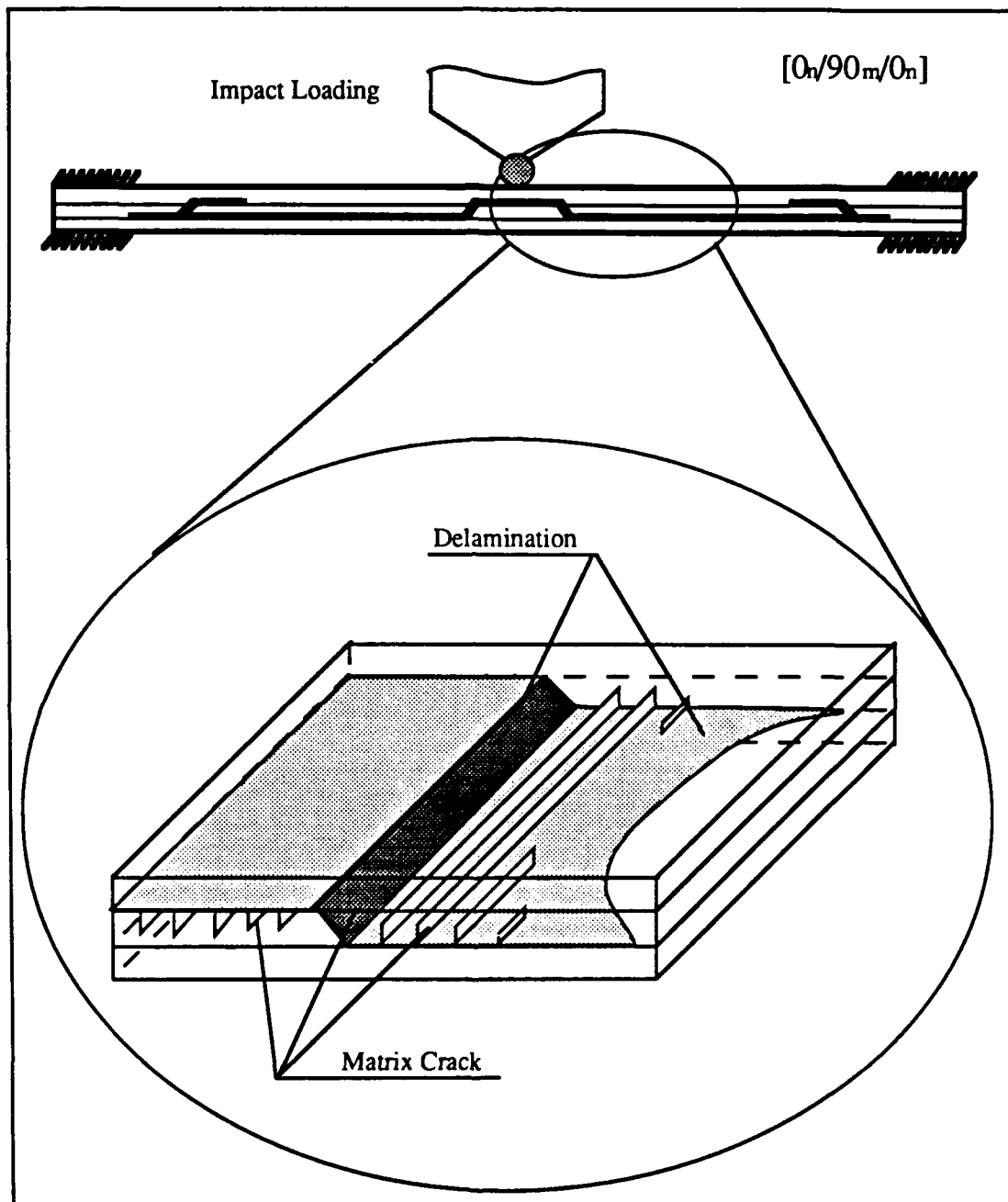


Figure 3.4: A schematic of a typical damage pattern of $[0_n/90_m/0_n]$ composites.

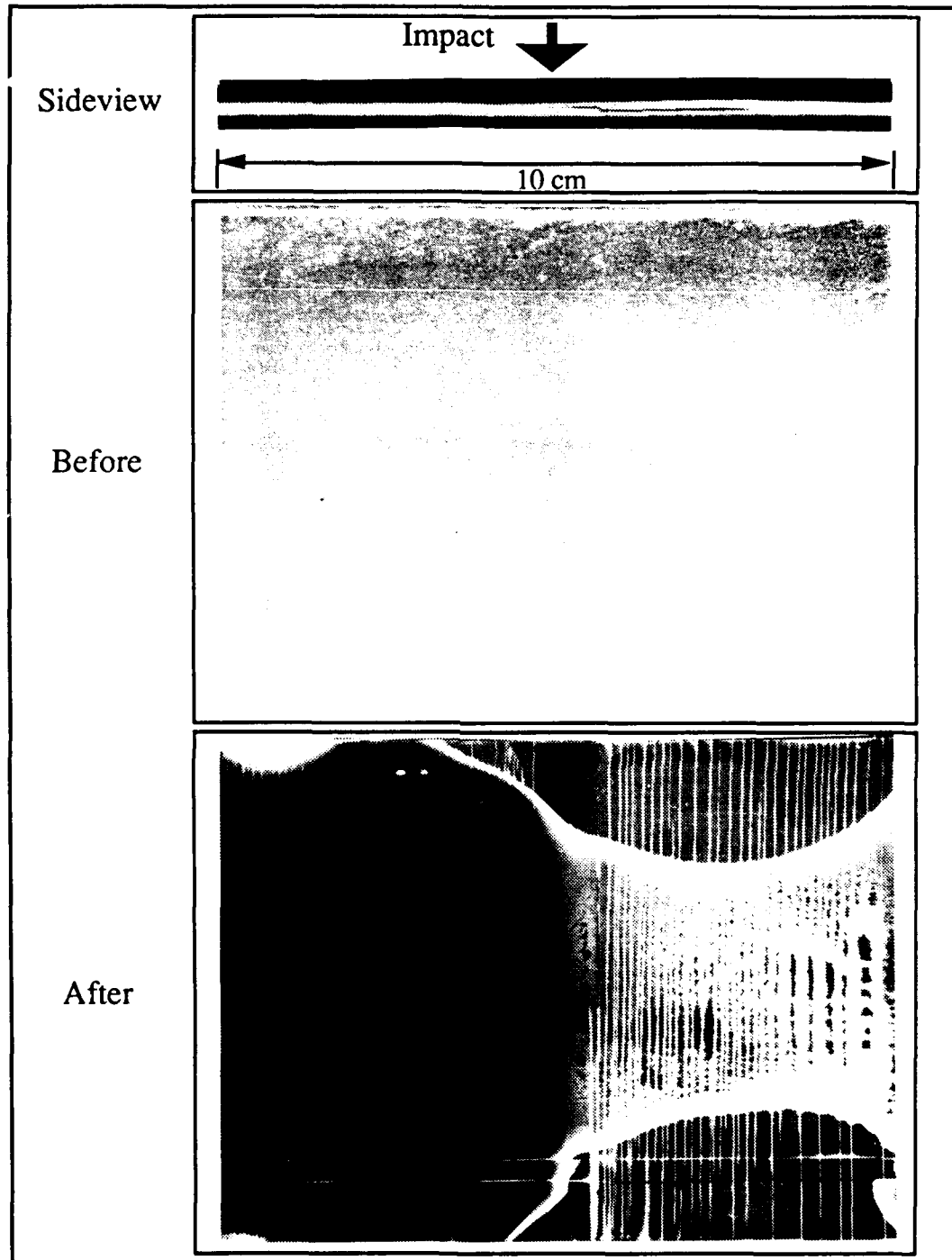


Figure 3.5: Photographs of an undamaged and a damaged $[0_6/90_4/0_6]$ composite. Top: a side-view photograph of a life-size damaged specimen. Center: X-radiograph of the specimen before impact. Bottom: X-radiographs of the specimen after impact.

was always very extensive and expanded across the width of the specimen. The delamination along the upper interface of the 90 degree layers propagated toward the center of the impacted area, while the one located at the bottom interface grew significantly away from the location of the critical crack and toward the boundary. The delaminations seemed to initiate from the matrix crack. The results strongly suggested that these matrix cracks were the initial failure mode of impact damage in laminated composites. Delaminations were initiated once the cracks had propagated to the interfaces between the plies containing different ply orientations. These types of matrix cracks are referred to as the "critical matrix cracks" hereafter in this paper.

Figure 3.5 also shows the X-radiographs of a $[0_6/90_4/0_6]$ specimen before and after impact. Clearly, before impact there was no damage in the specimen. However, after impact the X-radiograph shows significant amounts of internal damage in the specimen. Not only was the delamination the apparent failure mode, but extensive micro-cracks were also found. To clarify, an enlarged view of a similar damage pattern near the center region is presented schematically in Figure 3.4. Clearly, these micro-cracks were not seen by the naked eye, even with the aid of a binocular microscope with 20 times of magnification, nor were they revealed with a C-scan machine. They were, however, detectable from a X-radiograph, indicated by straight, parallel white lines. Apparently, these micro-cracks were generated along with delamination growth.

Theoretically, a pair of critical matrix cracks should exist near the impacted area if the specimen was symmetric with respect to the loading and if the internal flaws in the laminate were uniformly distributed. However, in reality, only a few tests were found to produce double critical cracks near the center region. The white double curve edges shown in the X-radiograph of the damaged specimen are the boundaries of the contact area between the upper and lower interfaces of the delamination in the laminate. Delaminations shown in the side-view photograph of the figure actually were equal when the specimen was viewed on either side. In most of the case studies, delaminations propagated throughout the width of the specimens quite uniformly. The delamination fronts near the free edges were found to have propagated slightly further than those in the inner areas. However, it was found that the energy of the

impactor required to produce the initial impact damage was nearly linearly proportional to the specimen width, indicating that the effect of the free edge was minimal for this study, since the actual delamination size was not the major concern of the study.

$[0_7/90_2/0_7]$

The damage pattern that appeared in $[0_6/90_4/0_6]$ specimens was seemingly reproduced in the $[0_7/90_2/0_7]$ specimens. However, for a given mass of the impactor, a higher velocity was required to cause damage in the $[0_7/90_2/0_7]$ specimens than for the $[0_6/90_4/0_6]$ laminates. As a result, once damage occurred it was more violent in the $[0_7/90_2/0_7]$ composites than in the $[0_6/90_4/0_6]$ specimens.

Figure 3.6 shows three photographs of a tested specimen. The top figure shows a side-view of a specimen after impact. Again, there existed a critical matrix crack in the 90 degree layer near the impacted area. An extensive delamination was found between the 0 and 90 degree layer interfaces initiating from the critical crack. The delamination propagated along the lower and upper interfaces from the tips of the critical matrix crack.

The results of the X-radiographs of the specimen before and after impact are also presented in Figure 3.6. Clearly, no damage was found before testing, but significant damage, including micro-cracks and delaminations, appeared in the specimen after impact. In addition to the micro-cracks in the 90 degree layers, the 0 degree layers also contained a few matrix cracks which apparently enhanced the extent of the delaminations. Accordingly, the size of the delaminations was much more non-uniform in shape than in the $[0_6/90_4/0_6]$ composites.

$[0_4/\pm 45_4/90_2]_s$ and $[0_3/\pm 45_4/90_3]_s$

Laminates containing ± 45 degree angle plies were also evaluated in the study. Again, all the damaged specimens contained critical matrix cracks. Figures 3.7 and 3.8 show photographs of typical $[0_3/\pm 45_4/90_3]_s$ and $[0_4/\pm 45_4/90_2]_s$ specimens after impact, respectively. Surprisingly, in addition to the critical cracks located near the

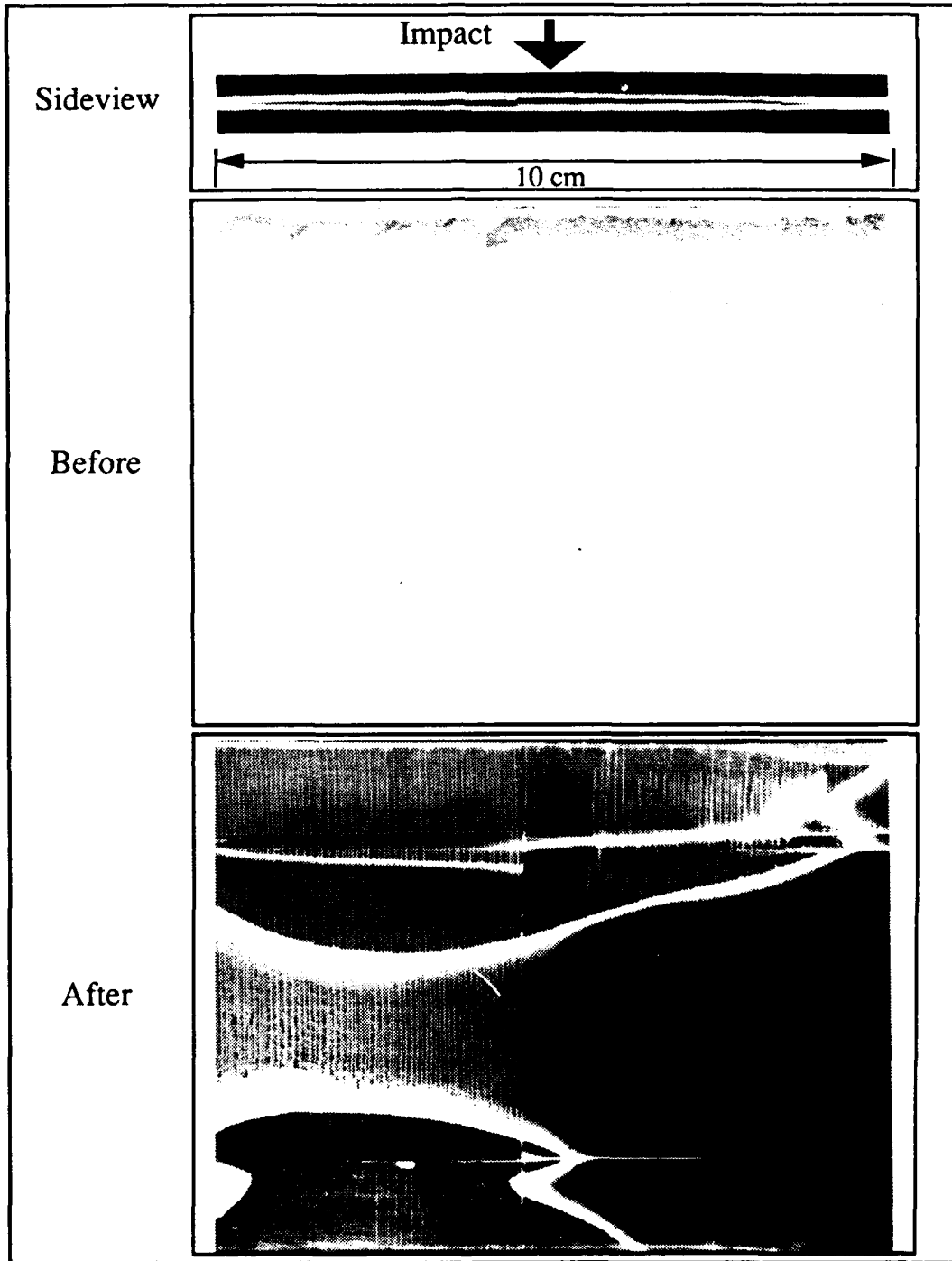


Figure 3.6: Photographs of an undamaged and a damaged $[0_7/90_2/0_7]$ composite. Top: a side-view photograph of a life-size damaged specimen. Center: an X-radiograph of the specimen before impact. Bottom: an X-radiograph of the specimen after impact.

center and the boundaries of the specimens, cracks were also found between the central impacted region and the boundaries, as shown in Figures 3.7 and 3.8. All the critical matrix cracks appeared in the 90 degree layer and led to extensive delaminations. Delamination occurred along the interface between the ± 45 degree and 90 degree layers. By examining the X-radiographs in Figures 3.7 and 3.8, it appears that besides the micro-cracks in the 90 degree layers, there are also micro-cracks found in the ± 45 degree layers within the delamination region. Apparently, these micro-cracks in the ± 45 degree layers were generated along with the delamination propagation as were those in 90 degree layers.

$[0_4/90_4/0_4/90_4/0_4]$

All the specimens considered above contained only one group of 90 degree plies located in middle plane of the specimens. Tests were also performed on $[0_4/90_4/0_4/90_4/0_4]$ specimens which contained two 90 degree ply groups located off the middle plane. It was intended to evaluate the effect of the location and number of 90 degree ply groups on impact damage. Typical results generated from the tests are shown in Figure 3.9.

Near the centrally impacted region, a critical matrix was found in each 90 degree ply group, leading to delamination along each interface between the 0 degree and 90 degree ply groups. Sometimes a double critical matrix crack symmetrically appearing from the impacted area was produced, as shown in Figure 3.10. The delamination on the lower interface propagated much more extensively than the one on the upper interface. These two delaminations were separated by the 0 degree layer group located in the middle plane.

$[0_3/90_3/0_3/90_3/0_3/90_3/0_3]$

Like the above tested specimens, the results from the $[0_3/90_3/0_3/90_3/0_3/90_3/0_3]$ specimens, which contained three 90 degree ply groups, showed multiple critical matrix cracks in the 90 degree layer groups. A photograph of a typical test result is shown in Figure 3.11. Once again, these critical cracks led to multiple delaminations which were individually constrained by the 0 degree ply groups. One interesting

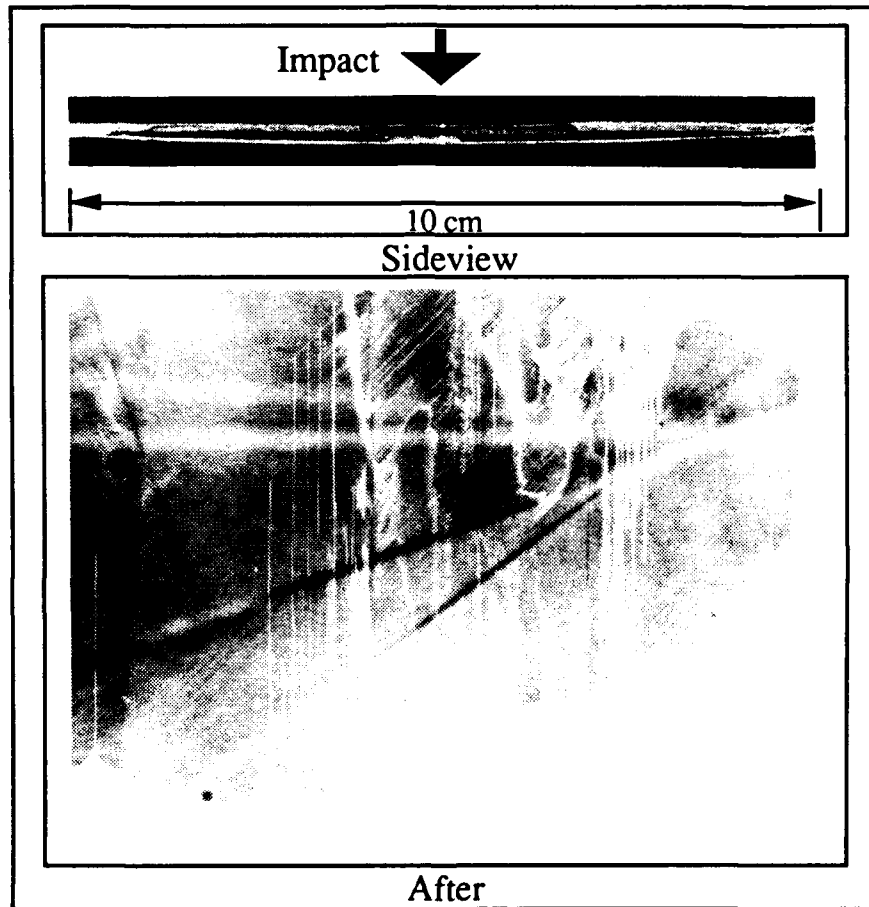


Figure 3.7: Photographs of a damaged $[0_3/\pm 45_4/90_3]_s$ composite. Top: a side-view photograph of a life-size damaged specimen. Bottom: an X-radiograph of the specimen after impact.

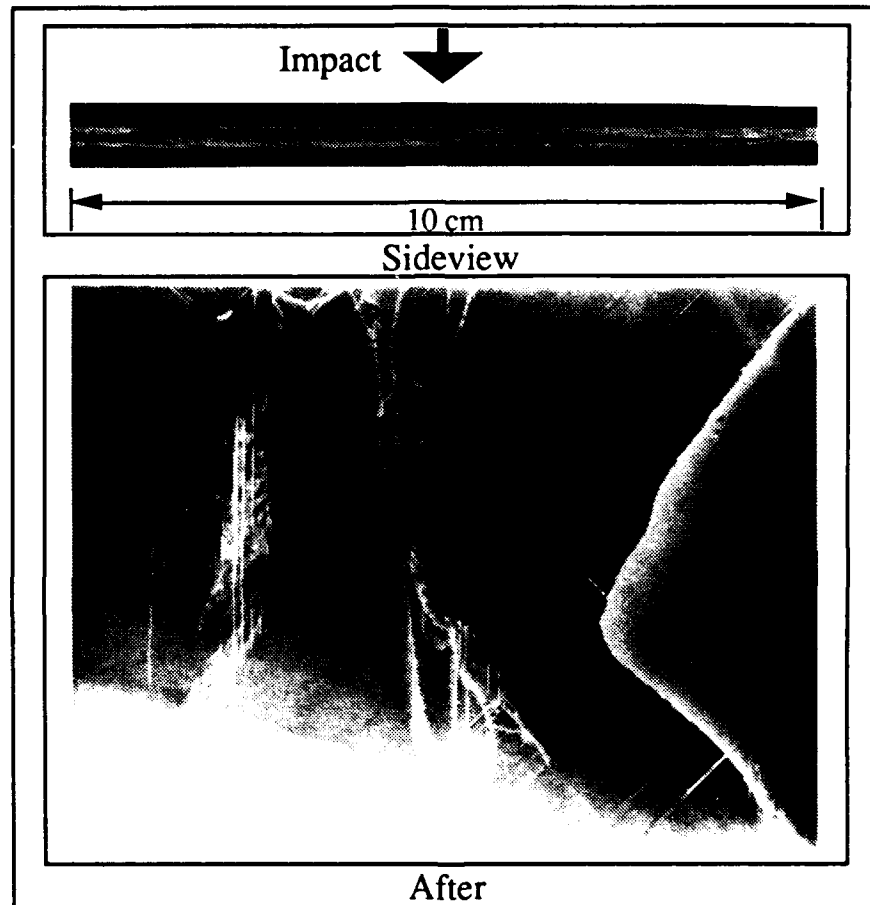


Figure 3.8: Photographs of a damaged $[0_4/\pm 45_4/90_2]$, composite. Top: a side-view photograph of a life-size damaged specimen. Bottom: an X-radiograph of the specimen after impact.

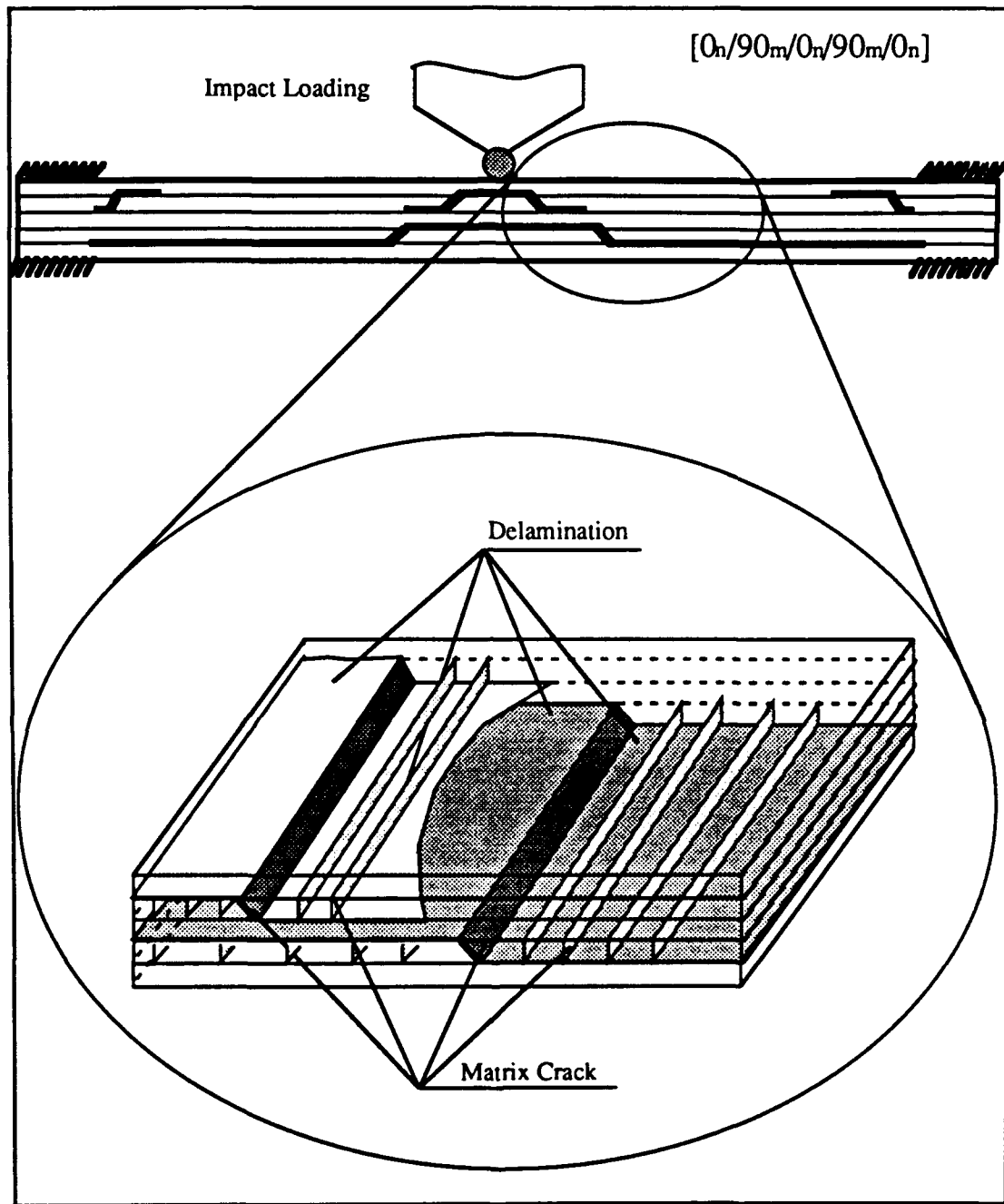


Figure 3.9: A schematic of a typical damage pattern of $[0_n/90_m/0_n/90_m/0_n]$ composites.

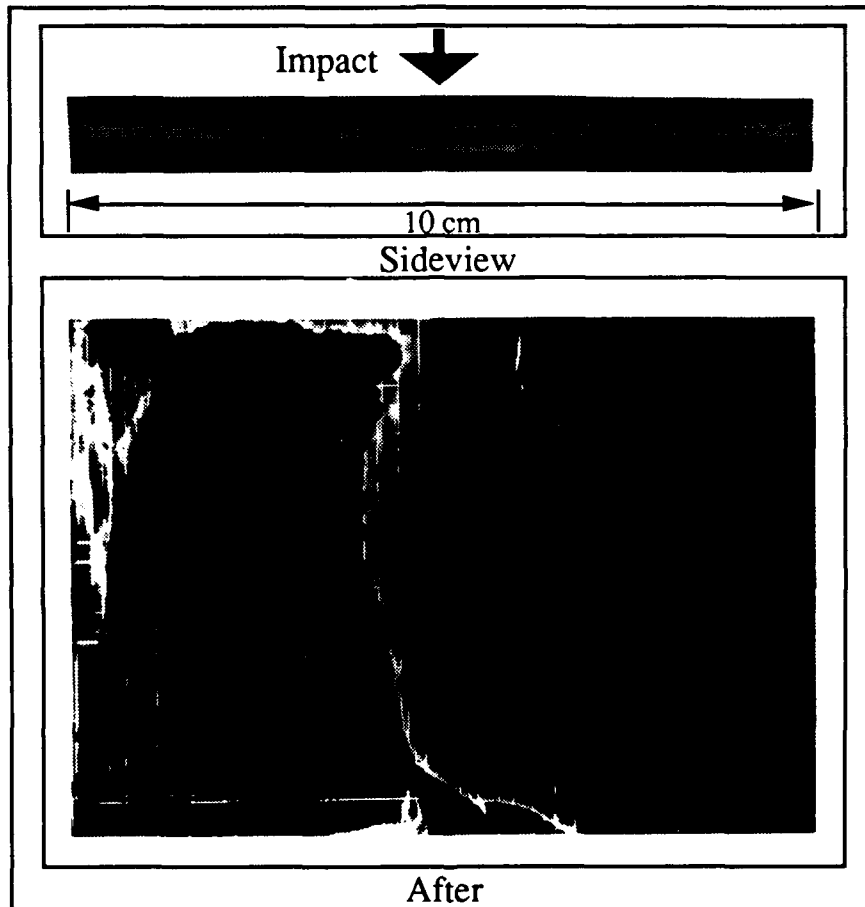


Figure 3.10: Photographs of a damaged $[0_4/90_4/0_4/90_4/0_4]$ composite. Top: a side-view photograph of a life-size damaged specimen. Bottom: an X-radiograph of the specimen after impact.

note worth mentioning is that the critical matrix cracks occurring near the central impacted region were much closer to the center line than those of the other tested specimens with different ply orientations.

$[90_3/0_3/90_3]$

Tests were also performed on $[90_3/0_3/90_3]$ laminates containing 90 degree ply groups on the outer layers. Intuitively, it was expected that the 90 degree ply groups are prone to produce intraply matrix cracking, because of excessive out-of-plane bending stress due to impact. The intuition was confirmed by the experiments. A photograph of a lifesize tested specimen of $[90_3/0_3/90_3]$ is shown in Figure 3.12. Clearly, a matrix crack initiated directly beneath the impacted area on the bottom 90 degree ply group and produced a delamination along the interface between the 90 and 0 degree ply groups. It is noted that the matrix crack is aligned vertically (parallel to the loading direction) and different from the other embedded matrix cracks, which were all inclined by an angle with respect to the loading direction, found in previously tested specimens with the 0 degree ply groups on the outer surfaces.

3.4.2 Impact Energy Threshold

One unique feature of the 2-dimensional impact results is that once damage occurs, delamination is always very extensive. Figure 3.13 presents the estimated delamination size in specimens of various ply orientations as a function of impact energy. There apparently exists an impact energy threshold beyond which damage occurs. For instance, the energy threshold of $[0_6/90_2]$ composites is about 100 J/m for a given impactor of 1.142 kg/m, beyond which significant delaminations are produced. No damage, including matrix cracks and delaminations, was found in any of the specimens tested below that energy level. Similar results are also shown in Figures 3.13 for other ply orientations. It is noted that all the dimensions above are normalized by width, based on the two-dimensional approach.

It was strongly implicated that the impact energy threshold was associated with

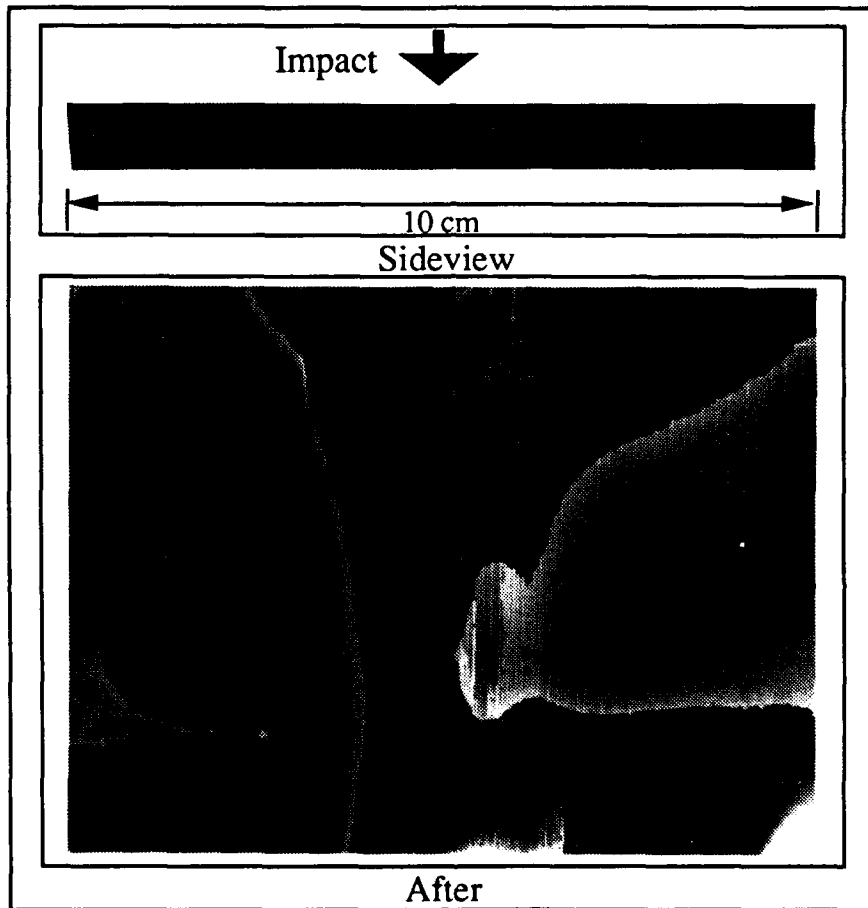


Figure 3.11: Photographs of a damaged $[0_3/90_3/0_3/90_3/0_3/90_3/0_3]$ composite. Top: a side-view photograph of a life-size damaged specimen. Bottom: an X-radiograph of the specimen after impact.

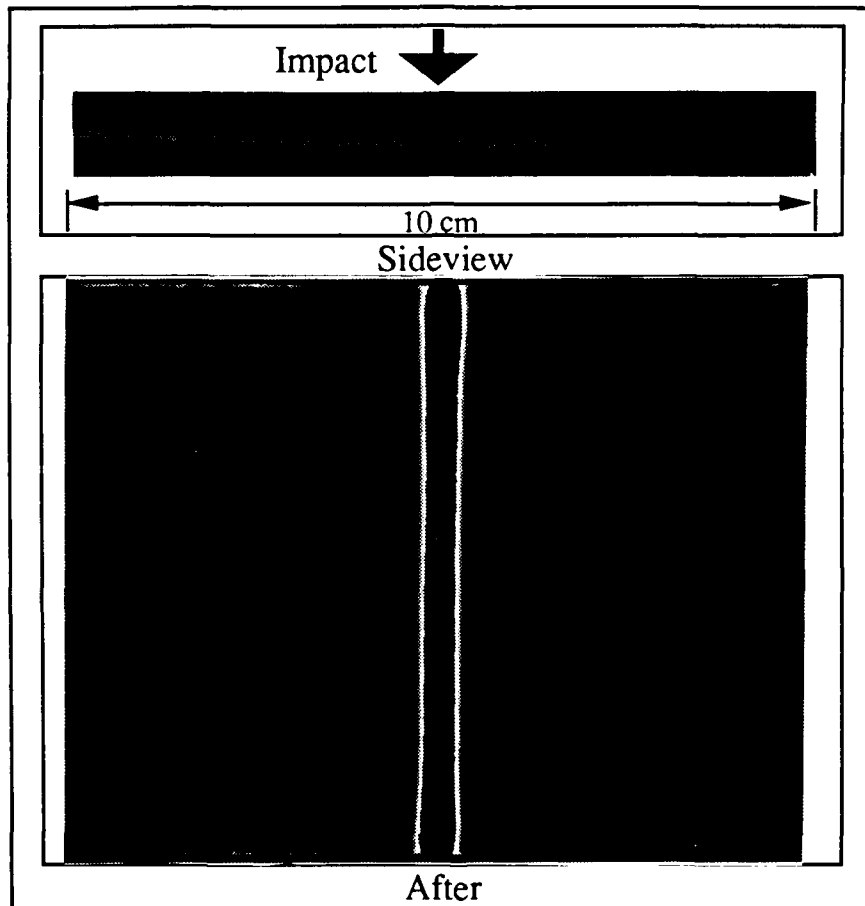


Figure 3.12: Photographs of a damaged $[90_3/0_3/90_3]$ composite. Top: a side-view photograph of a life-size damaged specimen. Bottom: an X-radiograph of the damaged specimen.

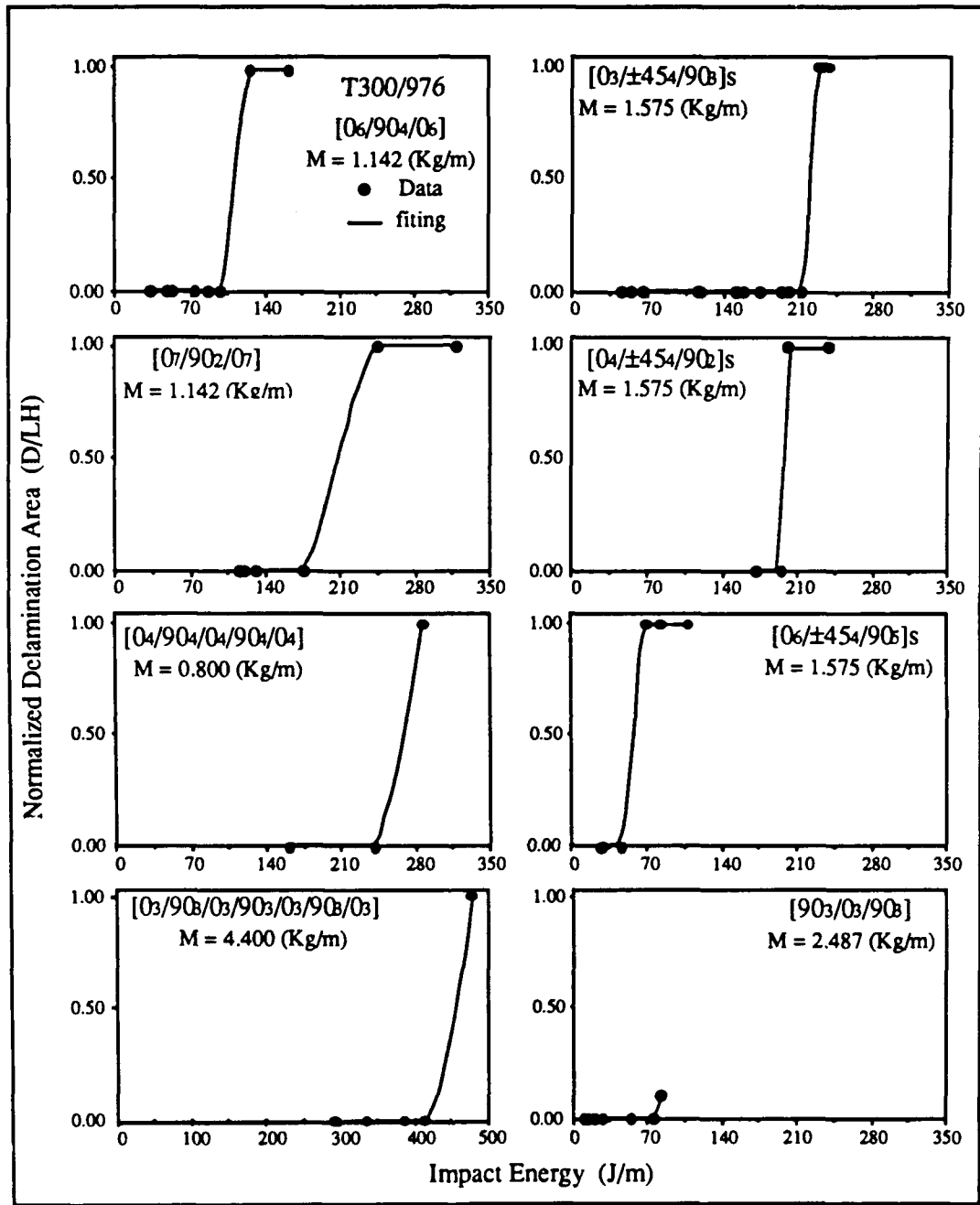


Figure 3.13: Illustration of the relationships between impact damage size and the impact energy for different ply orientations.

the energy required to initiate the impact damage. The existence of an impact energy threshold for point-loading cases also has been reported by other investigators [25,34,47]. Additionally, it appears that the impact energy threshold also strongly depends on the ply orientation, seen in Figure 3.13. The energy threshold may vary for different ply orientations. This information on the impact energy threshold could be useful in design as a guideline for selecting appropriate composites and for determining the configuration and layups of composite structures in order to sustain impact.

3.4.3 Pre-existing Micro-cracks Due to Thermal Residual Stresses

Due to the thermal expansion coefficient mismatch, manufacturing produces significant thermal residual stresses in laminated composites [55-58]. The amount of residual stress depends strongly on the degree of the thermal coefficient mismatch, the ply orientation, and the cure cycle. For $[0_6/\pm 45_4/90_5]$, layups cured under the standard cure cycle given in Figure 3.2, residual stresses exceeded the in situ transverse strength of the 90 degree plies in the laminate and caused micro-matrix cracks, as shown in Figure 3.14. However, for $[0_4/\pm 45_4/90_2]$, and $[0_3/\pm 45_4/90_3]$, laminates cured under the new cycle, no damage was found after curing.

For the specimens with pre-matrix cracks, the impact energy required to initiate damage was found to be substantially lower than for those laminates with similar layups but without pre-matrix cracks. Figure 3.13 shows the reduction of the impact energy threshold in $[0_6/\pm 45_4/90_5]$, laminates compared to those of the $[0_3/\pm 45_4/90_3]$, and $[0_4/\pm 45_4/90_2]$, laminates without pre-matrix cracks. Although the actual ply stacking sequences are slightly different among those compared, the reduction of the energy threshold of $[0_6/\pm 45_4/90_5]$, composites is very substantial and can be primarily attributed to the existence of the pre-matrix cracks. Figure 3.14 also shows an X-radiograph of a $[0_6/\pm 45_4/90_5]$, specimen with pre-matrix cracks after impact. Surprisingly, no additional pre-matrix cracks were found after impact, and the delaminations were initiated from one of the existing pre-matrix cracks and propagated

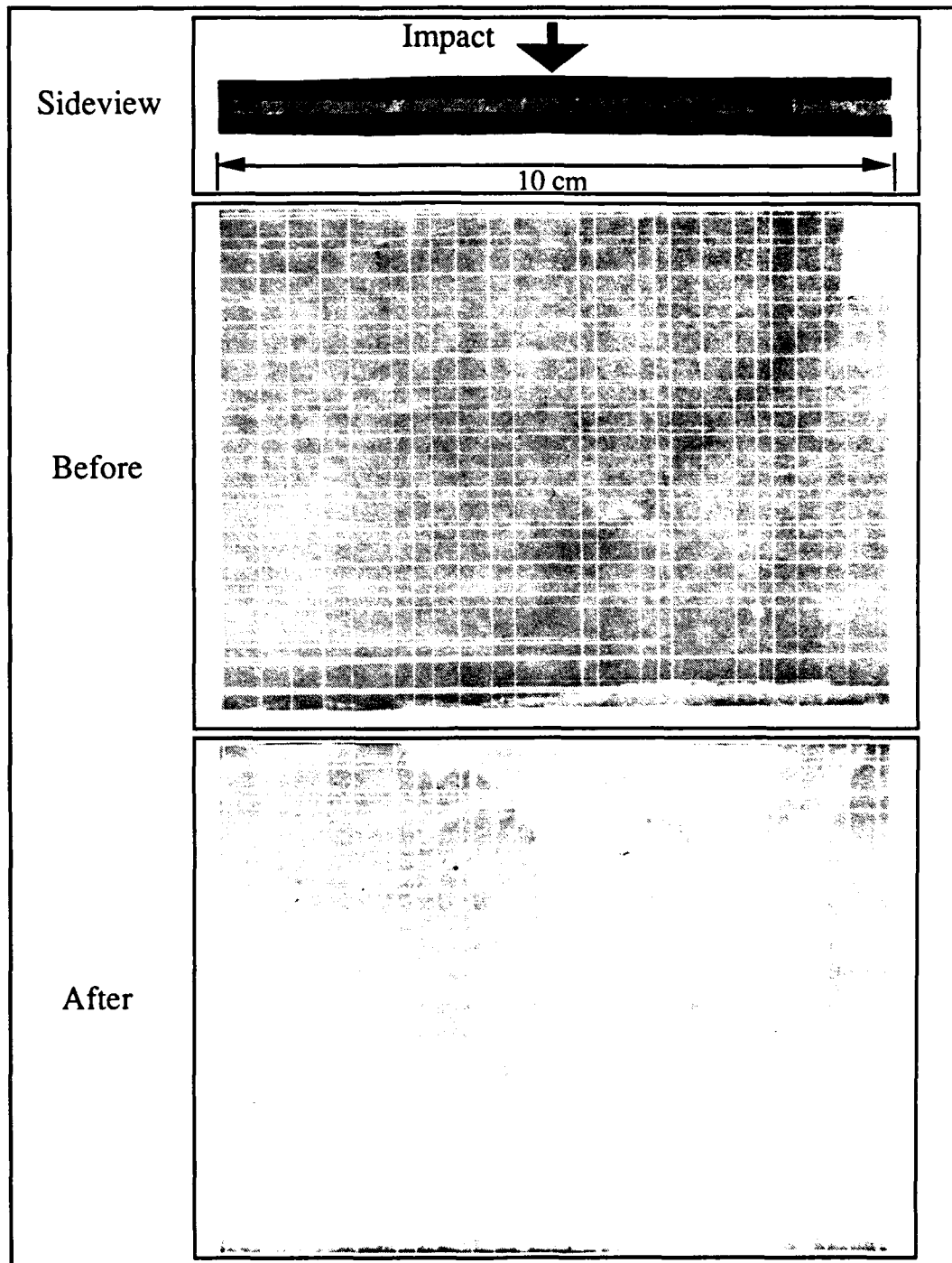


Figure 3.14: Photographs of an impacted specimen of a $[0_6/\pm 45_4/90_5]_s$ composite. Top: a side-view photograph of a life-size damaged specimen. Bottom: an X-radiograph of the specimen before and after impact. A considerable number of internal preexisting cracks were found before impact.

into interfaces in a similar pattern.

Apparently, the critical matrix cracks in $[0_6/\pm 45_4/90_5]$ composites were created from existing pre-matrix cracks and hence required much less energy than normally required to produce the critical crack. Accordingly, the impact energy threshold of the pre-cracked composites is considerably lower than for composites without flaws. Hence, these results strongly indicate that the impact energy threshold is related to the energy needed to initiate the critical matrix cracks.

It is worth noting that even if laminates contain no pre-matrix cracks, there always exists a considerable amount of residual stresses in the materials which could have a significant effect on impact damage. For the materials containing higher residual stresses, it is expected that the materials would have a much lower damage resistance to impact than those containing lower residual stresses. Hence, the energy threshold of a composite also depends strongly upon the amount of residual stresses left in the material due to manufacturing.

3.5 CONCLUSION

An experimental investigation was performed to study impact damage in T300/976 Graphite/epoxy laminated composites. Based on the test results, the following remarks can be made:

1. Matrix cracking initiates impact damage.
2. Delamination is always accompanied by a "critical" matrix crack.
3. Considerable micro-cracks can be generated along with delamination growth during impact.
4. There exists an impact energy threshold above which impact damage occurs.
5. Pre-existing micro-cracks induced by thermal stresses can substantially reduce impact resistance of composites.

6. Stacking sequence significantly affects impact resistance of composites.

Chapter 4

2-DIMENSIONAL LINE-LOADING IMPACT ANALYSIS

4.1 INTRODUCTION

In order to further substantiate the experimental findings and to understand the basic mechanics causing low-velocity impact damage, an analytical investigation was subsequently performed. An analytical model was developed for predicting the impact damage resulting from the tests. The numerical simulations based on the model were also carried out to understand the physics of the impact damage mechanics.

The analytical model described consists of a stress analysis for calculating transient dynamic stresses, strains and deformations during impact, and a failure analysis for predicting impact damage. Numerical simulations of the test conditions based on the analysis are also presented. The effects of geometry and ply orientation of the composites, and the velocity and mass of the impactor on impact damage are evaluated as well. Based on the study, the model combined with the test results provide essential information on the mechanisms and mechanics of impact damage in laminated composites due to low-velocity impact.

4.2 STATEMENT OF PROBLEM

The problem is described as follows: consider a symmetric laminated composite plate clamped along two parallel edges and free on the other two edges. A line-nose impactor strikes uniformly across the width on the center line of the specimen (see Figure 3.2). For a given mass of the impactor, it is desired to determine:

1. The initial failure mode.
2. The location of the initial damage.
3. The velocity required to cause the initial impact damage.
4. The initiation of delamination and micro-cracks.
5. The direction of delamination growth.
6. The essential parameters governing the impact damage.

4.3 ANALYSIS

During the investigation, an analytical model was developed for predicting the impact damage in laminated composites due to line-loading impact. Since the load distribution across the width is assumed to be uniform at any instant time and the boundary conditions are symmetric with respect to the loading condition, the impact response of the plate is assumed to be two-dimensional and independent of the x_2 axis, the direction along the width (see Figure 3.2). Ignoring the effect of free edges, the plane strain condition is adopted for the development of a two-dimensional transient dynamic finite element analysis for the investigation. The finite element analysis is used to calculate transient dynamic stresses, strains, and deformations inside the laminate during impact.

The experiments presented in the previous Chapter strongly indicate that impact damage is initiated by matrix cracking and that there exist critical matrix cracks from which delaminations and micro-cracks initiate. In order to substantiate the findings, the proposed model focuses on predicting the initial failure mode and the critical matrix cracks, and determining the mechanics governing the initiation of delaminations and micro-cracks. Thus, in the model, a matrix failure criterion is adopted and modified for predicting the initial failure mode. A post-failure analysis after the occurrence of the initial damage is also performed to determine the effect of the initial damage on the initiation of delamination and micro-cracks.

4.3.1 Stress Analysis

Based on plane strain condition, the equilibrium equation at an instant time in a variational form can be expressed as [59,60]

$$\int_v \rho u_{i,tt} \delta u_i \delta v + \int_v \sigma_j \delta \epsilon_j \delta v - \int_{s_\sigma} T_i \delta u_i \delta a = 0 \quad \begin{cases} i = 1, 3 \\ j = 1, 3, 5 \end{cases} \quad (4.1)$$

where u_i and $u_{i,tt}$ are the displacements and the accelerations ($u_{i,tt} = \partial^2 u_i / \partial t^2$), respectively. T_i is the contact force distribution during impact. σ_j and ϵ_j are the stresses and strains due to the mechanical loading in contracted notations, i.e.,

$$\{\sigma_1, \sigma_3, \sigma_5\} = \{\sigma_{11}, \sigma_{33}, \sigma_{13}\} \quad (4.2)$$

$$\{\epsilon_1, \epsilon_2, \epsilon_5\} = \{\epsilon_{11}, \epsilon_{33}, \epsilon_{13}\} \quad (4.3)$$

For laminated composites, the material properties may vary from layer to layer throughout the thickness, depending upon the laminate stacking sequence. Hence, Eq. (4.1) can be rewritten on a layer-by-layer basis as follows:

$$\sum_{n=1}^N \int_{n_h} \left[\int_v {}^n \rho {}^n u_{i,tt} \delta {}^n u_i dv + \int_v {}^n \sigma_j \delta {}^n \epsilon_j dv \right] dh = \int_{s_o} T_i \delta u_i da \quad (4.4)$$

where N is the total number of the layers of the laminate considered. The forward superscript n for all the variables indicates the corresponding layer within the laminate.

Thus, the mechanical stresses in the n -th layer are related to the mechanical strains of the corresponding layer through the following equation

$${}^n \sigma_j = {}^n [D_{jk}] {}^n \epsilon_k \quad (4.5)$$

where ${}^n [D_{jk}]$ is the stiffness matrix of the n -th ply of the composites based on the plane strain assumption. A complete expression of the stiffness matrix ${}^n [D_{jk}]$ for a single layer based on the plane strain assumption is given in the Appendix A.

In order to solve Eq. (4.1), the contact load distribution T_i , between the impactor and the composite, must first be known. In this investigation, the Hertzian contact law was adopted to simulate the contact load distribution. Because of the use of a cylindrical line-nose impactor, the Hertzian contact law has a considerably different expression from the one that is most commonly used for a spherical point-nose impactor [61]. Accordingly, the contact load distribution T_i ($= f$) for a line-loading impact is related to the indentation depth α ($= \delta_S - \delta_C$ = the change in the distance between the center of the impactor nose and the mid-plane of the plate) by the following expression [4]

$$\begin{aligned} \alpha &= f(\chi_s + \chi_p) \left\{ 1 - \ln [f r(\chi_s + \chi_p)] \right\} & \text{when } \delta_S \geq \delta_C \\ 0 &= f & \text{when } \delta_S < \delta_C \end{aligned} \quad (4.6)$$

where δ_S is the impactor displacement, δ_C is the plate displacement measured at the center of the mid-plate of the laminate, which is opposite to the impactor's surface,

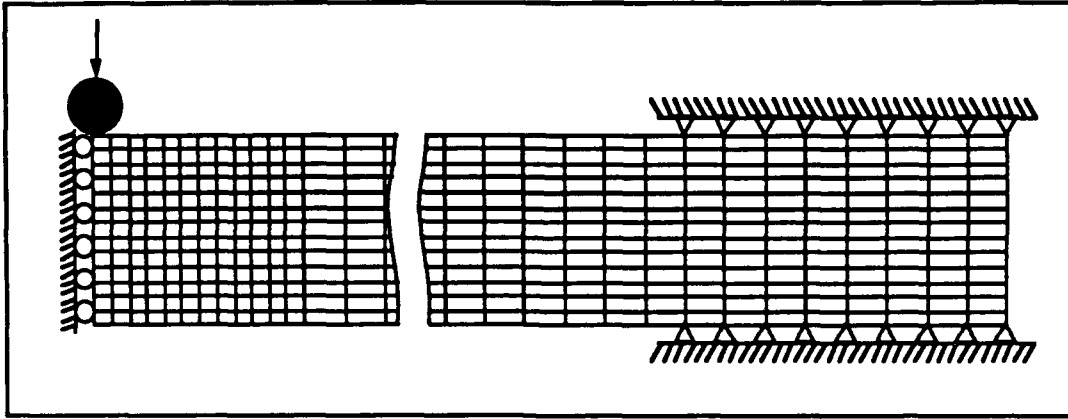


Figure 4.1: A typical finite element mesh used in the analysis.

and χ_s and χ_p are the constants defined as [61]

$$\chi_s = \frac{1 - \nu_s^2}{\pi E_s} \quad (4.7)$$

$$\chi_p = \frac{1}{\pi E_{yy}} \quad (4.8)$$

and r , ν_s , and E_s are the local radius, the Poisson's ratio, and the Young's modulus of the impactor, respectively. E_{yy} ($= E_{zz}$) is the modulus of elasticity of the impacted composite ply in the direction transverse to the fibers.

A transient dynamic finite element program was developed based on the analysis. An eight node isoparametric element was used, and a typical finite element mesh generated from the program is shown in Figure 4.1.

4.3.2 Finite Element Formulation

The stresses and strains in the laminate were calculated by a two-dimensional, transient finite element method. The equations used in the numerical calculations are presented in this section.

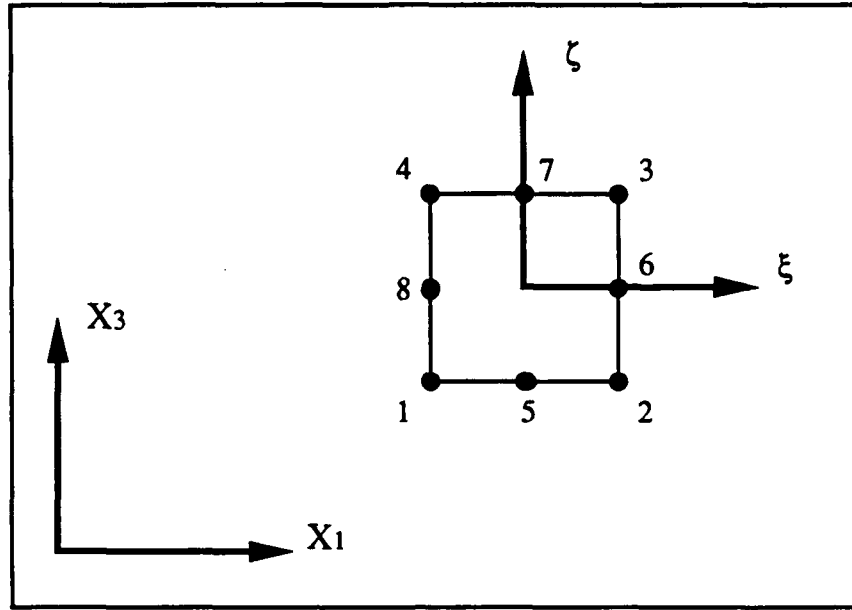


Figure 4.2: A schematic of the 8-node serendipity quadrilateral element.

Finite Element Model

In the finite element analysis, an 8-node serendipity quadrilateral element was adopted (Figure 4.2). The displacements at any point in the element (u_1, u_3) can be expressed as

$$u_q = \sum_{r=1}^8 N_r u_{qr} \quad q = 1, 3 \quad (4.9)$$

where u_{qr} are the displacements of nodal point r in the x_q direction. The shape functions of the 8-node quadrilateral elements N_r ($r = 1 \sim 8$) are given as follows [59,60]

$$\begin{aligned}
N_1 &= -\frac{1}{4} (1 - \xi) (1 - \zeta) (1 + \xi + \zeta) \\
N_2 &= -\frac{1}{4} (1 + \xi) (1 - \zeta) (1 - \xi + \zeta) \\
N_3 &= -\frac{1}{4} (1 + \xi) (1 + \zeta) (1 - \xi - \zeta) \\
N_4 &= -\frac{1}{4} (1 - \xi) (1 + \zeta) (1 + \xi - \zeta) \\
N_5 &= \frac{1}{2} (1 + \xi) (1 - \xi) (1 - \zeta) \\
N_6 &= \frac{1}{2} (1 + \xi) (1 + \zeta) (1 - \zeta) \\
N_7 &= \frac{1}{2} (1 + \xi) (1 - \xi) (1 + \zeta) \\
N_8 &= \frac{1}{2} (1 - \xi) (1 + \zeta) (1 - \zeta)
\end{aligned} \tag{4.10}$$

ξ and ζ are natural coordinates for each element (Figure 4.2) whose values vary from -1 to $+1$. The coordinates (x_1, x_3) of any point inside the element are related to the natural coordinate through the shape functions

$$x_q = \sum_{r=1}^8 N_r x_{qr} \quad q = 1, 3 \tag{4.11}$$

where x_{qr} are the coordinates of the nodal point r .

From Eq. (4.9) the strains at any point in the laminate can be written as

$$\begin{aligned}
\{\epsilon_{11}, \epsilon_{33}, 2\epsilon_{13}\}^T &= \{\epsilon_{11}, \epsilon_{33}, \gamma_{13}\}^T \\
&= \sum_{r=1}^8 [B_r] \{u_{1r}, u_{3r}\}^T
\end{aligned} \tag{4.12}$$

where ϵ_{11} and ϵ_{33} are the normal strains, ϵ_{13} are the components of shear strain tensor, and γ_{13} are the engineering shear strains. The symbols $\{ \}$ and $[]$ represent vectors and matrices, respectively. The superscript T means transposition of a vector or a matrix. The $[B_r]$ matrices is defined as

$$[\mathbf{B}_r] = \begin{bmatrix} \mathbf{N}_{r,1} & 0 \\ 0 & \mathbf{N}_{r,3} \\ \mathbf{N}_{r,3} & \mathbf{N}_{r,1} \end{bmatrix} \quad r = 1 \sim 8 \quad (4.13)$$

The symbols $\mathbf{N}_{r,i}$ represent the derivatives of the shape functions with respect to x_i ($\mathbf{N}_{r,i} = \partial \mathbf{N}_r / \partial x_i$). The stresses are related to the strains by the Eq. (4.5).

Governing Equations

By neglecting damping, the governing equation can be written as [60]

$$[M]\{\ddot{d}\} + [K]\{d\} = \{F\} \quad (4.14)$$

where $[M]$ and $[K]$ are the mass and stiffness matrices, and $\{F\}$, $\{d\}$ and $\{\ddot{d}\}$ are the force, displacement, and acceleration vectors, respectively. The mass matrix $[M]$ is the sum of the element mass matrix $[M^e]$

$$[M] = \sum_{e=1}^{N_{el}} [M^e] \quad (4.15)$$

where N_{el} is the number of total elements. The element mass matrix is the sum of the element mass submatrices

$$[M^e] = \sum_{p=1}^8 \sum_{r=1}^8 [M^e]_{pr} \quad (4.16)$$

In general, the element mass submatrices are [59]

$$[M^e]_{pr} = \int_{A^e} [\mathbf{B}_p]^T \rho [\mathbf{B}_r] da \quad p, r = 1 \sim 8 \quad (4.17)$$

where A^e is the area of element, and ρ is the ply density. For computational convenience, the mass matrix lumping procedure is used. In this method the diagonal

terms of the consistent mass matrix is scaled so that the mass is preserved. In the case of the rectangular 8-node serendipity elements used in our analysis, the element mass matrix becomes [59]

$$[M^e] = \rho \int_{A^e} \begin{bmatrix} W_1 & 0 & 0 & 0 & \cdots & 0 & 0 \\ 0 & W_1 & 0 & 0 & \cdots & 0 & 0 \\ 0 & 0 & W_2 & 0 & \cdots & 0 & 0 \\ 0 & 0 & 0 & W_2 & \cdots & 0 & 0 \\ \vdots & \vdots & \vdots & \vdots & \ddots & \vdots & \vdots \\ 0 & 0 & 0 & 0 & \cdots & W_8 & 0 \\ 0 & 0 & 0 & 0 & \cdots & 0 & W_8 \end{bmatrix} da \quad (4.18)$$

where

$$\begin{aligned} W_1 = W_2 = W_3 = W_4 &= \frac{1}{36} && \text{nodes } 1, 2, 3, 4 \\ W_5 = W_6 = W_7 = W_8 &= \frac{8}{36} && \text{nodes } 5, 6, 7, 8 \end{aligned}$$

The stiffness matrix $[K]$ is the sum of element stiffness matrices $[K^e]$

$$[K] = \sum_{e=1}^{Nel} [K^e] \quad (4.19)$$

The element stiffness matrix is the sum of the element stiffness submatrices

$$[K^e] = \sum_{p=1}^8 \sum_{r=1}^8 [K^e]_{pr} \quad (4.20)$$

where

$$[K^e]_{pr} = \int_{A^e} [\mathbf{B}_p]^T [\mathbf{D}] [\mathbf{B}_r] da \quad p, r = 1 \sim 8 \quad (4.21)$$

The elasticity matrix $[\mathbf{D}]$ in Eq. (4.21) is same as in Eq. (4.5).

In the present problem with the absence of the body forces, the contact force caused by the impactor is the only external load to be considered. The contact force vector $\{F\}$ is defined as

$$\{F\} = f\{U\} \quad (4.22)$$

where $\{U\}$ is a unit vector whose component is -1 in the direction of the contact force. All other components of $\{U\}$ are zero and f is the magnitude of the contact force which is a function of time.

At time $t + \Delta t$, Eq. (4.14) is written as

$$[M]\{\ddot{d}\}^{t+\Delta t} + [K]\{d\}^{t+\Delta t} = \{F\}^{t+\Delta t} \quad (4.23)$$

where the superscript refers to time. The Newmark method will be employed to obtain the solutions to this equation. Accordingly, the velocity and acceleration vectors at time $t + \Delta t$ are written as

$$\{\dot{d}\}^{t+\Delta t} = \{\dot{d}\}^t + (1 - \lambda)\Delta t\{\ddot{d}\}^t + \lambda\Delta t\{\ddot{d}\}^{t+\Delta t} \quad (4.24)$$

and

$$\{\ddot{d}\}^{t+\Delta t} = \frac{1}{\beta\Delta t^2}\{d\}^{t+\Delta t} - \frac{1}{\beta\Delta t^2}\{d\}^t - \frac{1}{\beta\Delta t}\{\dot{d}\}^t - \frac{\frac{1}{2} - \beta}{\beta}\{\ddot{d}\}^t \quad (4.25)$$

The parameters β and λ are constants whose values depend on the finite difference scheme used in the calculations. The constant-average-acceleration method was employed, which is implicit and unconditionally stable. For this method β is $1/4$ and λ is $1/2$. Although the velocity vector is not required in Eq. (4.24), it is presented here because it will be needed subsequently. By substituting Eq. (4.25) into Eq. (4.23), we obtain

$$[\hat{K}]\{d\}^{t+\Delta t} = \{\hat{F}\}^{t+\Delta t} \quad (4.26)$$

where $[\hat{K}]$ is the effective stiffness matrix, and $\{\hat{F}\}^{t+\Delta t}$ is the effective force vector. These parameters are defined as

$$[\hat{K}] = \frac{1}{\beta \Delta t^2} [M] + [K] \quad (4.27)$$

and

$$\{\hat{F}\}^{t+\Delta t} = \{H\}^t + \{F\}^{t+\Delta t} \quad (4.28)$$

where $\{H\}^t$ is the following vector

$$\{H\}^t = [M] \left(\frac{1}{\beta \Delta t^2} \{d\}^t + \frac{1}{\beta \Delta t} \{\dot{d}\}^t + \frac{1-2\beta}{2\beta} \{\ddot{d}\}^t \right) \quad (4.29)$$

Referring to Eq. (4.26), it is noted that the displacements, velocities, and accelerations at time t are known at every point inside the plate. Hence, the unknowns in Eq. (4.26) are the displacement vector $\{d\}^{t+\Delta t}$ and the force vector $\{F\}^{t+\Delta t}$. To determine these two variables, an additional expression is needed. This expression is described below.

Solution Procedure

Combining Eq. (4.26) with Eq. (4.28), results in

$$[\hat{K}]\{d\}^{t+\Delta t} = \{H\}^t + \{F\}^{t+\Delta t} \quad (4.30)$$

The displacement vector $\{d\}^{t+\Delta t}$ is expressed as the sum of the displacements due to the force $\{H\}^t$ and the contact force $\{F\}^{t+\Delta t}$

$$\{d\}^{t+\Delta t} = \{d\}_H^{t+\Delta t} + \{d\}_F^{t+\Delta t} \quad (4.31)$$

Eq. (4.30) and Eq. (4.31) give

$$[\hat{K}](\{d\}_H^{t+\Delta t} + \{d\}_F^{t+\Delta t}) = \{H\}^t + \{F\}^{t+\Delta t} \quad (4.32)$$

From Eq. (4.32),

$$[\hat{K}]\{d\}_H^{t+\Delta t} = \{H\}^t \quad (4.33)$$

and

$$[\hat{K}]\{d\}_F^{t+\Delta t} = \{F\}^{t+\Delta t} \quad (4.34)$$

In order to determine the displacement vectors $\{d\}_H$ and $\{d\}_F$ in Eq. (4.31)-(4.32), the two force vectors $\{H\}$ and $\{F\}$ at every nodal point must be specified. At each nodal point $\{H\}$ is given by Eq. (4.29) and $\{F\}$ equals to zero except at the point of impact where $\{F\} = f\{U\}$ [see Eq. (4.22)]. The solutions of Eq. (4.30)-(4.31) are obtained in two steps. First, the forces $\{H\}$ and the displacements $\{d\}_H$ are calculated from Eq. (4.29) and (4.33). This calculation is straightforward, since the mass matrix $[M]$, the time step Δt , as well as the displacement $\{d\}$, the velocity $\{\dot{d}\}$, and acceleration $\{\ddot{d}\}$ at time t are all known. Second, the contact force vector $\{F\}$ and the displacement $\{d\}_F$ are calculated as follows. At time $t + \Delta t$, Eq. (4.22) is written as

$$\{F\}^{t+\Delta t} = f^{t+\Delta t}\{U\} \quad (4.35)$$

where $f^{t+\Delta t}$ is the contact force at time $t + \Delta t$. Eq. (4.34) and (4.35) yield

$$[\hat{K}]\{d\}_F^{t+\Delta t} = f^{t+\Delta t}\{U\} \quad (4.36)$$

For a unit contact force ($f^{t+\Delta t} = 1$), Eq. (4.36) becomes

$$[\hat{K}]\{d\}_U^{t+\Delta t} = \{U\} \quad (4.37)$$

where $\{d\}_U^{t+\Delta t}$ is the displacement caused by the unit contact force. For a given effective stiffness matrix the displacement vector $\{d\}_U^{t+\Delta t}$ can be calculated from Eq. (4.37). From Eqs. (4.37) and (4.38), it can be seen that $\{d\}_F^{t+\Delta t}$ and $\{d\}_U^{t+\Delta t}$ can be related by

$$\{d\}_F^{t+\Delta t} = f^{t+\Delta t} \{d\}_U^{t+\Delta t} \quad (4.38)$$

Eqs. (4.31) and (4.38) give

$$\{d\}^{t+\Delta t} = \{d\}_H^{t+\Delta t} + f^{t+\Delta t} \{d\}_U^{t+\Delta t} \quad (4.39)$$

In Eq. (4.39), the unknowns are the displacement vector $\{d\}$ and the scalar contact force f at time $t + \Delta t$. During impact the contact force can be expressed as

$$\begin{aligned} \alpha^{t+\Delta t} &= f^{t+\Delta t} (\chi_s + \chi_p) \left\{ 1 - \ln [f^{t+\Delta t} r (\chi_s + \chi_p)] \right\} & \text{when } \delta_S \geq \delta_C \\ 0 &= f^{t+\Delta t} & \text{when } \delta_S < \delta_C \end{aligned} \quad (4.40)$$

$\chi_s, \chi_p, \delta_S, \delta_C$, and r are known constants defined previously. α is the indentation depth which varies with time. At time $t + \Delta t$ this depth is

$$\alpha^{t+\Delta t} = \delta_S^{t+\Delta t} - \delta_C^{t+\Delta t} \quad (4.41)$$

$\delta_C^{t+\Delta t}$ is the displacement of the center of the midsurface of the plate in the direction of the impact. With the use of Eq. (4.39), δ_C can be expressed as

$$\delta_C^{t+\Delta t} = \delta_{CH}^{t+\Delta t} - f^{t+\Delta t} \delta_{CU}^{t+\Delta t} \quad (4.42)$$

where $\delta_C^{t+\Delta t}$, $\delta_{CH}^{t+\Delta t}$ and $\delta_{CU}^{t+\Delta t}$ are the magnitudes of the displacements at the center point of the mid-surface in the direction of impact at time $t + \Delta t$. $\delta_S^{t+\Delta t}$ is the position of the center point of the impactor. At time $t + \Delta t$, the magnitude of $\delta_S^{t+\Delta t}$ is determined by Newton's second law (See Appendix B)

$$\begin{aligned}\delta_S^{t+\Delta t} &= \frac{1}{m} \int_0^{t+\Delta t} \int_0^{t+\Delta t} f dt dt \\ &= \delta_S^t + v_1 \Delta t - \frac{1}{6m} (2f^t + f^{t+\Delta t}) \Delta t^2\end{aligned}\tag{4.43}$$

where m is impactor mass and v_1 is the impactor velocity at time t . By combining Eqs. (4.40)-(4.43), the contact force can be expressed as follows:

$$\begin{aligned}0 &= f^{t+\Delta t} (\chi_s + \chi_p) \left\{ 1 - \ln [f^{t+\Delta t} r (\chi_s + \chi_p)] \right\} \\ &\quad - \delta_S^t - v_1 \Delta t + \frac{1}{6m} (2f^t + f^{t+\Delta t}) \Delta t^2 \\ &\quad + (\delta_{CH}^{t+\Delta t} + f^{t+\Delta t} \delta_{CU}^{t+\Delta t}) \quad \text{when } \delta_S \geq \delta_C \\ 0 &= f^{t+\Delta t} \quad \text{when } \delta_S < \delta_C\end{aligned}\tag{4.44}$$

Newton-Raphson method was used to calculate the contact force $f^{t+\Delta t}$ in Eq. (4.44). Once the value of $f^{t+\Delta t}$ is known, the displacement vector $\{d\}$ at time $t + \Delta t$ is calculated from Eq. (4.39), and the velocity and acceleration vector at time $t + \Delta t$ are calculated from Eqs. (4.24) and (4.25). From the known displacements, the strains are calculated from Eq. (4.12), and, from the known strains, the stresses are obtained from Eq. (4.5). The aforementioned procedures are repeated at each time step.

Once the stresses are calculated, initial damage of the composites can be determined by substituting the stresses into an appropriately selected failure criterion. Accordingly, the accuracy of the prediction of damage relies on the proper selection of the failure criterion and the accuracy of information regarding the stresses in the

laminate and the ply strength distributions within the composites. It is noted that the stresses thus calculated from the analysis are associated directly with the mechanical loading. There also exists a certain amount of thermal residual stresses in composites resulting from fabrication which could inherently weaken the strength of the material and its ability to sustain the impact. The thickness and ply orientation of the composite could also affect the ply strength distributions within the composite [62–65]. Hence, in order to accurately predict the initial impact damage, the in situ strength distribution of composites as well as the transient dynamic stress distributions should be considered in conjunction with the failure criterion.

4.3.3 Failure Analysis

The major focus of the failure analysis is to numerically simulate the impact damage resulting from the line-loading impact. Hence, the proposed failure analysis concentrates on predicting the occurrence and location of the critical matrix cracks and the initiation of delamination and micro-cracks.

Initial Damage

A matrix failure criterion is utilized to determine the initial failure mode of impact damage, the critical matrix cracks. In this study, a three-dimensional matrix failure criterion originally proposed by Hashin [54] was adopted and modified for predicting the matrix cracks. The initial impact damage is predicted whenever the calculated stresses satisfy the criterion and the corresponding location is associated with the place where the matrix crack occurs.

Here, based on line-loading impact, there are only three major stress components that can contribute to initial matrix cracking in the 90 degree layers in the plane strain condition, as shown schematically in Figure 4.3. These are the interlaminar shear stress σ_{13} ($= \sigma_{yz}$), in-plane tensile stress σ_{11} ($= \sigma_{yy}$), and out-of-plane normal stress σ_{33} ($= \sigma_{zz}$). However, it will be shown later that the out-of-plane normal stress σ_{33} is found to be very small in comparison with the other two stress components

during the entire impact event. Hence, the matrix failure criterion can be simplified as ($\sigma_{yy} \geq 0$),

$$\left(\frac{{}^n\bar{\sigma}_{yy}}{{}^nY_t}\right)^2 + \left(\frac{{}^n\bar{\sigma}_{yz}}{{}^nS_i}\right)^2 = e_M^2 \quad \begin{cases} e_M \geq 1 & \text{Failure} \\ e_M < 1 & \text{No failure} \end{cases} \quad (4.45)$$

where the subscript of x and y are the local coordinates of the n -th layer parallel and normal to the fiber directions, respectively, and z is the out-of-plane direction. nY_t and nS_i are the in situ ply transverse tensile strength and interlaminar transverse shear strength within the n -th ply of laminate under consideration, respectively [62,63]. ${}^n\bar{\sigma}_{yz}$ and ${}^n\bar{\sigma}_{yy}$ are the averaged interlaminar transverse shear stress and the averaged in-plane transverse tensile stress, respectively, within the n -th ply, which can be expressed as

$${}^n\bar{\sigma}_{yz} = \frac{1}{h_n} \int_{t_{n-1}}^{t_n} \sigma_{yz} dz \quad (4.46)$$

and

$${}^n\bar{\sigma}_{yy} = \frac{1}{h_n} \int_{t_{n-1}}^{t_n} \sigma_{yy} dz \quad (4.47)$$

where t_n and t_{n-1} are the upper and lower interfaces of the n -th ply or ply group in the laminate and h_n is the thickness of the ply or ply group.

Based on Eq. (4.45), the determination of the initial impact damage strongly depends on the in situ strength of the material within the laminate. It is well known that the strengths of a single ply within a laminate can be substantially different from the strengths measured directly from a unidirectional composite [62–65]; the difference has been attributed to the thermal residual stresses, ply orientation, and the thickness of the laminate. However, the actual strength distributions of a laminate as a function of these parameters are still not well established.

Here, an empirical relationship of the ply transverse tensile strength within a laminate as a function of the laminate thickness and stacking sequence was adopted, which was proposed by Chang and Lessard [62]. The relationship can be expressed as

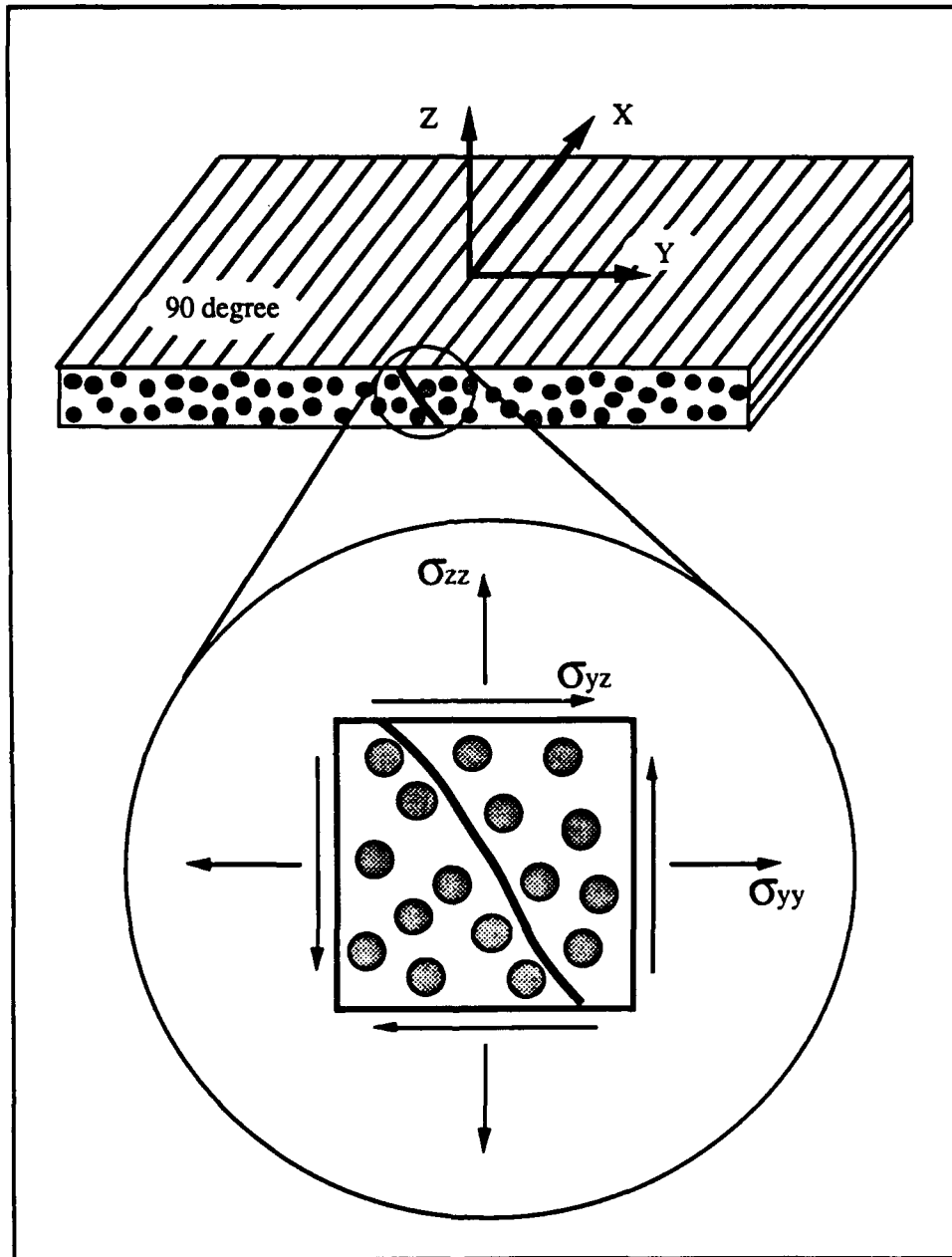


Figure 4.3: The stress components based on the plane strain condition contributing to transverse matrix cracking.

$$Y_t = Y_t^o \left(1 + A \frac{\sin(\Delta\theta)}{M_c^B} \right) \quad (4.48)$$

where Y_t is the in situ ply transverse tensile strength of the laminate, $\Delta\theta$ is the maximum ply angle change between the ply or the ply group under consideration and its neighboring plies, and M_c is the total number of consecutive (clustered) ply groups that are considered. Y_t^o is the transverse tensile strength of a $[90_n]_s$ composite ($n \geq 6$). The parameters of A and B are constants which can be determined from experiment [62].

Note that the strength distribution thus determined corresponds to the mechanical load that causes the first matrix crack in the laminate. The distribution depends on the manufacturing process, ply orientation and thickness of the laminate. Hence, the value of Y_t determined from Eq. (4.48) can be used in Eq. (4.45) for predicting initial impact damage.

However, the interlaminar shear strength distribution within a laminated composite has not yet been fully studied. It is still not understood how the strength distribution is affected by the stacking sequence and the laminate thickness, but such distribution has been frequently assumed to be in the same order of magnitude as the ply shear strength distribution within a laminate. Accordingly, here, it was assumed that the interlaminar shear strength normal to the fiber direction is equivalent to in situ ply shear strength S within the laminate. The distribution of the in situ ply shear strength S has been observed, experimentally, to exhibit similar behavior as the in situ transverse tensile strength Y_t [62]. Hence, the expression for the in situ ply shear strength distribution proposed by Chang and Lessard [62] was adopted for estimating the interlaminar shear strength distribution normal to the fiber direction within a laminate. The expression similar to Eq. (4.48) can be written as

$$S = S^o \left(1 + C \frac{\sin(\Delta\theta)}{M_c^D} \right) \quad (4.49)$$

where S is the in situ ply shear strength of a laminate and S^o is the ply shear strength measured from a unidirectional composite with more than eight layers. Again, C and D are the material constants which can be determined from experiment [62].

Delamination Growth and Micro-cracks

Once the critical matrix crack is predicted, the next step is to discover if such a crack could initiate delaminations and micro-cracks in a composite during impact. Accordingly, a post-failure analysis was performed to simulate the subsequent response of the composite containing the initial damage. The analysis was executed by reducing the material stiffnesses within the damaged element where the critical matrix crack was predicted. For matrix cracking, the material properties within the damaged layer were reduced as follows [62,66,67]

$${}^n[\mathbf{D}] = \begin{bmatrix} E_x & 0 & 0 & 0 & 0 & 0 \\ 0 & 0 & 0 & 0 & 0 & 0 \\ 0 & 0 & E_z & 0 & 0 & 0 \\ 0 & 0 & 0 & 0 & 0 & 0 \\ 0 & 0 & 0 & 0 & G_{xz} & 0 \\ 0 & 0 & 0 & 0 & 0 & G_{xy} \end{bmatrix} \quad (4.50)$$

where E_x and E_z are the tensile moduli of the n -th layer along the fibers and normal to the middle plane, respectively. G_{xz} and G_{xy} are the out-of-plane shear moduli of the n -th layer. The expression for the undamaged material properties of ${}^n[\mathbf{D}]$ is given in Appendix A.

Eq. (4.50) indicates that the damaged element can not sustain any additional transverse tensile stress and out-of-plane shear stress due to the presence of the crack. This reduction is reasonable within the neighborhood of the crack for a quantitative study, although a dynamic fracture analysis may result in more qualitative findings. The stresses and strains were then recalculated using Eq. (4.5) at the same instant in time as the occurrence of the critical matrix cracks. Accordingly, the redistributed

stress distributions near the neighborhood of the critical matrix cracks could be studied.

4.4 VERIFICATION

During the investigation, a computer code designated as "2DIMPACT" was developed based on the proposed analysis. In order to verify the calculations of stresses and strains from the code, comparisons were made between the existing analytical solutions and the calculated results from the code. The stress distributions through the thickness of a composite plate subjected to quasi-static cylindrical bendings were calculated and compared with the analytical solutions obtained by Pagano [68]. Figure 4.4 shows the calculated results from the code and the analytical solutions [68]. Excellent agreements were obtained. Furthermore, the dynamic response of a cantilever beam subjected to a periodic loading was determined from the code and compared with the analytical solutions in Figure 4.5 [69]. Again, the calculations agreed with the analysis very well.

Unfortunately, no analytical solutions of the transient dynamic stress distributions due to line-loading impact were available in the literature for comparison. Hence, the solutions of a beam subjected to a line loading impact based on the code were compared to the solutions of the beam subjected to a point loading impact. It is reasonable to consider that if the width of the beam is narrow enough, the response of the beam and the contact force distribution would be consistent in both cases. The solutions resulting from the point-loading impact were calculated from the "IMPACT" code which was developed previously by Wu *et al* [13,16].

Figure 4.6 shows the central deflections of the beam for both loading cases at a given impact energy. The two curves coincide with each other very well. The contact force distributions as a function of duration of time for both cases are also shown in Figure 4.6. Again, based on two completely different contact algorithms, the two calculated contact force distributions were very consistent with each other

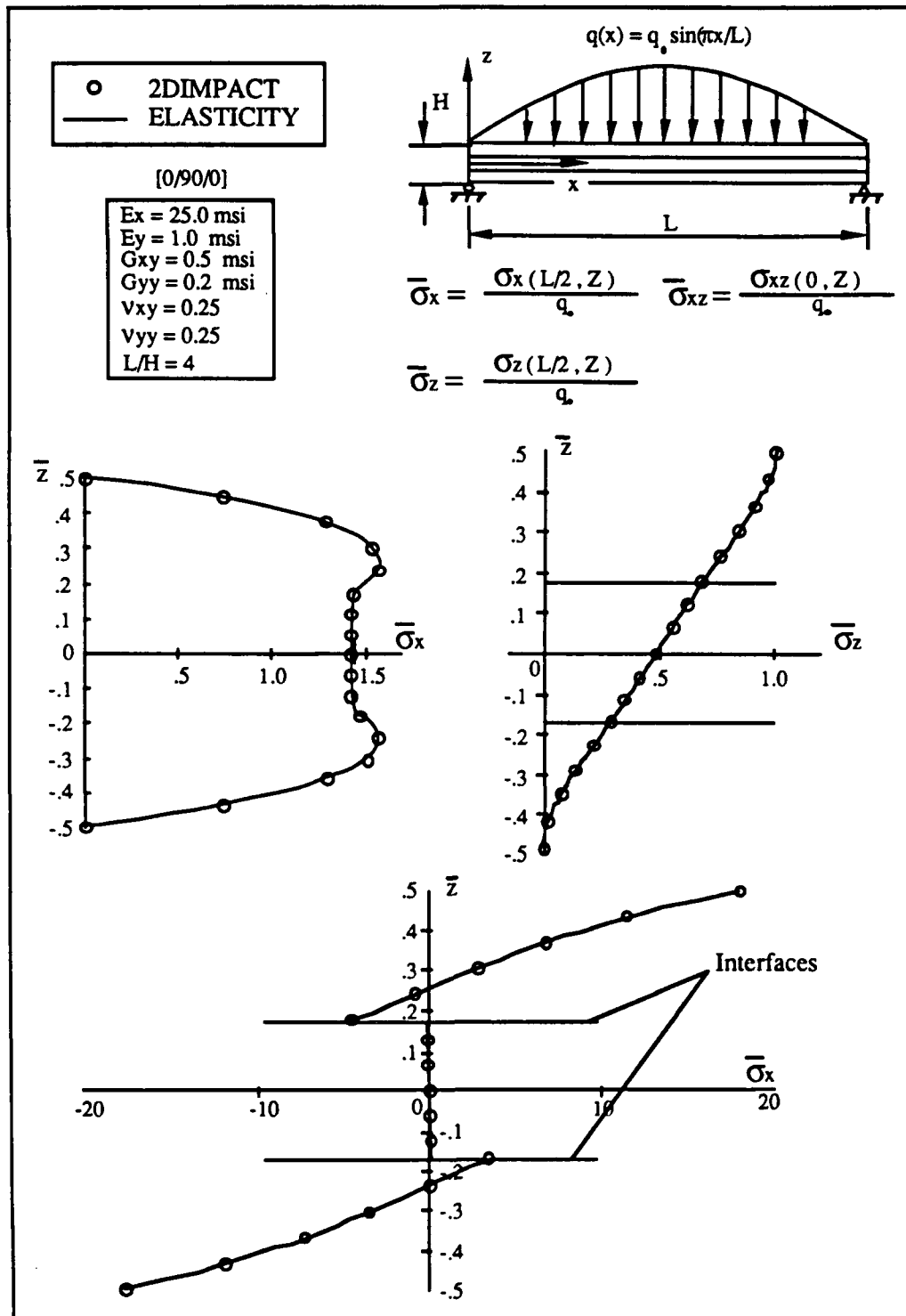


Figure 4.4: Comparison between the calculated and the analytical solutions for a laminated composite panel subjected to cylindrical bending. The analytical solutions are taken from [68].

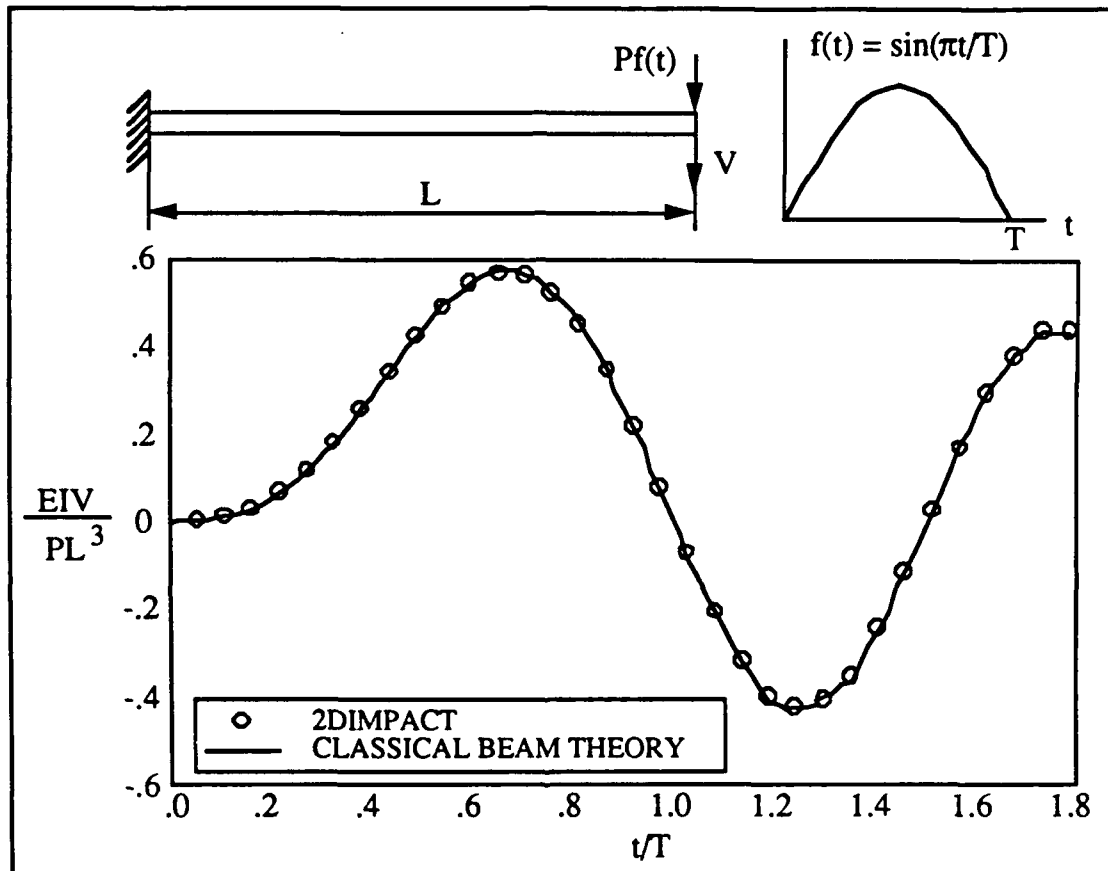


Figure 4.5: Comparison between the calculated and the analytical solutions for a laminated composite panel subjected to periodic loading. The analytical solutions are taken from [69].

and exhibited a very similar pattern. Accordingly, it was believed that the code could provide accurate information about the stresses and deformations inside the structures during impact. Hence, numerical solutions were generated from the code to compare with the test results, and the results of the comparison are presented in the next section.

4.5 COMPARISON

Numerical simulations of the specimens under the test condition are performed by using the code. The material properties of T300/976 Graphite/Epoxy used in the calculations are summarized in Table 4.1. The results of the calculations compared to the experimental data are presented as follows:

4.5.1 Initial Impact Damage

To predict the initial matrix cracking, the test results of the $[0_6/90_4/0_6]$ and $[0_3/\pm 45_4/90_3]$ specimens are first simulated by the code. The weight and velocity of the impactor used in the calculations are the same as the test conditions. Figures 4.7 and 4.8 show the peaks of the values of e_M in 90 degree layers (matrix failure criterion) as a function of position for $[0_6/90_4/0_6]$ and $[0_3/\pm 45_4/90_3]$ specimens under the test condition respectively. For $e_M \geq 1$, matrix cracking is predicted. For instance, Figure 4.7 indicates that there are two possible locations in 90 degree layers for matrix cracking at the given test condition ($M = 1.142$ kg/m and $V = 14.5$ m/sec); one is close to the central impacted area at $t = 351$ μ sec, and the other is near the clamping areas at $t = 423$ μ sec. The central crack occurs much earlier than the others near the boundaries. Apparently, the former is the direct result of impact from the impactor and the latter is primarily due to bending and stretching of the plates resulting from the constraints of the boundaries.

Surprisingly, a rather different strength ratio distribution (e_M) is obtained for the

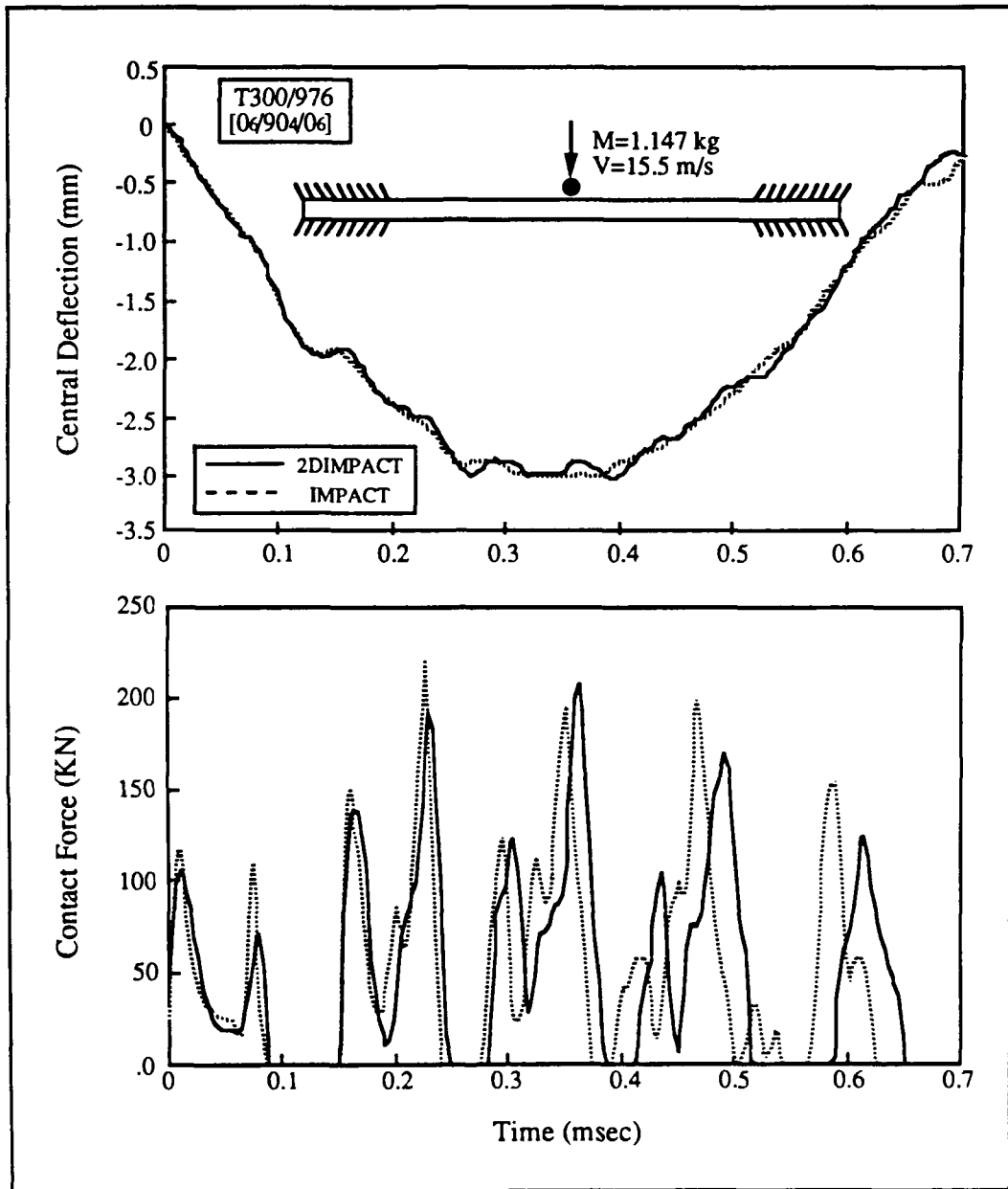


Figure 4.6: Comparison of the calculations between the “2DIMPACT” and “IMPACT” [13,16] for a composite beam subjected to a line-loading impact or a point-loading impact, respectively. Top: the central deflection of the beam for both loading cases at a given impact energy. Bottom: the contact distribution as a function of the duration of time for both loading cases.

Moduli	Symbol (unit)	
In-plane longitudinal modulus	E_{xx} (Gpa)	156
In-plane transverse modulus	E_{yy} (Gpa)	9.09
In-plane shear modulus	G_{xy} (Gpa)	6.96
Out-of-plane shear modulus	G_{yz} (Gpa)	3.24
In-plane Poisson's ratio	ν_{xy}	0.228
Out-of-plane Poisson's ratio	ν_{yz}	0.400
Density	ρ (kg/m ³)	1540

Strength	Symbol (unit)	
Longitudinal tension	X_T (Mpa)	1520
Longitudinal compression	X_C (Mpa)	1590
Transverse tension	Y_T^* (Mpa)	45
Transverse compression	Y_C (Mpa)	252
Ply longitudinal shear	S^* (Mpa)	105
Strength parameters (From Eq. 4.48)	A^*	1.3
Strength parameters (From Eq. 4.48)	B^*	0.7
Strength parameters (From Eq. 4.49)	C^*	2.0
Strength parameters (From Eq. 4.49)	D^*	1.0

Impactor	Symbol (unit)	
Modulus	E_s (Gpa)	207
Poisson's ratio	ν_s	0.3
Nose radius	r (mm)	1.5

* Data taken from [62]

Table 4.1: Material properties of T300/976 used in the calculations.

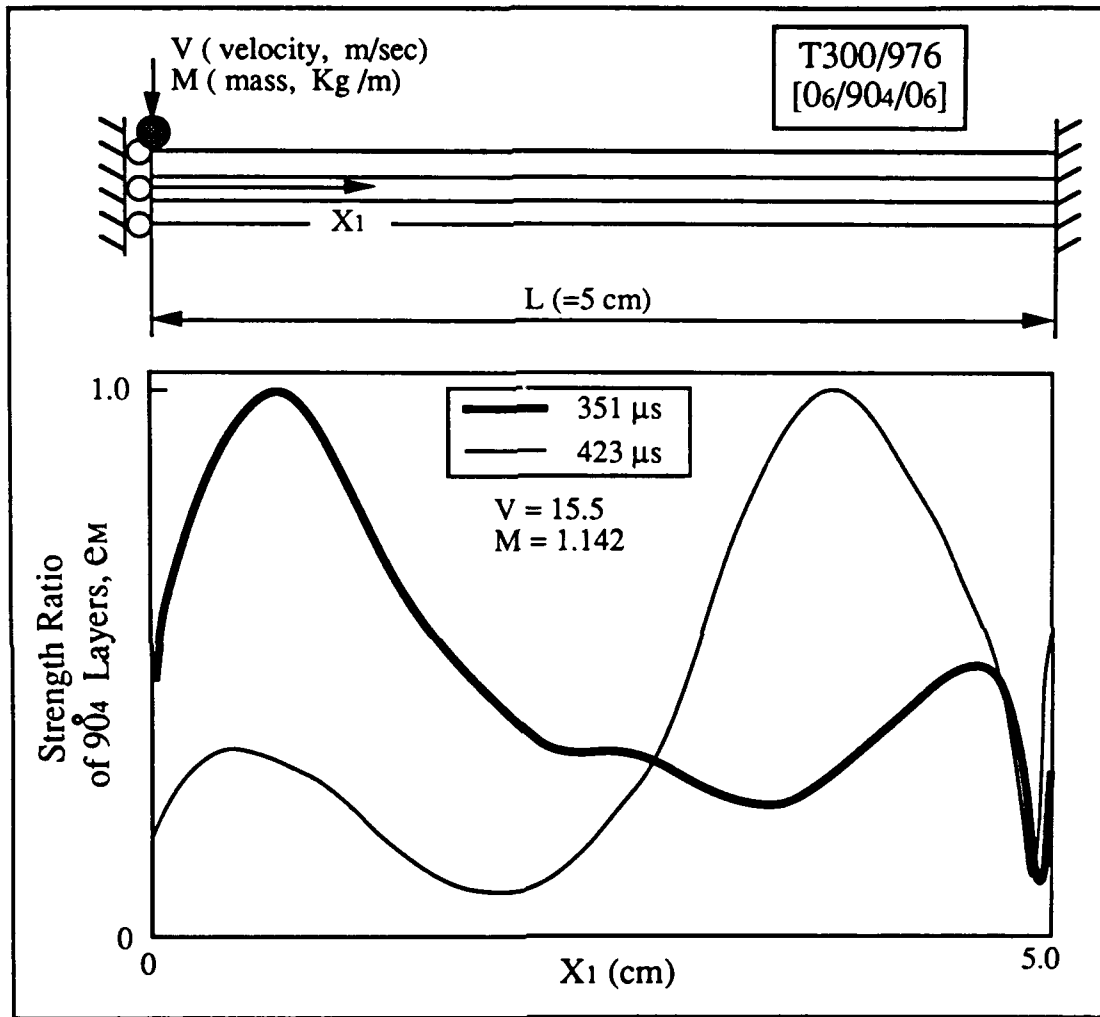


Figure 4.7: The calculated maximum strength ratios of e_M (failure criterion) for a $[0_6/90_4/0_6]$ specimen occurring at two separate instants.

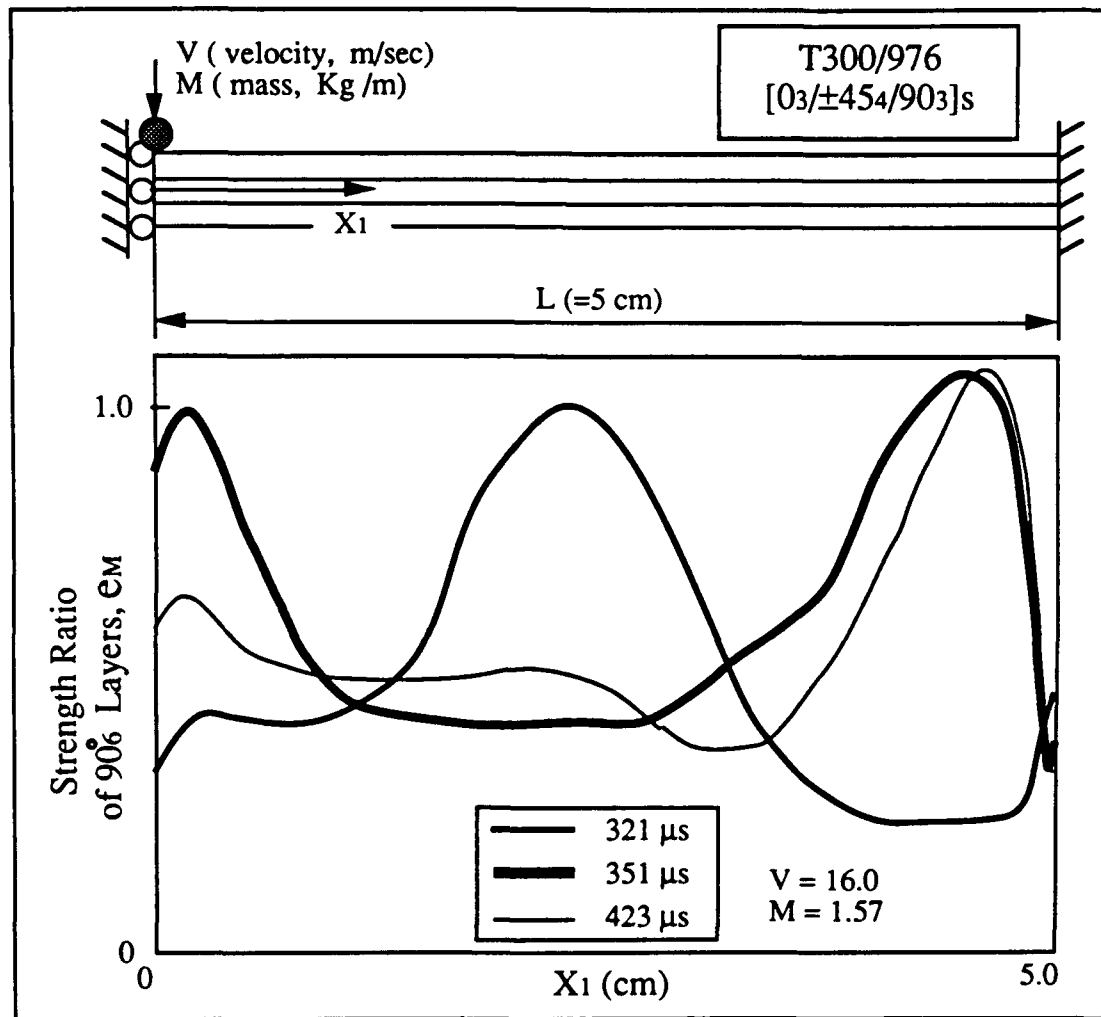


Figure 4.8: The calculated maximum strength ratios of e_M (failure criterion) for a $[0_3/\pm 45_4/90_3]_s$ specimen occurring at three separate instants.

$[0_3/\pm 45_4/90_3]$, composites. No matrix cracking is predicted in ± 45 degree layers under the given loading condition. Besides the two possible locations for matrix cracking similar to those of $[0_6/90_4/0_6]$ composites, an additional peak of the strength ratio ($e_M = 1$) occurs first at time $t = 321 \mu\text{sec}$ and appears at a quarter of the test span of the specimen, measured from the boundary (about half the distance from the center of the specimen to the boundary). The location of the critical matrix cracks corresponds to the position where e_M reaches the unity. Figure 4.9 shows the locations of the predicted critical cracks compared to the experimental data for $[0_6/90_4/0_6]$ and $[0_3/\pm 45_4/90_3]$, composites. The experimental results in Figure 4.9 were taken from an average of the measured data of three to four tested specimens.

It is worth noting that the critical matrix crack near the central region of the specimens does not occur directly beneath the impacted area, but a distance from it. In order to understand the phenomenon, the distributions of the stresses near the central impacted region were carefully studied. It was found, for instance, in $[0_6/90_4/0_6]$ specimens that the interlaminar shear stress and the in-plane transverse tensile stress in the 90 degree layers reach the peaks at $t = 351 \mu\text{sec}$ near the location where the critical matrix occurs, but the out-of-plane normal tensile stress σ_{33} is always negligibly small compared to the others and decreases rapidly once it is away from the impacted area (see Figure 4.10). Apparently, the interlaminar shear stress and the in-plane transverse tensile stress are the dominant stresses causing the critical matrix cracking during impact. Thus, the effect of the out-of-plane normal tensile stress on the initiation of impact damage is negligible. As a result, without out-of-plane normal stress, delamination initiation which requires the combination of out-of-plane normal stress and interlaminar shear stress would most unlikely occur earlier than the matrix failure, indicating that the critical matrix cracking is the initial failure mode.

Furthermore, the distributions of interlaminar shear stress across the thickness at various locations were also calculated and studied. Figure 4.11 shows the interlaminar shear stress distributions at six different cross sections near the central impacted areas at time $t = 351 \mu\text{sec}$. Interestingly, the distributions varied considerably from cross

Initial Matrix Crack Locations

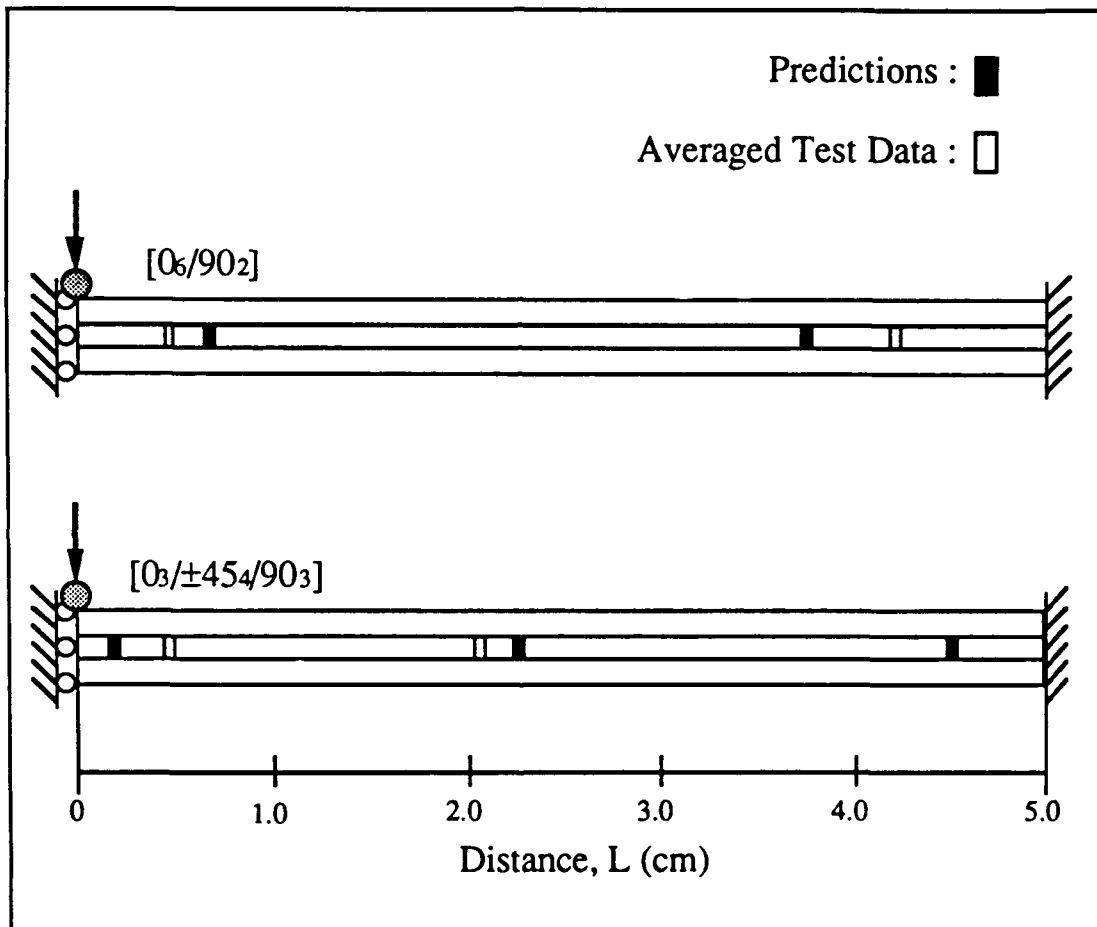


Figure 4.9: Comparison of the locations of the initial matrix cracks between the averaged data and the predictions.

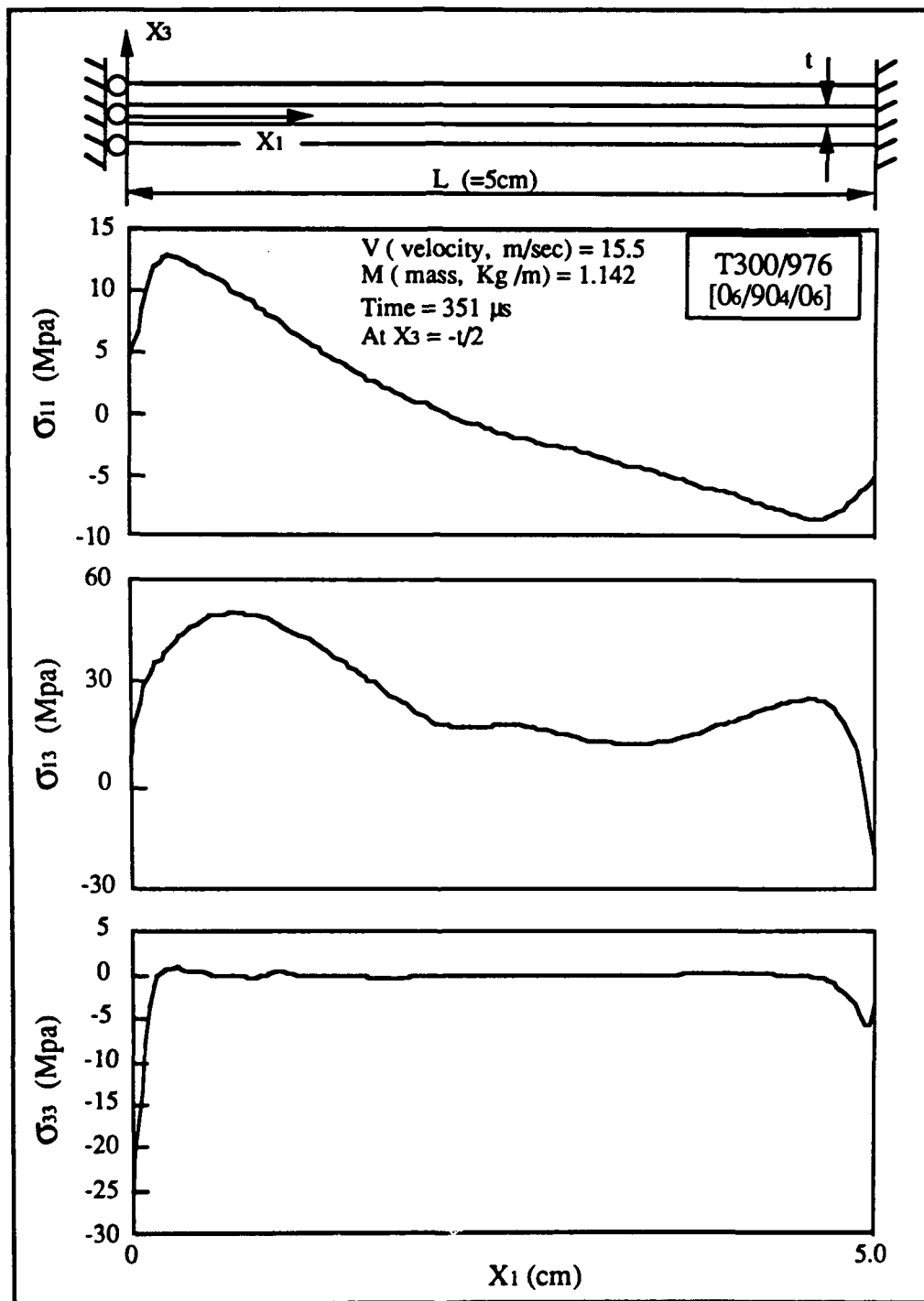


Figure 4.10: The instantaneous stress distributions near the center impacted area of a [0₆/90₄/0₆] specimen.

section to cross section, and the shear distribution in 90 degree layer reached the maximum at the location near the critical matrix crack. The magnitude of such shear distribution is considerably higher than the one obtained statically by a line-loading force under the same out-of-plane deflection as shown in Figure 4.12. The difference can be attributed to the transient dynamic effect. Clearly, the interlaminar shear stress distribution is strongly influenced by the impact loading and, hence, is a function of the velocity and the mass of the impactor as well.

The distribution of the transverse normal stress at time $t = 351 \mu\text{sec}$, given in Figure 4.10, was also compared with a static solution based on the same amount of deflection corresponding to the dynamic case at $t = 351 \mu\text{sec}$. The comparison is shown in Figure 4.13. Apparently, the distribution is not very sensitive to dynamic effect and is primarily attributed to bending and stretching. Hence, it can be concluded that the initial impact damage is governed by transient dynamic interlaminar shear stress and in-plane normal stress. The location and the amount of energy required to cause the initial impact damage strongly depend on the velocity and mass of the impactor and the geometry and boundary condition of the specimen.

A very consistent prediction of the location of the critical matrix cracks for each possible 90 degree layer in the laminates was also obtained for specimens with other ply orientations and geometries. The results of the comparison are summarized in Figure 4.14. All of these critical matrix cracks located near the central impacted region of the specimens were embedded inside the laminates and inclined of an angle about 45 degrees from the loading direction. The inclination of the matrix cracks is due to the combination of the interlaminar shear stress and the transverse normal stress in the 90 degree layers.

However, numerical simulations were also performed on $[90_3/0_3/90_3]$ specimens in which the critical cracks were found experimentally in the outer 90 degree layers. At a given mass and velocity of the impactor, the code predicted that a critical matrix crack would be located at the center of the specimen in the bottom 90 degree layers. The prediction also coincided with the experiment very well. It was found that the

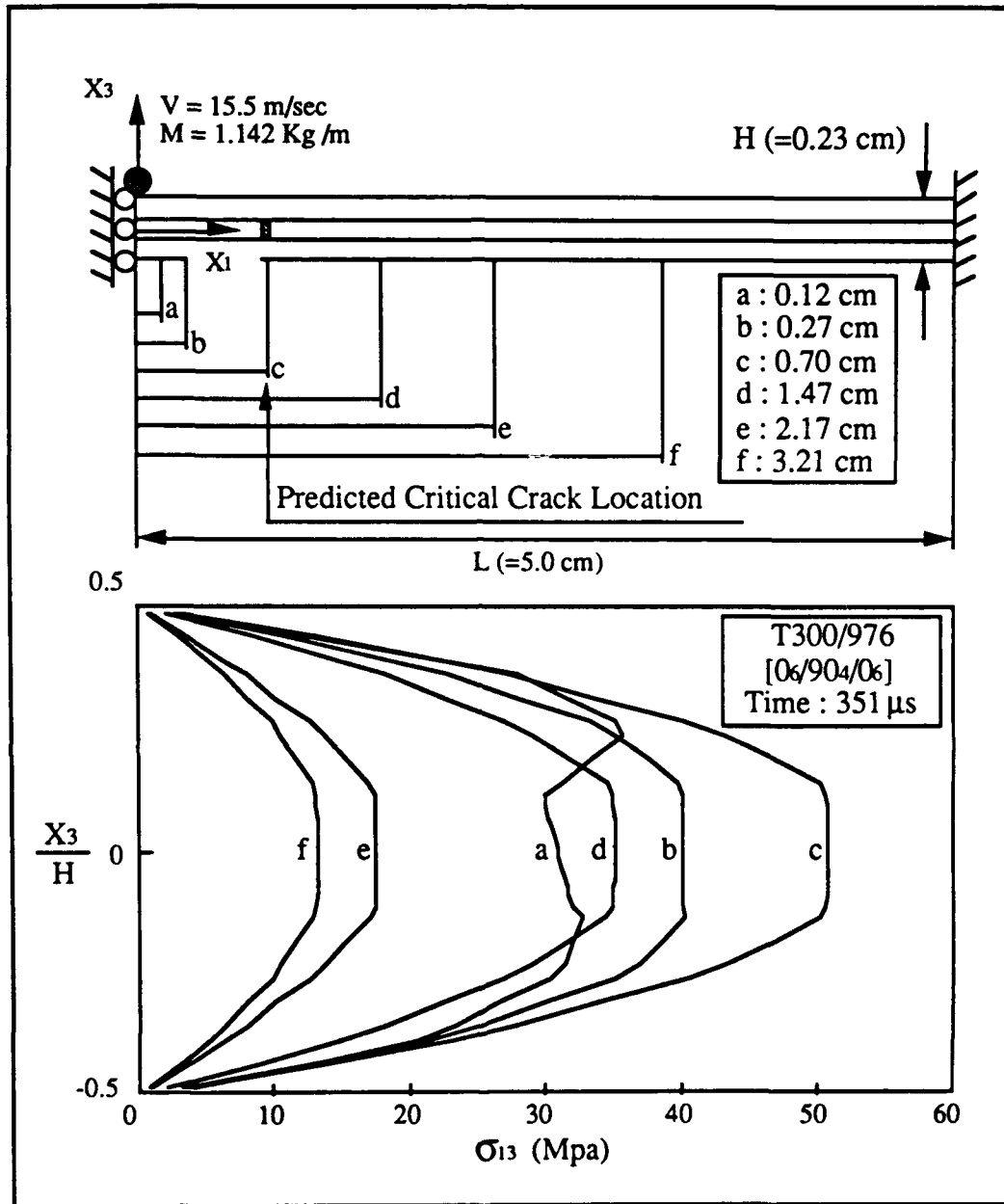


Figure 4.11: The calculated interlaminar shear stress distribution across the thickness at six different cross sections near the central impacted areas of a $[0_6/90_4/0_6]$ specimen at the time corresponding to the first critical matrix crack.

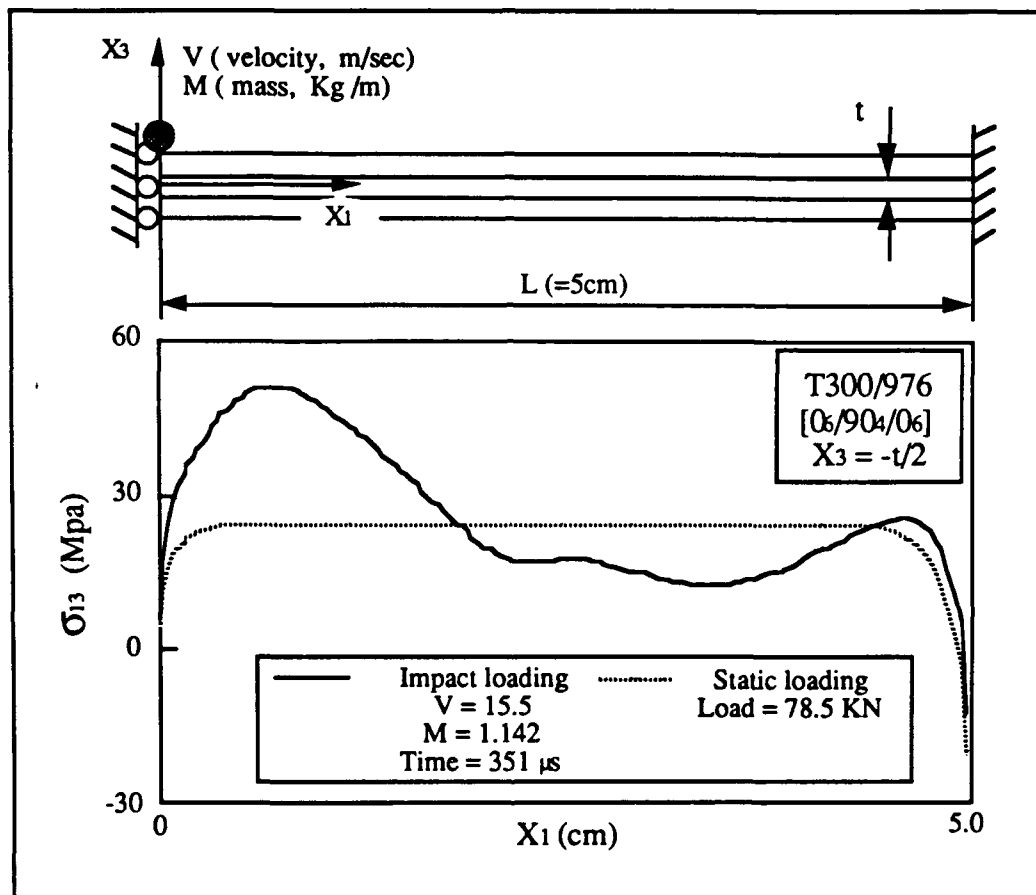


Figure 4.12: Comparison of the interlaminar shear stress distribution along the lower 90/0 interface of a $[0_6/90_4/0_6]$ composite specimen between the static and the transient dynamic calculations. The static load was applied to generate an equal amount of lateral deflection as that of the dynamic case at the compared instant.

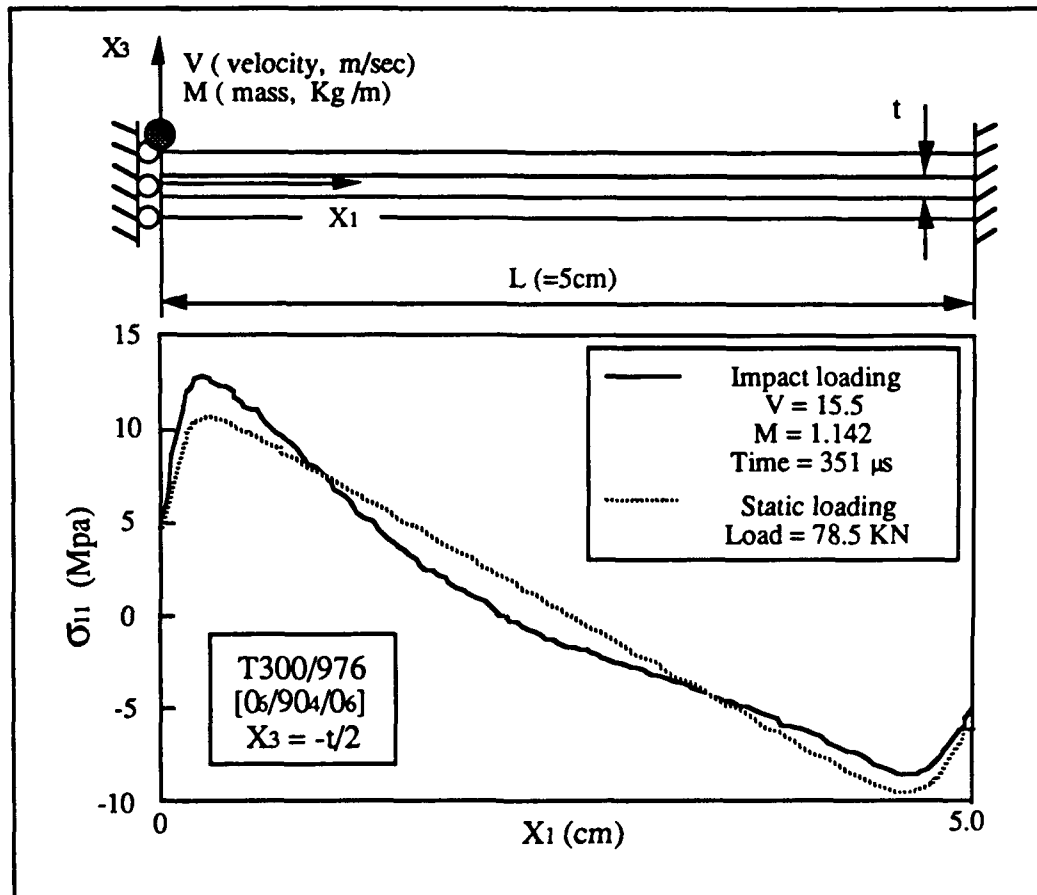


Figure 4.13: Comparison of the in-plane tensile stress distribution in the 90° layers along the lower $90/0$ interface of a $[0_6/90_4/0_6]$ composite specimen between the static and the transient dynamic calculations. The static load was applied to generate an equal amount of lateral deflection as that of the dynamic case at the compared instant.

Initial Matrix Crack Locations

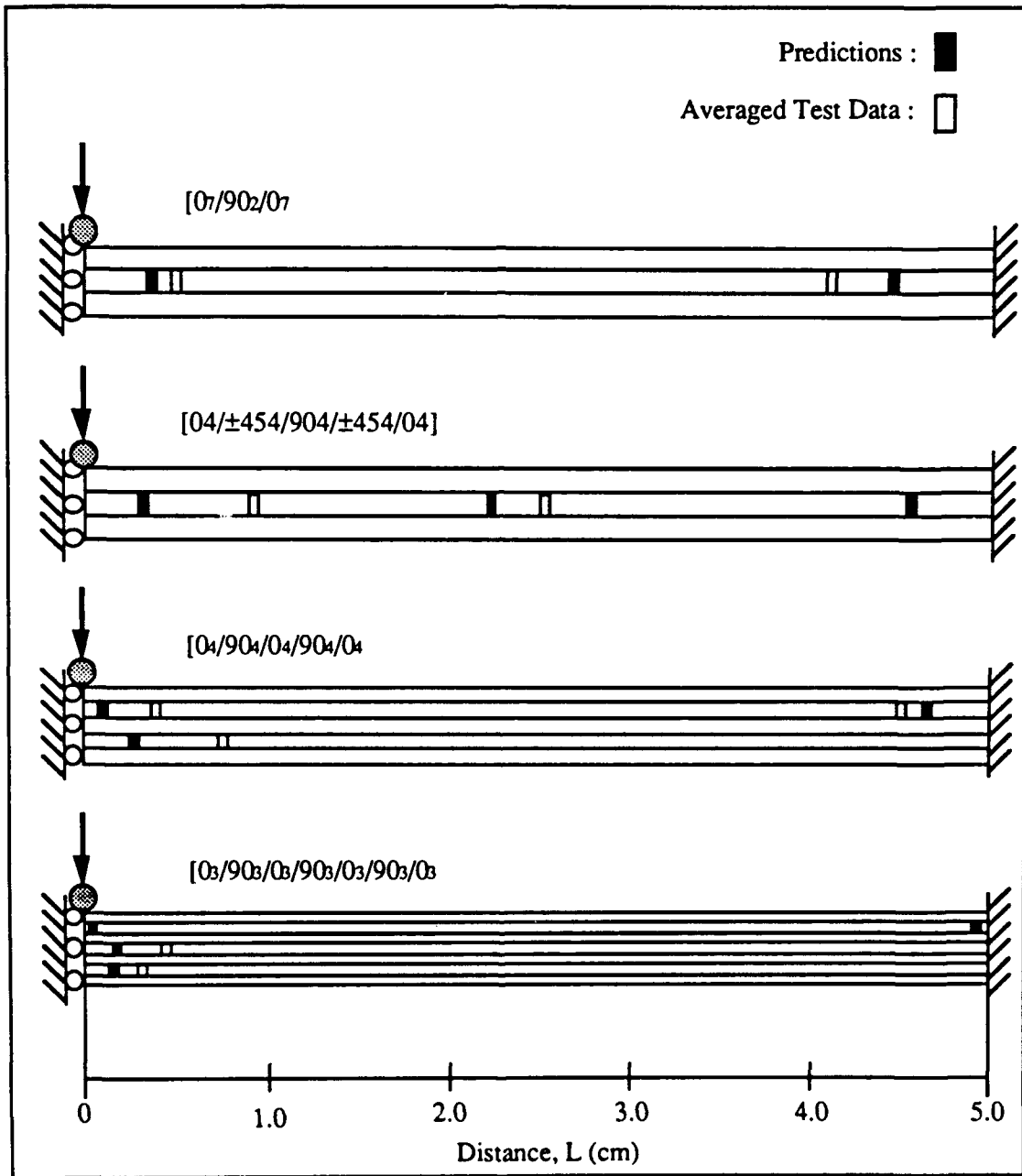


Figure 4.14: Comparison of the locations of the initial matrix cracks between the averaged data and the predictions.

critical matrix crack is dominated by the in-plane transverse tensile stress σ_{yy} , and hence, the crack surface was normal to the loading direction.

Therefore, based on the results of the calculations, it can be concluded that the critical matrix crack is the initial failure mode and the interlaminar shear stress/strength and in-plane transverse tensile stress/strength are very critical for initiating impact damage. The inclined cracks are dominated by the interlaminar shear stress, and the vertical cracks are governed by the transverse normal tensile stress.

4.5.2 Impact Energy Threshold

It is observed from the previous experiments (Chapter 3) that there exists an impact energy threshold beyond which impact damage occurs, but below which no damage can be found. The same phenomenon is also reported for point-loading impact by others [25,34,47]. It is strongly indicated from the previous experimental observation that the impact energy threshold is related to the energy required to cause the first critical matrix crack.

Thus, numerical calculations were performed to calculate the energy required to initiate the first critical matrix crack for all the test configurations. For a given mass of the impactor, the numerical simulation was performed at various velocities until the first critical matrix crack was predicted. The impact energy threshold is defined as one half of the mass multiplied by the square of the velocity corresponding to the initial matrix crack ($1/2MV^2$). The predicted impact energy thresholds for various ply orientations and thickness compared to the test data are presented in Table 4.2. Overall, the predictions agree with the test data very well. The predictions are, in general, consistently conservative compared to the experiments. The predictions further strongly confirm the experimental observation that the impact energy threshold is associated with the energy required to initiate the first critical matrix crack. Delamination will proceed once the critical matrix is produced.

Ply Orientation	Mass (kg/m)	Test Velocity (m/s)	Predicted Velocity (m/s)	Predicted Energy (J/m)
[0 ₇ /90 ₂ /0 ₇]	1.14	19±1.5	20	228
[0 ₆ /90 ₄ /0 ₆]	1.14	14±1	15.5	137
[0 ₄ /±45 ₄ /90 ₄ /±45 ₄ /0 ₄]	1.57	15±1	15	177
[0 ₃ /±45 ₄ /90 ₆ /±45 ₄ /0 ₃]	1.57	17±1	14	154
[0 ₄ /90 ₄ /0 ₄ /90 ₄ /0 ₄]	0.80	25±2	20	157
[0 ₃ /90 ₃ /0 ₃ /90 ₃ /0 ₃ /90 ₃ /0 ₃]	4.40	13±2	11	266

Table 4.2: Prediction of impact velocity threshold.

Apparently, by examining Table 4.2, it can be found that the impact energy threshold is also strongly affected by ply orientation and laminate thickness. Ply orientation (especially the stacking sequence) seems to have more effect on impact energy threshold than thickness. For instance, the impact energy threshold of [0₄/90₄/0₄/90₄/0₄] laminates is about 15 percent higher than that of [0₆/90₄/0₆] laminates with the laminate thickness increased by 25 percent, from 16 layers to 20 layers. However, comparing the energy thresholds between [0₃/90₃/0₃/90₃/0₃/90₃/0₃] and [0₄/90₄/0₄/90₄/0₄] laminates with only one layer difference in thickness, the energy threshold increased by 40 percent from [0₄/90₄/0₄/90₄/0₄] to [0₃/90₃/0₃/90₃/0₃/90₃/0₃]. Accordingly, ply orientation and thickness are also very important factors, especially the former, on the design of composite structures which may be subjected to impact.

4.5.3 Delamination and Micro-cracks

Once a critical matrix is predicted, the material stiffnesses within the element containing the crack are reduced according to the material degradation rules, and the stress distributions near the damaged element are recalculated. Figure 4.15 shows the redistributed out-of-plane normal stresses along the ply interfaces of a $[0_6/90_4/0_6]$ laminate before and after matrix cracking. Directly before the occurrence of the matrix crack, the out-of-plane normal stress is near zero around the damaged location. However, two peak out-of-plane normal stresses with opposite signs are found immediately adjacent to the damaged element along each upper and lower interface between the 0 and 90 degree layers. Furthermore, the distribution of interlaminar shear stress increases in the neighborhood of the damaged area and reduces sharply to zero within the damaged area, as shown in Figure 4.16.

Along the lower interface, the concentrated normal stress is positive leading away from the impacted area, and becomes negative toward the impacted area. However, along the upper interface, the situation of the stress distribution is completely reversed. This result indicates that two delaminations can be initiated by the out-of-plane normal tensile stresses along the upper and lower interfaces resulting from mode I fracture. The interlaminar shear stress near the damage area consequently can enhance the growth of the delamination once it propagates. The delamination along the lower interface propagates away from the impacted region, but the delamination along the upper interface moves toward the center of the specimen. The results from the prediction can be illustrated by the drawing shown in Figure 4.17. This prediction is very consistent with the experimental findings as shown in Figure 3.5, which is a side view of a lifesize photograph of a $[0_6/90_4/0_6]$ specimen after impact.

Similar results are also obtained for the distribution of in-plane transverse tensile stresses of a $[0_6/90_4/0_6]$ laminate before and after the occurrence of the critical matrix crack. The results of calculations are shown in Figure 4.18. Again, there appears to be two peak in-plane transverse stresses along the same upper and lower interfaces as the out-of-plane normal tensile stresses near the damaged area immediately after

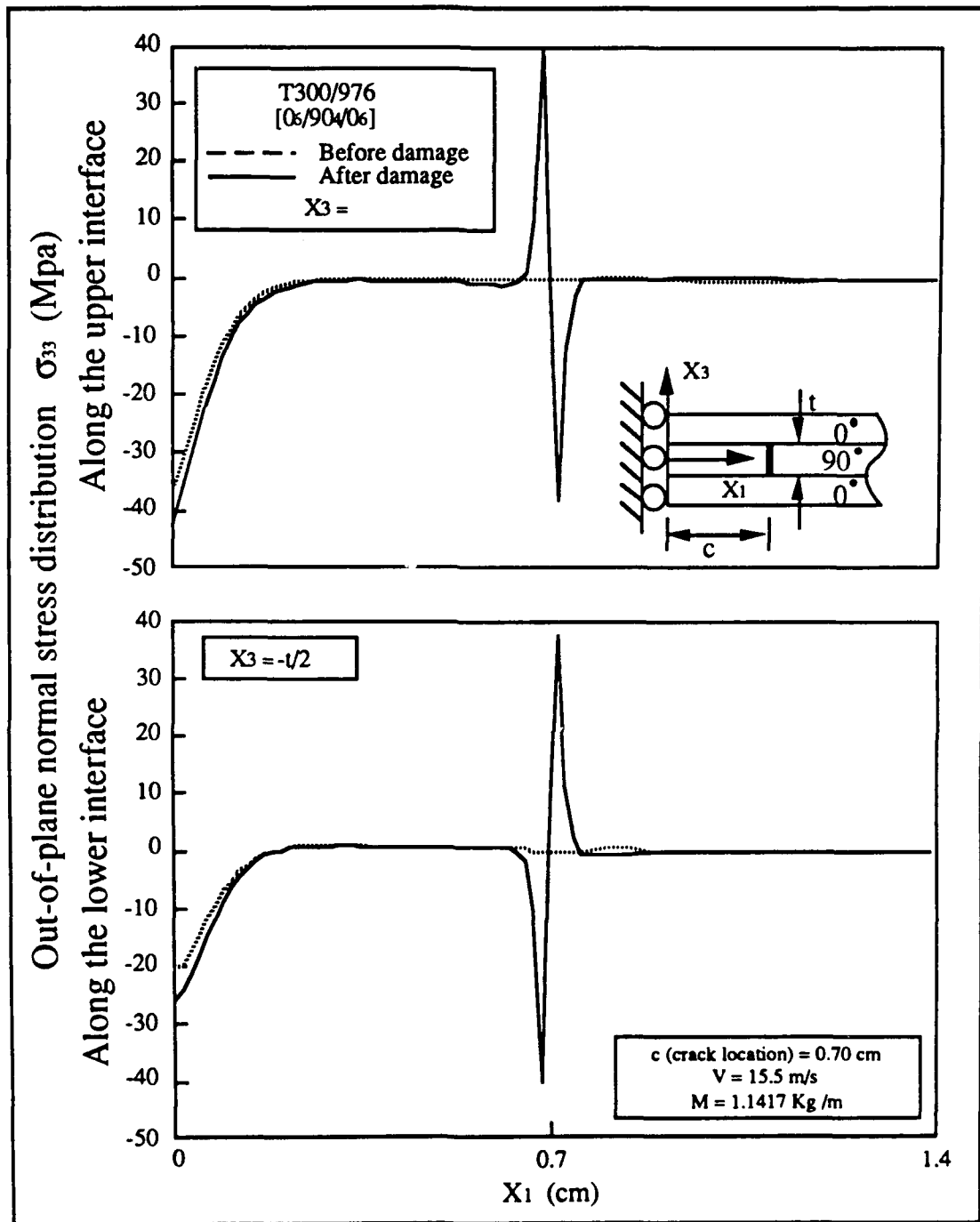


Figure 4.15: Comparison of the instantaneous out-of-plane normal stress distributions along the upper and lower 90° interfaces in the 90° plies of a $[0_6/90_4/0_6]$ specimen before and after impact.

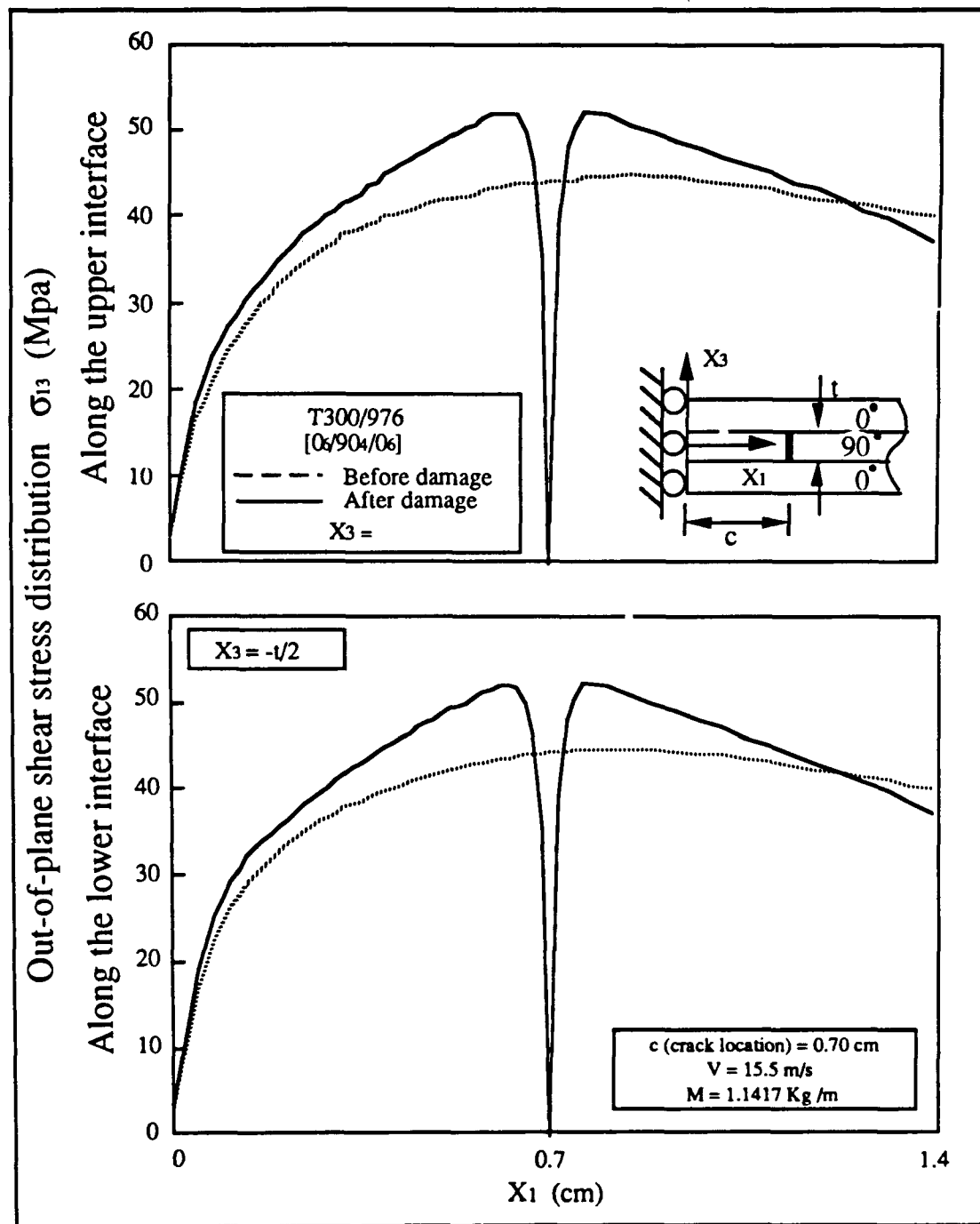


Figure 4.16: Comparison of the instantaneous interlaminar shear stress distributions along the upper and lower 90/0 interfaces in the 90° plies of a [0₆/90₄/0₆] specimen before and after impact.

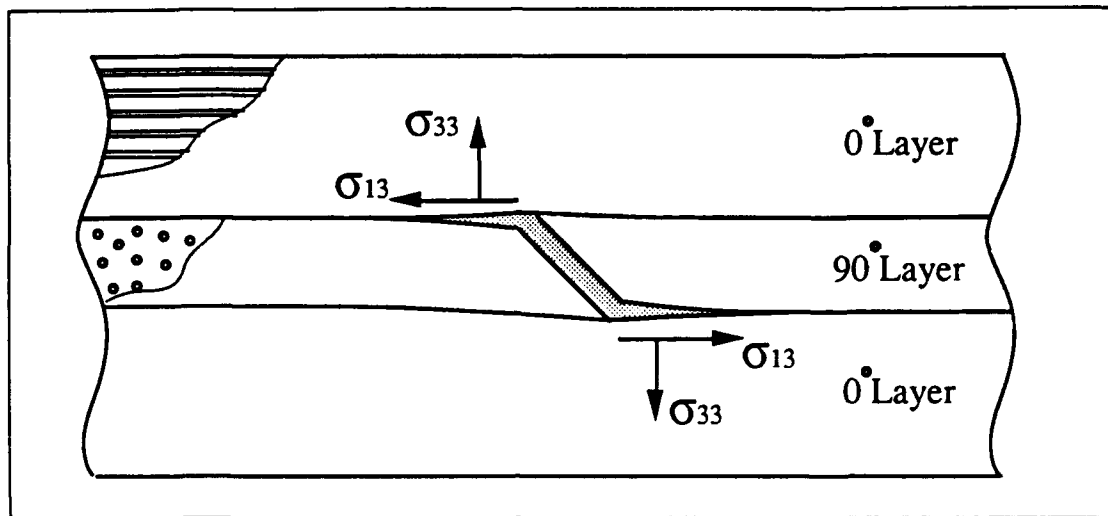


Figure 4.17: A schematic description of the impact damage mechanism resulting from an internal matrix crack.

matrix cracking. This can imply that the resulting highly concentrated in-plane normal tensile stress can cause micro-cracks in the 90 degree layers accompanying the delamination growth. These micro-cracks along with delaminations were detected by X-ray from the experiments. As a comparison, a typical sample of a radiograph of these micro-cracks of a $[0_6/90_4/0_6]$ specimen is shown in Figure 3.5. It is worth noting that the extent of the micro-cracks is quite consistent with the size of the delaminations.

Similar results for evaluating the initiation of delamination and micro-cracks are also obtained for $[90_3/0_3/90_3]$ specimens. The distributions of the out-of-plane normal stress and transverse tensile stress before and after the occurrence of the critical matrix crack at the center of the specimen along the 90 and 0 degree ply interface are presented in Figure 4.19. Again, stress concentrations arise near the crack tip along the interface and trigger the initiation of delamination and micro-cracks. Accordingly, based on the predictions and the experimental observations from the previous chapter, the physical processes of impact damage mechanisms in laminated composites due to low velocity impact can be illustrated schematically in sequential steps as shown in

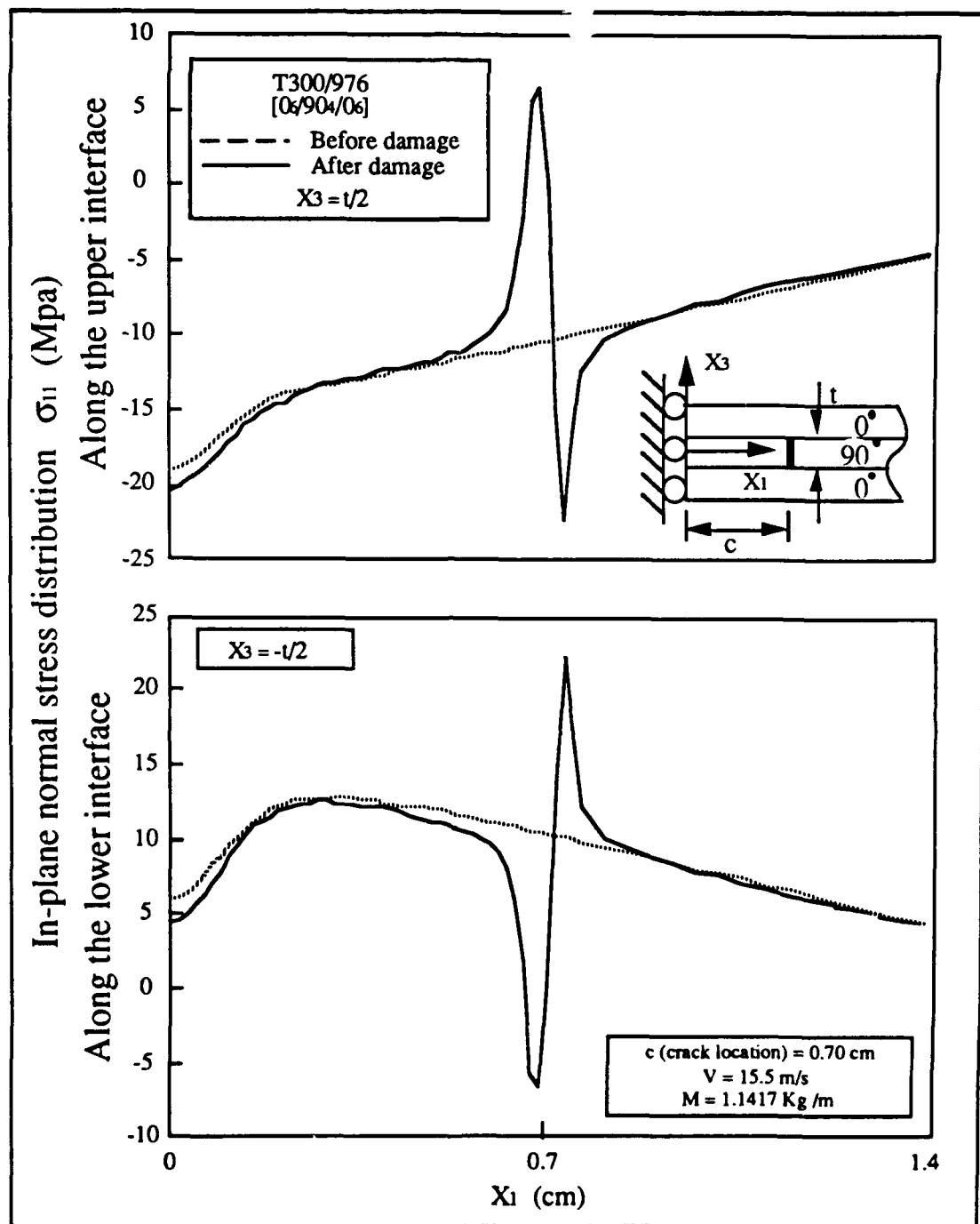


Figure 4.18: Comparison of the instantaneous in-plane transverse normal stress distributions along the upper and lower 90/0 interfaces in the 90° plies of a $[0_6/90_4/0_6]$ specimen before and after impact.

Figure 4.20.

4.6 CONCLUSION

An analytical investigation was performed to study impact damage in laminated composites as a result of line-loading impact. An analysis was developed for predicting the impact damage and for understanding impact damage mechanisms and mechanics of laminated composites. The results of the predictions agreed very well with the experiments. Based on the study, the following remarks can be made:

1. Matrix cracking is the initial failure mode of impact damage of laminated composites.
2. Delamination and micro-cracks due to impact are initiated by the matrix cracks (the critical matrix cracks).
3. Impact energy threshold is associated with the energy required to initiate the first critical matrix crack.
4. Pre-existing micro-cracks can significantly reduce the impact resistance of composites.
5. Interlaminar shear stresses/strength and in-plane tensile stress/strength are the dominant factors causing the critical matrix cracks.
6. Out-of-plane normal stress (or Mode I) and interlaminar shear stress (or Mode II) are important for determination of delamination growth after the critical matrix is introduced.
7. In-plane transverse tensile stress and interlaminar shear stress near the critical matrix cracks produce micro-cracks as delamination propagates.

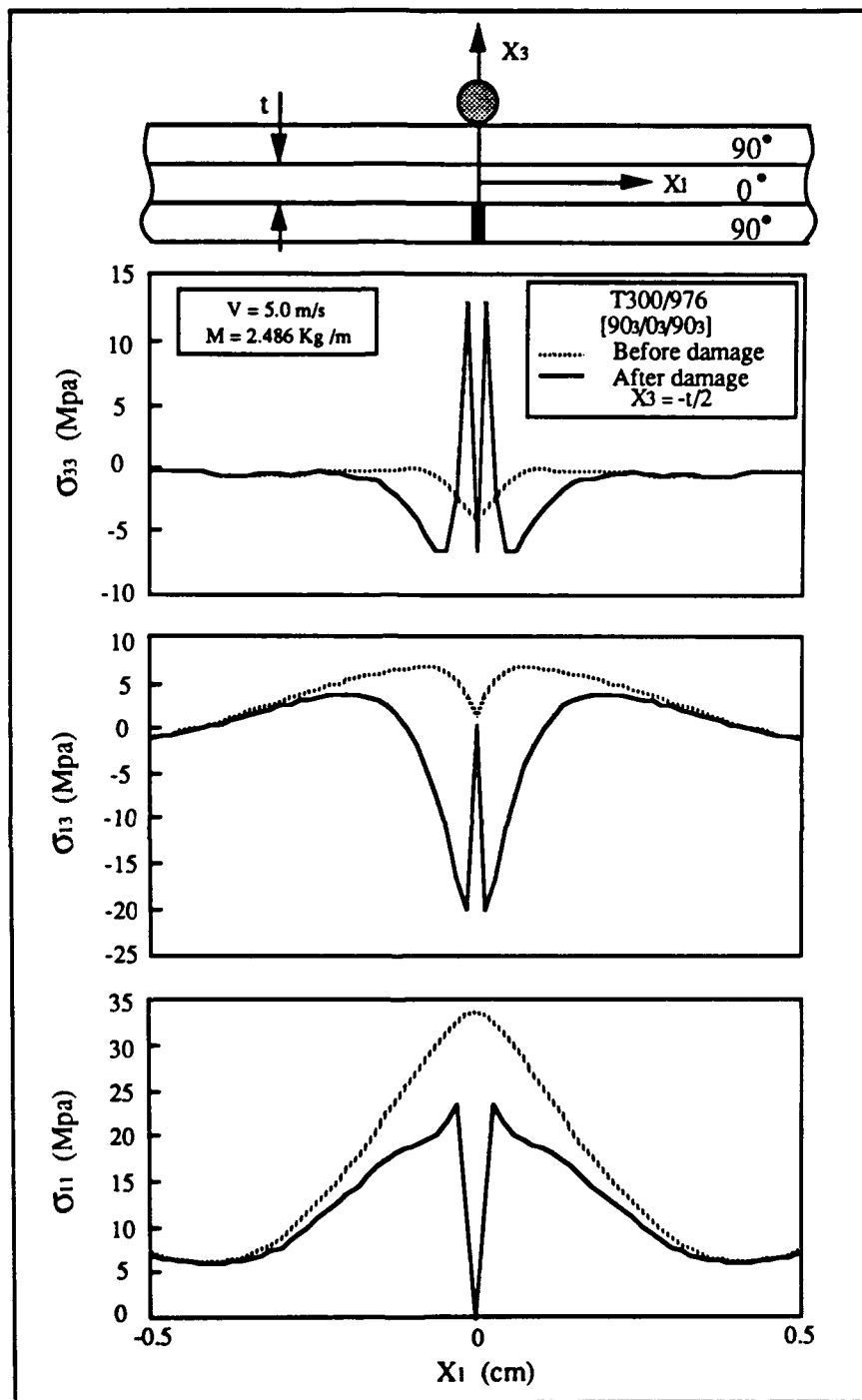


Figure 4.19: Comparison of the instantaneous out-of-plane, interlaminar shear stress, and in-plane normal stress distributions along the lower 0/90 interfaces in the 90° plies of a [90₃/0₃/90₃] specimen before and after impact.

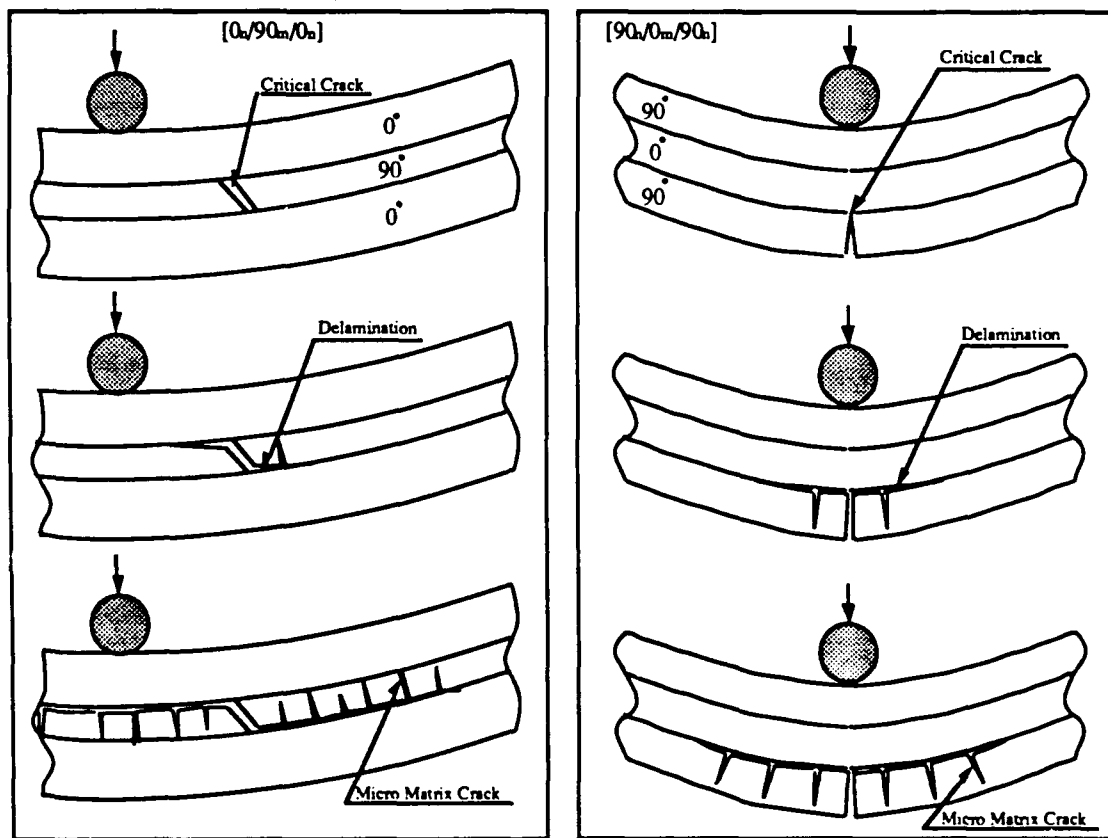


Figure 4.20: A schematic description of two basic impact damage growth mechanisms of laminated composites.

Chapter 5

EFFECTS OF IMPACT PARAMETERS

5.1 INTRODUCTION

The effects of laminate configurations, such as stacking sequence and thickness, and mass of the impactor on the impact damage of laminated composites due to low-velocity line load impact were also studied. The major focus of the study concentrated on the initial damage and the corresponding failure mode. Hence, it was of particular interest to determine the velocity of the impactor required to initiate the impact damage as a function of the stacking sequence and the thickness of the composites for different impactors' masses. In order to understand the basic mechanics and mechanisms of the test results, numerical simulations based on an analytical model (Chapter 4) were also performed. Based on the study, the relationships of the initial damage with respect to the laminate configuration and impactor's mass were established.

5.2 EXPERIMENTS

In order to achieve the objectives, laminates made of T300/976 Graphite/Epoxy prepregs with different stacking sequences and thicknesses were deliberately selected for the tests. For stacking sequence effect, cross-ply composites, containing about 67 percent of 0 degree plies and 33 percent of 90 degree plies, with four different stacking

Ply Orientation	Thickness (h) (mm)	Span length (L) (cm)	Width (W) (cm)	Impactor Mass (kg/m)		
[0 ₆ /90 ₆ /0 ₆]	2.58	10.0	2.3		4.17	6.67
[0 ₄ /90 ₃ /0 ₄ /90 ₃ /0 ₄]	2.58	10.0	2.3	2.50	4.17	6.67
[0 ₃ /90 ₂ /0 ₃ /90 ₂ /0 ₃ /90 ₂ /0 ₃]	2.58	10.0	2.3	2.50	4.17	6.67
[0 ₂ /90/0 ₂ /90/0/90/0] _s	2.58	10.0	2.3		4.17	
[(0 ₃ /90 ₃) _n /0 ₃]	2.16	10.0	2.3	2.50	4.17	6.67
[(0 ₃ /90 ₃) _n /0 ₃]	3.02	10.0	2.3	2.50	4.17	6.67
[(0 ₃ /90 ₃) _n /0 ₃]	3.88	10.0	2.3	2.50	4.17	6.67

Table 5.1: Ply orientations and geometries of the test specimens.

sequences were selected: [0₆/90₆/0₆], [0₄/90₃/0₄/90₃/0₄], [0₃/90₂/0₃/90₂/0₃/90₂/0₃] and [0₂/90/0₂/90/0/90/0]_s, all of which have a constant thickness. To evaluate the thickness effect, the [(0₃/90₃)_n/0₃] composites were chosen. The subscript *n* indicates the number of the repeat of (0₃/90₃) in the laminate. Three different thicknesses were considered. In addition, three different masses were used for each selected configuration. Table 5.1 lists the stacking sequences, geometries, and masses of the impactors used in the experiments.

All the specimens were cured under the same cure cycle used in Chapter 3 (see Figure 3.3) and were cut into the same size: 10.1 cm in length and 2.54 cm in width. An X-radiograph was taken of all the specimens before impact to examine the internal damage resulting from manufacturing or cutting. No apparent damage was found in any of the specimens.

Each specimen was firmly clamped on two parallel edges, and the other edges were left free, as shown in Figure 5.1. A specially designed L-shaped aluminum tab was adhesively bonded to each clamped end of the specimen to prevent any slippage of the specimen from the fixture during impact. A schematic of the test configuration of the specimen is shown in Figure 5.1. More than fifty specimens were tested. For each

configuration, four to five replicants were tested. After every test, each specimen was unloaded from the fixture and thoroughly inspected by a binocular microscope with 20 times of magnification to determine any damage from the sides of the specimen.

Initially, X-radiographs were also frequently taken to confirm the eye inspection. After many comparisons, it was found that the initial damage was so obviously noticeable by the naked eye that a dual confirmation by X-radiograph was unnecessary. Therefore, the X-radiograph was only used afterward when the damage inspected by the binocular microscope was in question. The undamaged specimens were reloaded and tested at a higher velocity, and then inspected again for initial damage. The procedure was repeated until initial damage was detected. Most specimens were repeatedly tested less than three times. It is noted that the attention of the experiment is focused on examining the initial damage, the mode of failure, and determining the corresponding impactor's energy or velocity required to cause such damage in composites.

5.3 RESULTS AND DISCUSSIONS

The results of the measured impact damage as a function of the energy of the impactor at the instant of impact for various specimen configurations are summarized in Figure 5.2. Each box in the figure represents a test configuration. The test data clearly shows that an impact energy threshold exists for all the composites tested, beyond which significant damage occurs, but below which no damage, including delaminations and microcracks, is found. The impact energy threshold is apparently the minimum energy required for causing impact damage. It has been illustrated that the initial impact damage consisted of several critical matrix cracks from which the subsequent damage, delamination and microcracks, is induced. Thus, the impact energy threshold corresponds to the energy that produces the critical matrix cracks.

Accordingly, the initial impact damage and the corresponding impact energy are very important for characterizing impact resistance of laminated composites, because

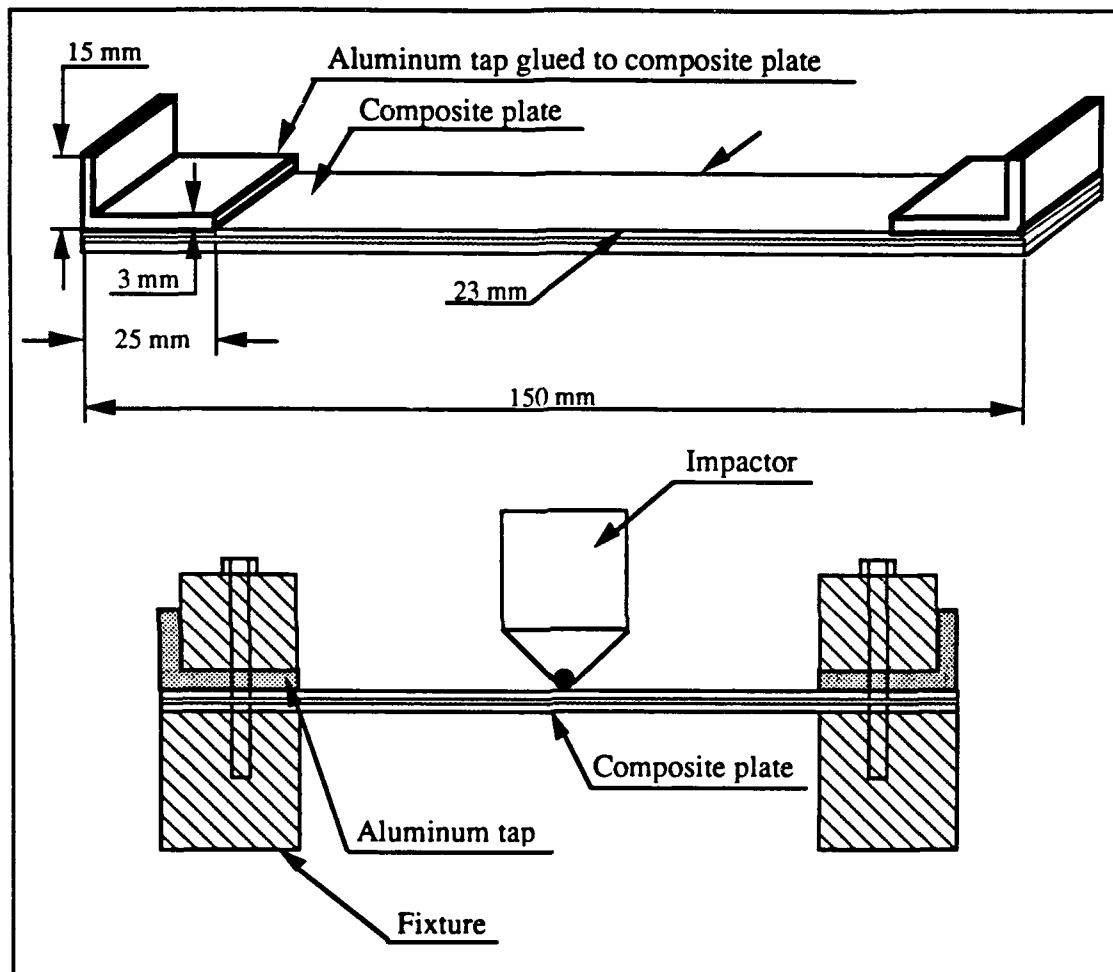


Figure 5.1: Description of the geometry and the boundary conditions of the test specimens.

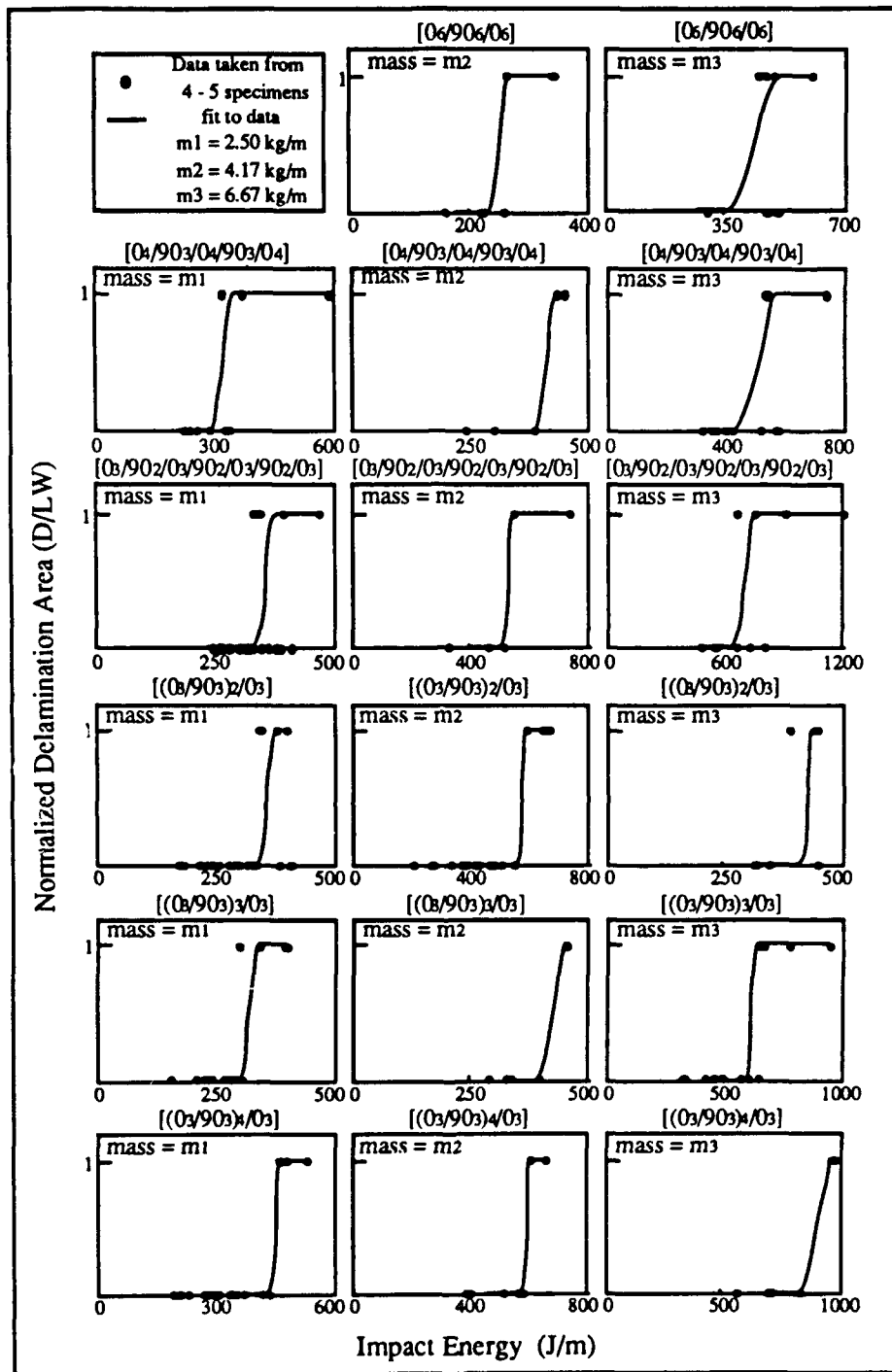


Figure 5.2: A summary of the test results. The measured impact damage size as a function of the impact energy for various specimen configurations.

they can lead to extensive damage in composites. Therefore, the initial impact damage and the energy threshold are evaluated and analyzed thoroughly in the following.

5.3.1 Stacking Sequence Effect

The test results of cross-ply laminated composites, consisting of three different stacking sequences, with a constant thickness and volume fraction of 0 degree and 90 degree plies are presented in Figure 5.3. Three different masses of the impactors are considered. The results presented in each box of the figure correspond to a different mass. In each box, the ordinate is the impact velocity threshold corresponding to the velocity of the impactor of a given mass required to cause initial damage. The horizontal axis indicates the three ply orientations. At a given mass, the test results clearly show that the stacking sequence significantly affects the impact velocity as well as the impact energy required to initiate the impact damage. The impact velocity threshold V_c can be enhanced by as much as 30 to 50 percent by reordering the sequence of the plies within the laminates from $[0_6/90_6/0_6]$ to $[0_3/90_2/0_3/90_2/0_3/90_2/0_3]$, depending upon the impactor's mass. It is worth noting that if the impact energy ($1/2MV_c^2$) is used instead of the velocity V_c in the ordinate, the difference in the impact energy threshold among these laminates is greatly magnified.

Apparently, the velocity (energy) of an impactor must be increased in order to produce initial impact damage as the number of layers grouped together with the same ply orientation within a laminate decreases. In other words, it is expected that the more uniformly dispersed the ply sequence is in a laminate, the higher the initial impact damage resistance will be. However, this statement is valid only under the condition that the initial damage is governed by critical matrix cracks, because sharp nose impactors with a higher impact velocity could easily cause surface damage such as fiber breakage on the surface of the laminates containing thin ply groups on outer surfaces. For example, a few tests were performed on $[0_2/90/0_2/90/0/90/0]$, composites, and a photograph of a life-size tested specimen is shown in Figure 5.4. The specimen, which has the same thickness as $[0_3/90_2/0_3/90_2/0_3/90_2/0_3]$ composites,

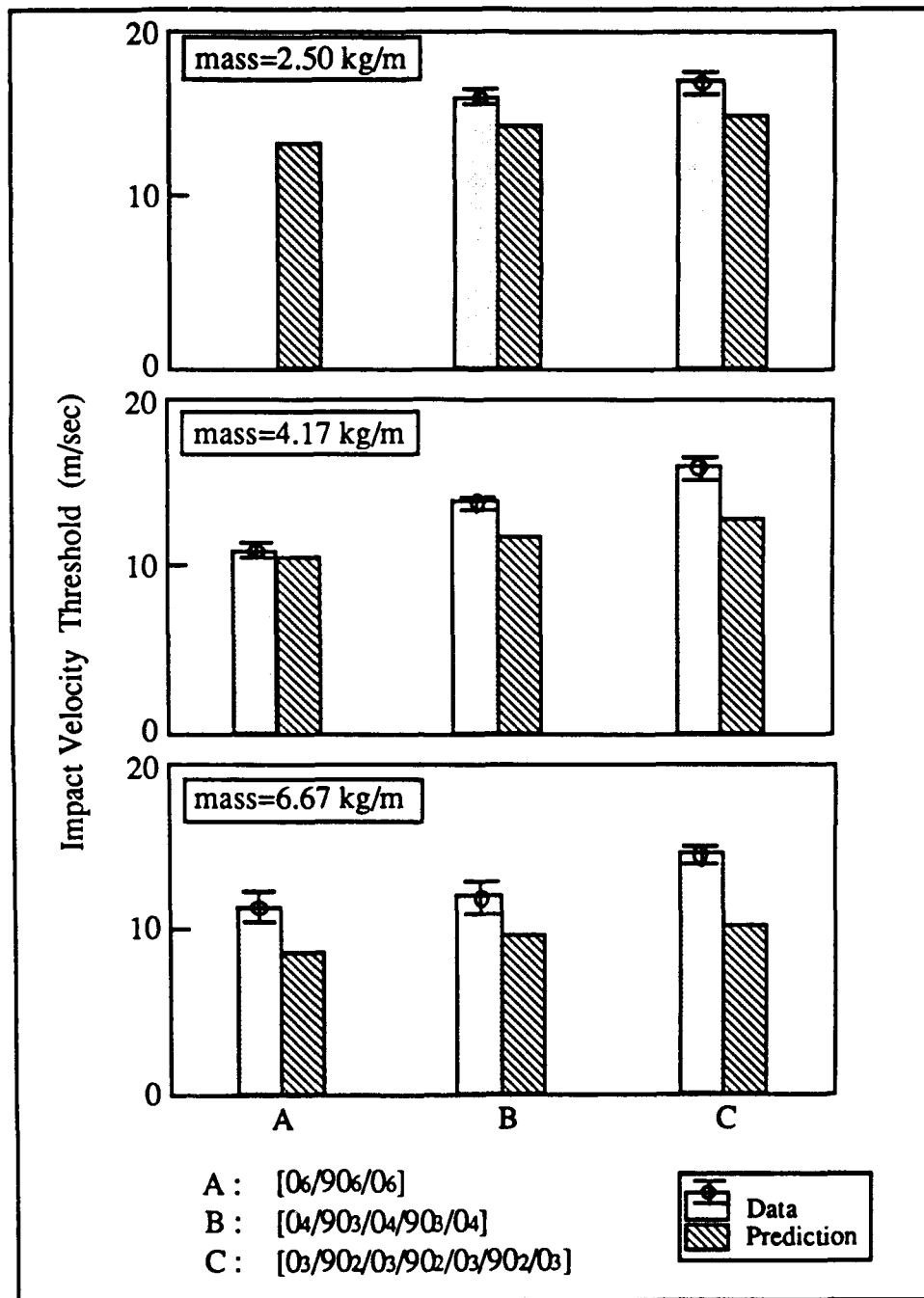


Figure 5.3: The effect of stacking sequence on the impact velocity threshold. Comparison between the test data and the predictions.

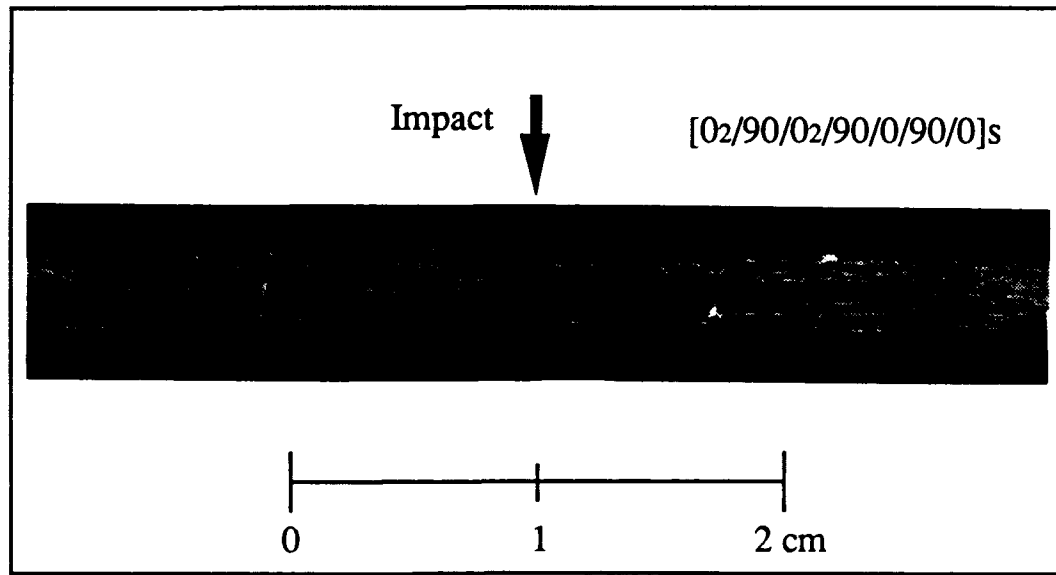


Figure 5.4: A photograph of a life-size $[0_2/90/0_2/90/0/90/0]_s$ specimen subjected to line-loading impact.

broke into two pieces when impacted. Surface damage due to fiber breakage is believed to have been the initial damage that triggered the total failure. The impact velocity threshold of the specimen was 16 m/sec at an impactor mass of 4.17 kg/m, which was nearly the same as that of the $[0_3/90_2/0_3/90_2/0_3/90_2/0_3]$ composites. Apparently, if the thickness of the surface ply group of composites is too thin (i.e., less than three plies), surface damage could occur earlier than internal damage, thus resulting in premature failure. Since the surface damage caused by fiber breakage was not the focus of the study, the results of the $[0_2/90/0_2/90/0/90/0]_s$ composites were not used further in comparisons with others which failed in totally different modes.

In order to fundamentally understand the phenomena of the test results, numerical simulations of the test conditions were performed based on the model (Chapter 4). The predicted impact velocity thresholds for the tested composites with the three different stacking sequences are presented in Figure 5.3. As can be seen, the predictions correlated with the data very well, especially for the lower masses. The discrepancy between the predictions and the data increased as the mass of the impactor increased.

This can be primarily attributed to the basic assumption of the analysis which was based on a small deformation theory. It was observed during the experiments that the amount of the out-of-plane deflection of the specimens increased substantially as the mass of the impactor increased. However, the predicted velocities overall were conservative and consistently lower than the test data by within 25 percent.

The predicted locations of the initial critical matrix cracks for these specimens are shown in Figure 5.5 as compared to the test data. A photograph of a typical life-size tested specimen corresponding to each stacking sequence appears in Figure 5.6. It is worth noting that the locations of the critical matrix cracks shift from the mid-plane in $[0_6/90_6/0_6]$ composites toward the back surface of the specimens (away from the impacting surface) in $[0_3/90_2/0_3/90_2/0_3/90_2/0_3]$ composites, as the six 90 degree plies located at the mid-plane of the laminates are dispersed throughout the laminates. For $[0_6/90_6/0_6]$ composites, the critical cracks, inclined at an angle of nearly 45 degrees, are located in the 90 degree central plies. However, for $[0_4/90_4/0_2/90_4/0_4]$ and $[0_3/90_2/0_3/90_2/0_3/90_2/0_3]$ composites, the critical cracks are found in the 90 degree ply group near the back side of the specimens, and the direction of the surface of the cracks lean more and more toward the direction vertical to the loading direction (about 90 degrees measured from the center line).

It has been demonstrated in Chapter 4 that both interlaminar shear stress σ_{yz} and transverse tensile stress σ_{yy} control the initial impact damage mechanism due to line-loading impact. Excessive interlaminar shear stress can cause inclined cracks, and the high in-plane transverse tensile stress can result in vertical cracks. For transverse impact, the interlaminar stress distributions across the thickness reach a maximum near the mid-plane of the laminate, but the transverse tensile stress is minimal near the central plane and increases toward the outer surfaces due to bending. According to Eq. (4.45), the combined ratios of the interlaminar shear stress to shear strength and transverse tensile stress to tensile strength determine the velocity threshold of the laminate and the locations of the critical cracks.

Initial Matrix Crack Locations

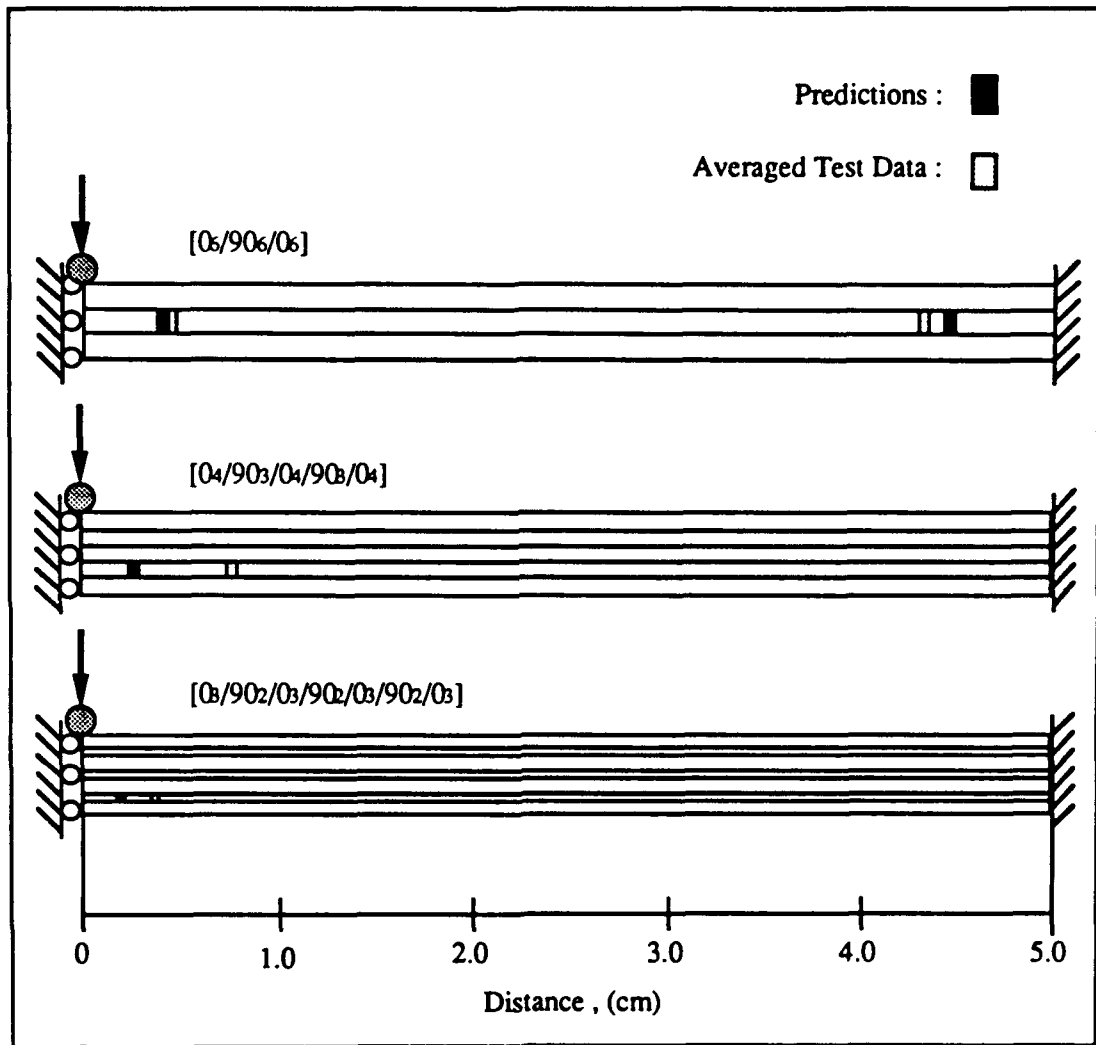


Figure 5.5: The effect of stacking sequence on the location of the initial matrix crack. Comparison between the test data and the predictions.

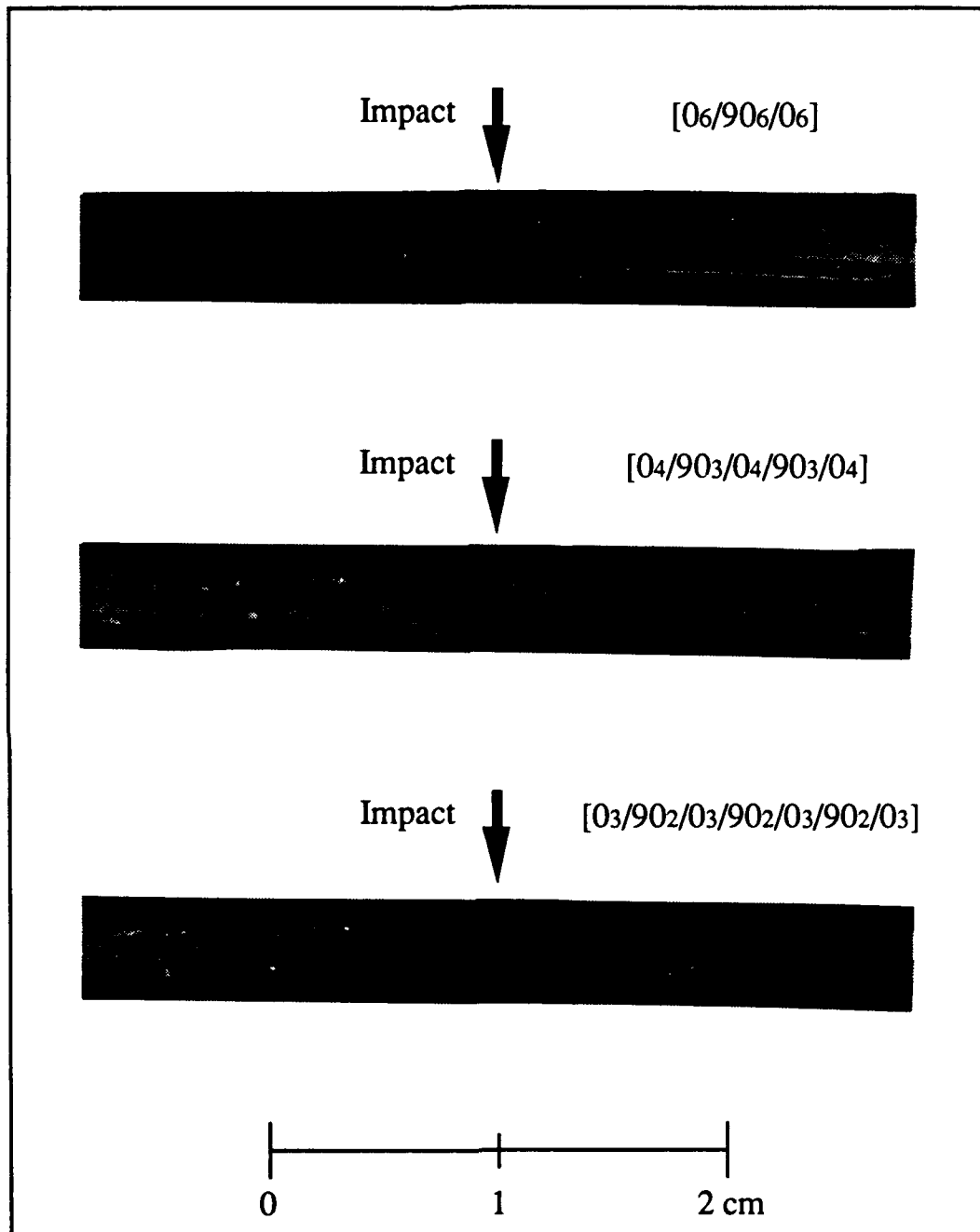


Figure 5.6: Photographs of three typical life-size tested specimens corresponding to three different stacking sequences.

Figure 5.7 compares the calculated stress/strength ratio of each stress component corresponding to the impact velocity threshold for the laminates with the three different stacking sequences. Note that the sum of the two ratios for each laminate is equal to unity. For $[0_6/90_6/0_6]$ composites, initial failure is dominated primarily by the interlaminar shear stress/strength ratio. As a result, the critical cracks are inclined by nearly 45 degrees in the 90 degree layers. However, the interlaminar shear stress/strength ratio is reduced for the $[0_4/90_3/0_4/90_3/0_4]$ composites because the 90 degree ply group, where the cracks are generated, is away from the mid-plane. Hence, failure is due to the combination of interlaminar shear stress and transverse tensile stress. The cracks are less inclined than those of the $[0_6/90_6/0_6]$ composites. As the 90 degree plies are further dispersed throughout the laminates in $[0_3/90_2/0_3/90_2/0_3/90_2/0_3]$ composites, the locations of the critical cracks are closer to the back of the outer surface. Accordingly, the transverse tensile stress/strength ratio further increases and become a dominant factor for the damage in $[0_3/90_2/0_3/90_2/0_3/90_2/0_3]$ composites. Based on the calculations, it is apparent that both interlaminar shear stress and transverse tensile stress are critically important for causing initial impact damage in laminated composites. By reordering the stacking sequence, the effect of the combined stresses on the location of the initial failure can be changed significantly. A higher impact resistance can be expected for laminates whose initial failure occurs away from the mid-plane, because a higher velocity is required to make up the reduction of the interlaminar shear stress near the outer surfaces.

5.3.2 Thickness Effect

The effect of laminate thickness on the initial impact damage is demonstrated by the results of the test data on $[(0_3/90_3)_n/0_3]$ composites ($n = 2$ thru 4), as shown in Figure 5.8. As n increased, the repeating ply group of $(0_3/90_3)$ duplicate n times within the laminate; only the thickness is changed, and the ply orientation and stacking sequence remain the same. Again, each box in the figure presents the data obtained from a particular mass of the impactor. By comparing the test data for various laminate

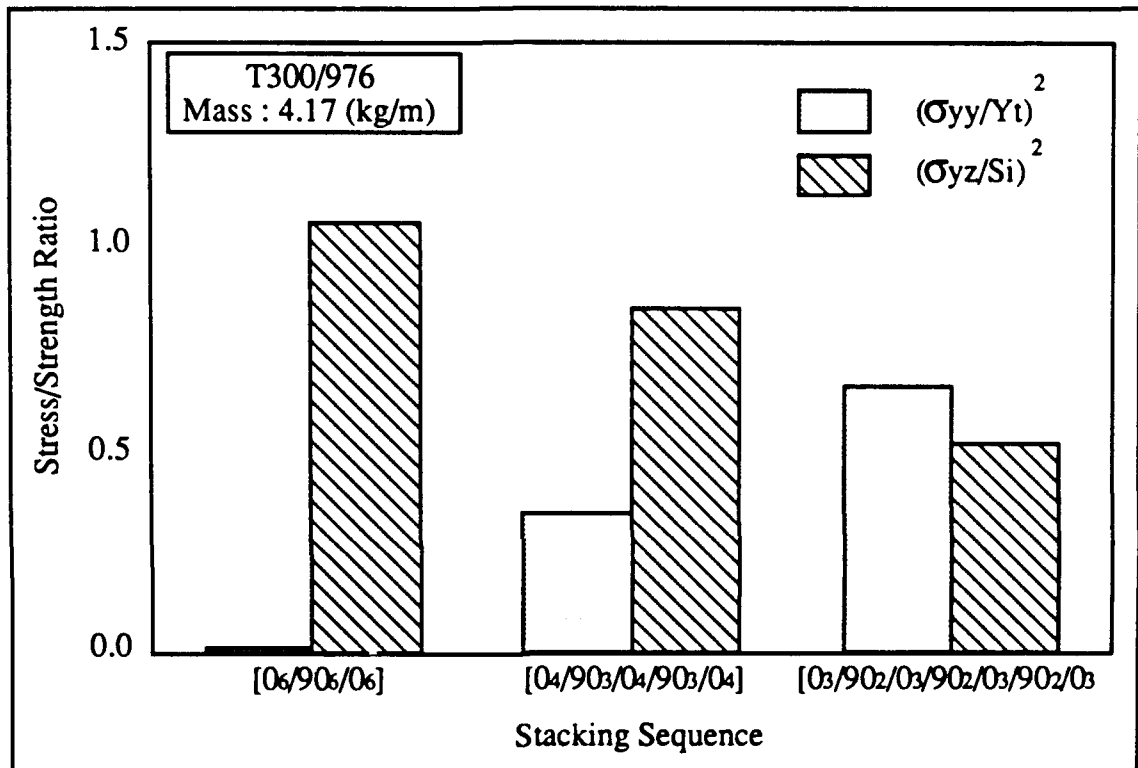


Figure 5.7: The calculated on-set interlaminar shear stress/strength and transverse tensile stress/strength ratios corresponding to the impact velocity thresholds for laminates with three different stacking sequences.

thicknesses, it is clear that the change of laminate thickness does not significantly alter the impact velocity threshold. The effect of thickness is not as clear and obvious as the stacking sequence on the initial impact damage of composites. For lower masses ($M = 2.5$ kg/m and 4.17 kg/m), the impact velocity threshold varies within ± 10 percent as the laminate thickness increases from 15 layers to 27 layers. A consistently moderate increase of the impact velocity threshold is found for the laminates impacted under the heaviest mass ($M = 6.67$ kg/m).

The predictions of the impact velocity thresholds for the laminates with various thicknesses based on the analytical model are also presented in Figure 5.8. Again, the predicted impact velocity thresholds are conservative and consistently lower than the test data. The difference between the predictions and the test data becomes significant especially for the thin laminates $[0_3/90_3/0_3/90_3/0_3]$ with 15 layers and for the laminates impacted under the heaviest mass ($M = 6.67$ kg/m). This also can be primarily attributed to the large out-of-plane deformations occurring during impact which can not be adequately analyzed by the model based on the present small deformation theory. It is believed that a better prediction can be obtained by adopting the large deformation theory in the model.

The predictions indicate that the impact velocity threshold is expected to increase slightly as the thickness of the composites increases. However, the rate of increase of the impact velocity threshold with thickness is considerably smaller than that with stacking sequence. Accordingly, the initial impact damage and the subsequent growth of damage in composites are much more sensitive to the change of stacking sequence than to the change in thickness.

The predicted locations of the critical matrix cracks for these laminates are presented in Figure 5.9 along with the measured test data. A photograph of a life-size specimen corresponding to each configuration is shown in Figure 5.10. Apparently, the predictions correlate with the test data very well. Figure 5.11 shows the stress/strength ratio of interlaminar shear and transverse tensile stresses in the 90 degree layers where the critical matrix cracks are predicted for the laminates with

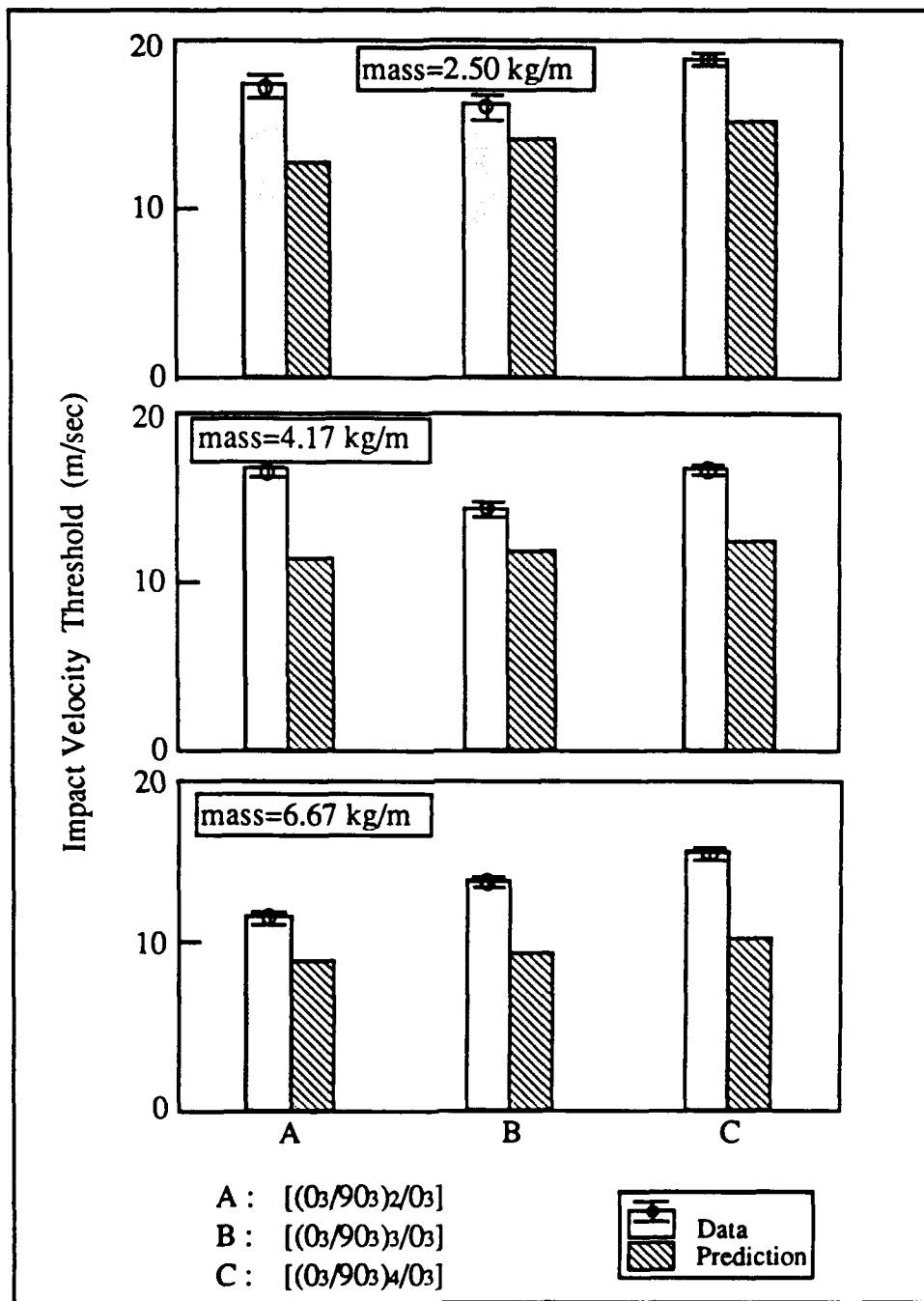


Figure 5.8: The effect of laminate thickness on impact velocity threshold. Comparison between the test data and the predictions.

three different thicknesses. It seems that interlaminar shear stress is more important than the transverse tensile stress on producing the initial damage for thin laminates, but the trend is gradually reversed when the thickness increases. For $[(0_3/90_3)_4/0_3]$ composites, the contribution of the transverse tensile stress to damage is greater than that of the interlaminar shear stress. However, the difference between the two ratios for each of these three composites is relatively small compared to that for the composites with various stacking sequences. Accordingly, this is the reason why the impact damage is much less sensitive to laminate thickness than to stacking sequence. It is expected that, if the initial impact damage is dominated by the transverse tensile stress, increasing the thickness could increase the impact resistance of the composites. However, if the failure mode of the composites is strongly associated with the interlaminar shear stress, then the effect of thickness on impact damage is expected to be at a minimum.

5.3.3 Mass Effect

The effect of the mass of the impactor on the initial impact damage can be best demonstrated in Figures 5.12 and 5.13 by reorganizing the test data. The ordinate of each box in the figures is the impact velocity threshold, and the horizontal axis is the impactor's mass. Both test data and the predictions are shown in the figures. Clearly, the impact velocity threshold strongly depends upon the impactor's mass; the heavier the mass is, the lower impact velocity is required to cause damage. Thus, the impact velocity threshold increases if the mass of the impactor decreases. However, it is found from all the composites tested that the percentage of increase of the impact velocity threshold to the percentage of decrease of the impactor's mass is out of proportion; a nonlinear relationship exists between the impact velocity threshold and the impactor's mass for a given laminate configuration. Overall, an increase of the mass by three times approximately reduces the impact velocity threshold by as much as 50 percent.

The finding of the test results from Figures 5.12 and 5.13 is very important and significant. It indicates that the mass of the impactor should be considered as a factor

Initial Matrix Crack Locations

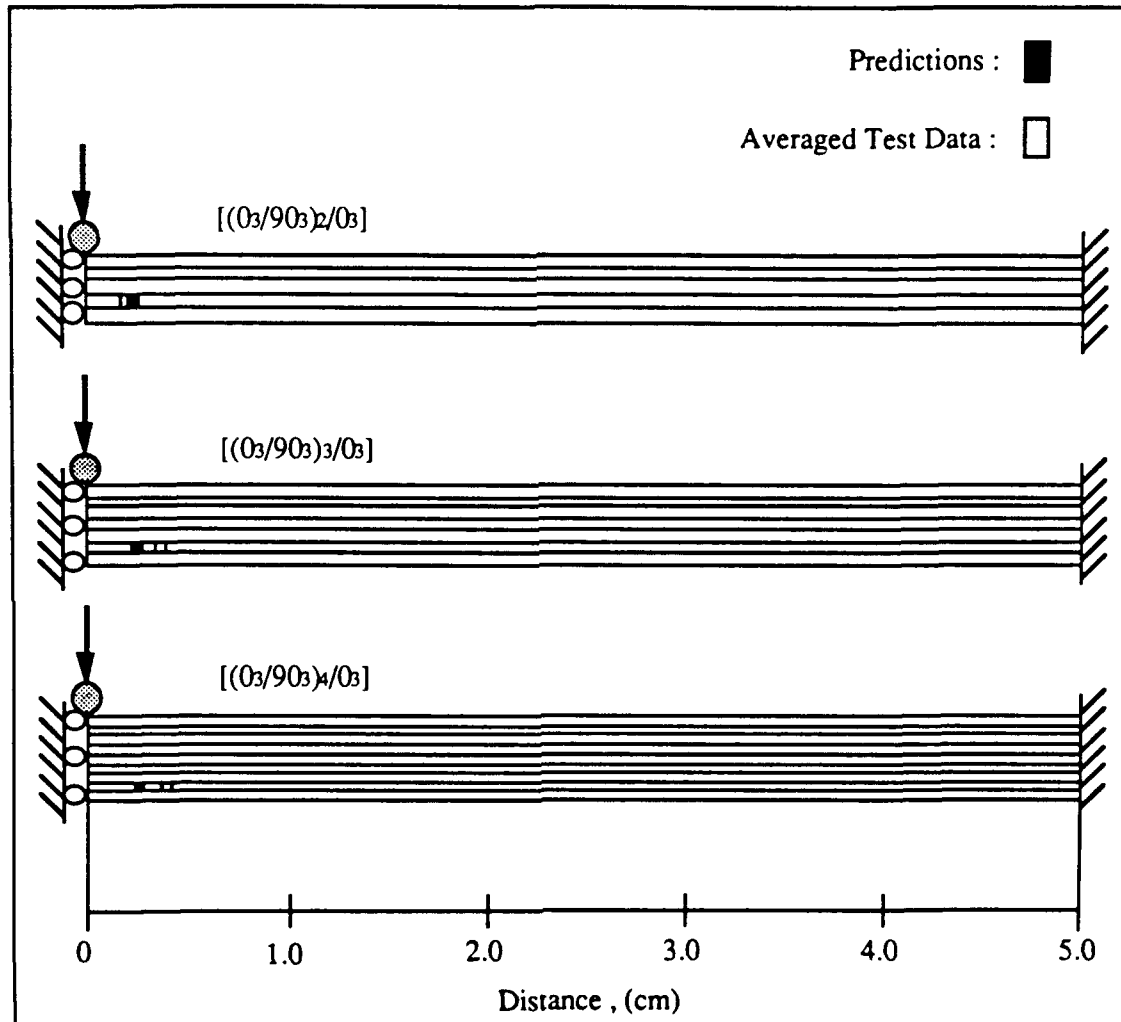


Figure 5.9: The effect of laminate thickness on the location of the critical matrix crack. Comparison between the test data and the predictions.

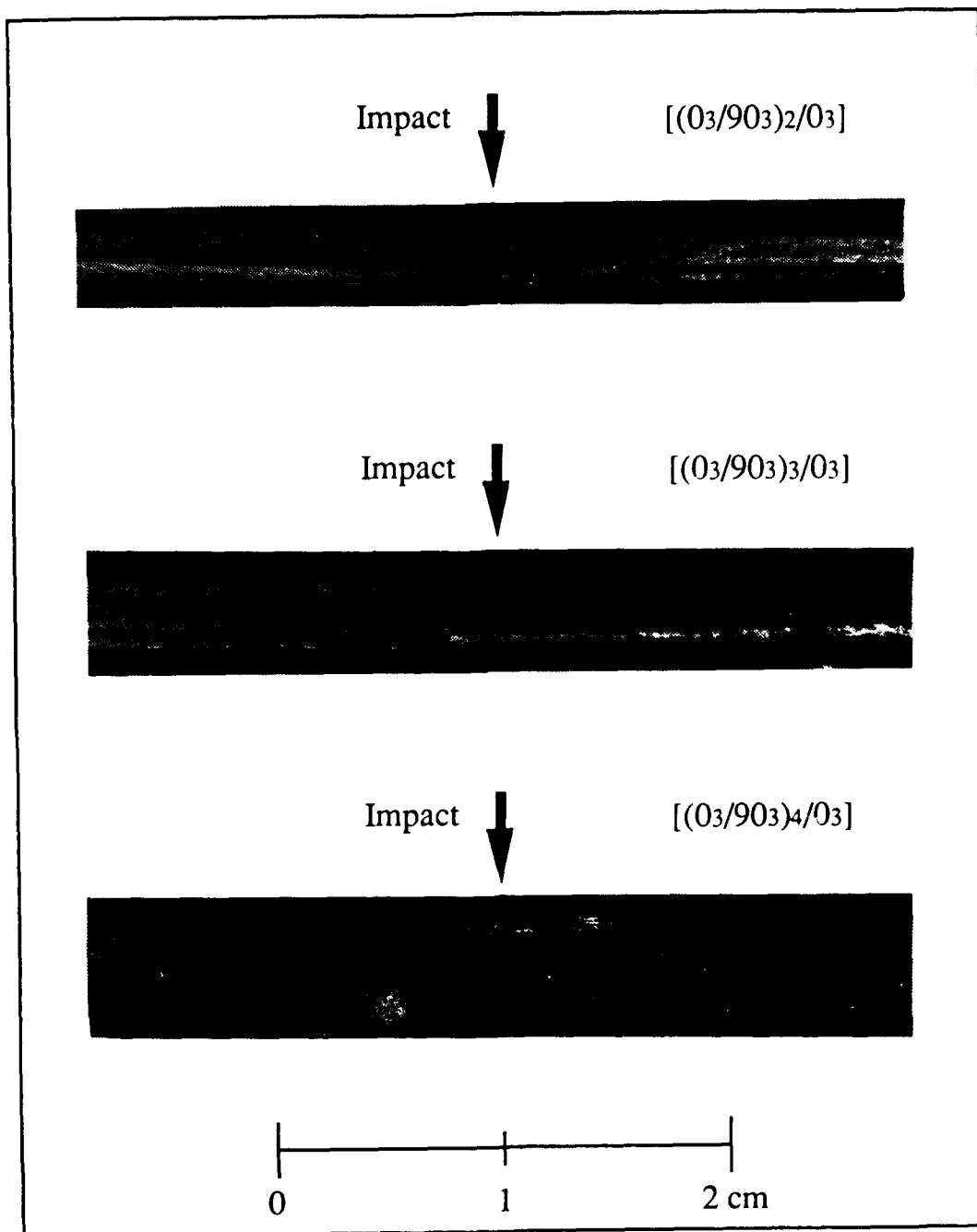


Figure 5.10: Photographs of three typical life-size tested specimens corresponding to three different laminate thicknesses.

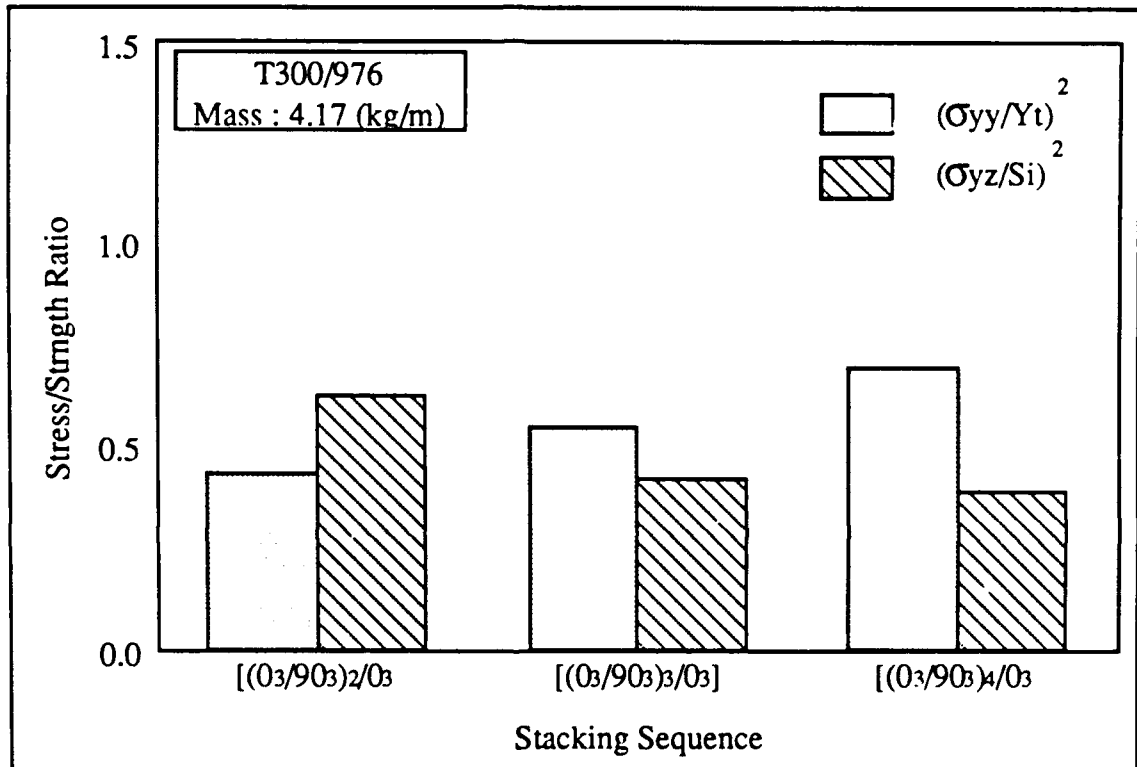


Figure 5.11: The calculated on-set interlaminar shear stress/strength and transverse tensile stress/strength ratios corresponding to impact velocity threshold for laminates with three different thicknesses.

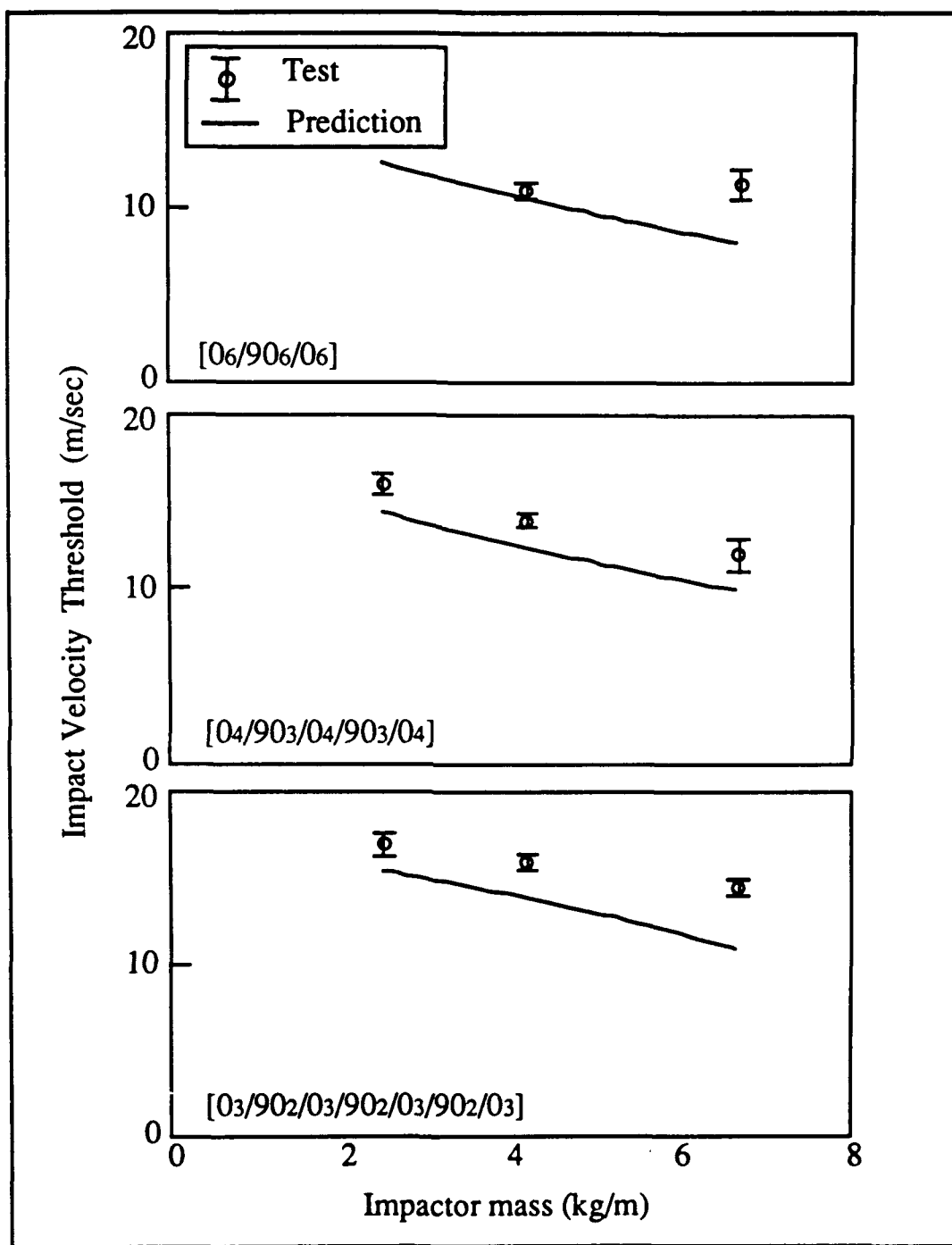


Figure 5.12: The effect of impactor's mass on the impact velocity threshold. Comparison between the test data and the predictions.

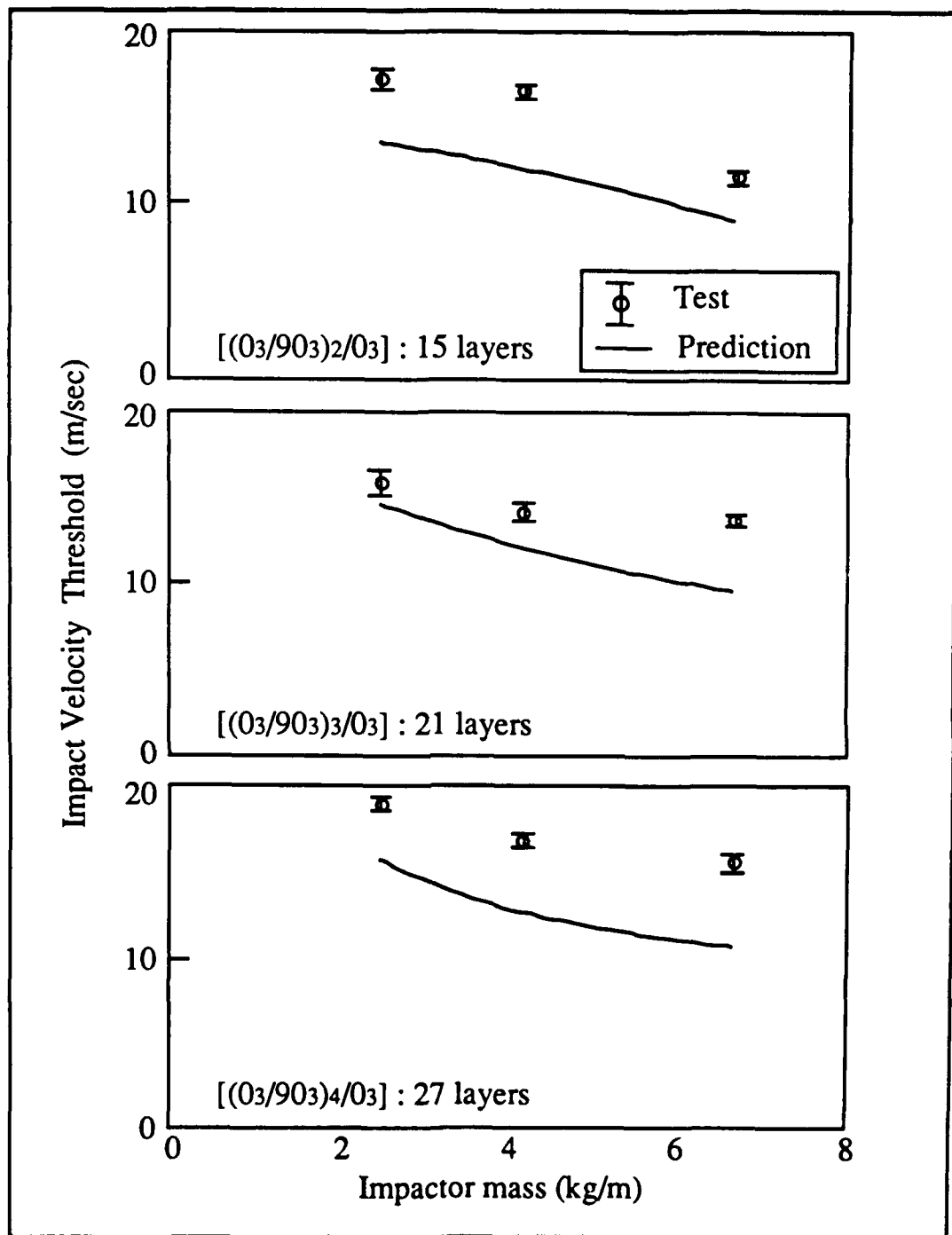


Figure 5.13: The effect of impactor's mass on the impact velocity threshold. Comparison between the test data and the predictions.

in determining impact damage in laminated composites. According to the figures, impact damage is much more sensitive to the impactor's velocity than to its mass. Given the same impact energy, an impactor may or may not cause damage, strongly depending upon the mass of the impactor. Therefore, it would be inadequate to select impact energy alone as a parameter to characterize impact damage, without specifying the mass of the impactor. Accordingly, both the impactor's mass and velocity should be identified in order to characterize impact damage in composites.

5.4 CONCLUSION

An investigation was performed to study the effect of laminate configuration and impactor's mass on impact damage in laminated composites. Both experimental and analytical work were conducted. Based on the study, the following remarks can be made:

1. ply orientation and stacking sequence can significantly affect impact damage.
2. laminates with uniformly dispersed ply orientation can increase impact resistance significantly.
3. impact damage is more sensitive to the change of stacking sequence than of thickness.
4. the mass of the impactor considerably affects the impact velocity threshold as well as impact damage.
5. interlaminar shear stress/strength and in-plane tensile stress/strength ratios dominate the initial impact damage and the impact velocity threshold.
6. both the velocity and mass of the impactor are required in order to characterize impact damage.
7. the use of impact energy alone as a parameter to characterize impact damage is inadequate.

Chapter 6

3-DIMENSIONAL POINT-LOADING IMPACT ANALYSIS AND EXPERIMENTS

6.1 INTRODUCTION

A model was developed, based on the previous study of the line-loading impact, for predicting the impact damage of Graphite/Epoxy laminated composites resulting from point-nose impact. In order to verify the model, appropriate experiments were performed during the investigation. In the following sections, the model and experiments are described, and the comparisons between the numerical simulations and the test data from the experiments are presented.

6.2 STATEMENT OF PROBLEM

Consider a laminated composite panel made of Graphite/Epoxy fiber reinforced prepreps and subjected to transverse impact by a low-velocity spherical nose projectile as shown in Figure 2.1. The ply orientation of the laminate can be arbitrary but must be symmetric with respect to its middle plane. For a given mass of the impactor, it was desired to determine the following:

1. The velocity of the impactor required to initiate the impact damage.

2. The extent of delaminations inside the laminate.
3. The effect of ply orientation and laminate thickness on the impact damage.

6.3 ANALYTICAL MODEL

A model is proposed for predicting the damage in fiber-reinforced, epoxy matrix laminated composites resulting from point-loading impact. The model consists of a stress analysis for determining the stress distributions inside the laminates during impact and a failure analysis for predicting the initiation and the extent of the impact damage. The information of the transient dynamic stress distributions is calculated by using the three-dimensional transient dynamic finite element code previously developed by Wu *et al* [13,16]. In the failure analysis, a matrix failure criterion and a delamination growth criterion are proposed for predicting the initial impact damage and the extent of the delaminations due to impact, respectively.

6.3.1 Stress Analysis

The finite element analysis previously developed by Wu *et al* [13,16] is adopted for calculating the stresses and strains inside the composites during impact resulting from a spherical nose impactor. The information regarding the finite element procedures is given extensively in [13,16], hence, only a brief description of the analytical approach is given as follows:

The analysis is based on a three-dimensional linear elasticity theory. The materials in each layer are considered homogeneous and orthotropic. Accordingly, the equilibrium equations at instant time t in a variational form can be expressed as [70]

$$0 = \int_v w_i \rho u_{i,t} dv + \int_v e_{ij} E_{ijkl} \epsilon_{kl} dv - \int_{s_\sigma} w_i \sigma_{ij} n_j da \quad (6.1)$$

where σ_{ij} are the stresses, ϵ_{kl} are the strains, ρ is the density, $u_{i,tt}$ are the accelerations ($u_{i,tt} = \partial^2 u_i / \partial t^2$), w_i are the arbitrary variational displacements, e_{ij} are the strains from the arbitrary variational displacements, v is the entire plate volume, s_σ is the surface of the plate, n_j is the outward unit normal vector on the plate surface, and E_{ijkl} are the material properties of the laminate, which may vary from layer to layer according to the ply orientation of the composite.

In order to solve Eq. (6.1), the distribution of the contact force, $F(= \sigma_{ij}n_j)$, between the impactor and the impacted laminate must first be known. The projectile is modeled as an elastic body with a spherical nose. The contact force distribution during impact is simulated according to loading and unloading processes.

Upon loading (the contact force was increased), the contact force distribution is determined using the Hertzian contact law [71]. Thus, the contact force F can be related to the indentation depth α (the distance between the center of the projectile's nose and the mid-surface of the plate) by the expression [71]

$$F = \kappa \alpha^{1.5} \quad (6.2)$$

where κ is the modified constant of the Hertz contact theory proposed by Sun *et al.* [22] and

$$\kappa = \frac{4}{3} \sqrt{r} \frac{1}{[(1 - \nu_s^2)/E_s + 1/E_{yy}]} \quad (6.3)$$

where r , ν_s , and E_s are the local radius, the Poisson's ratio, and the Young's modulus of the impactor, respectively. E_{yy} is the transverse modulus normal to the fiber direction in the upper-most composite layer.

Upon unloading, the contact force is simulated by the following relation developed by Sun *et al.* [22]

$$F = F_m \left[\frac{\alpha - \alpha_o}{\alpha_m - \alpha_o} \right]^{2.5} \quad (6.4)$$

where F_m is the maximum contact force just before unloading, α_m is the maximum indentation corresponding to F_m , and α_o is the permanent indentation during the loading/unloading process. The permanent indentation can be determined from the following expression [22]

$$\begin{aligned} \alpha_o &= 0 & \text{when } \alpha_m < \alpha_{cr} \\ \alpha_o &= \alpha_m \left[1 - \left(\frac{\alpha_{cr}}{\alpha_m} \right)^{2/5} \right] & \text{when } \alpha_m \geq \alpha_{cr} \end{aligned} \quad (6.5)$$

where α_{cr} is the critical indentation, and is approximately 0.004 inches for glass/epoxy and 0.00316 inches for graphite/epoxy.

An eight-node brick element incorporating incompatible modes is used in the finite element calculations, and a direct Gauss quadrature integration scheme is adopted [70] through the element thickness to account for the change in material properties from layer to layer within the element. Therefore, plies with different ply orientations can be grouped into an element, resulting in a significant reduction in computational time and memory space for the three-dimensional analysis.

The accuracy of the computer code is extensively verified by comparison with the existing analytical and numerical solutions [13,16]. To demonstrate the capability of the finite element analysis, Figure 6.1 shows the calculated impact force and central laminate deflection as a function of time for a T300/976 [45₄/ - 45₈/45₄] composite plate. The finite element mesh used for the calculations is also presented in Figure 6.1. The laminate is discretized into a total of $N_1 \times N_2 \times N_3$ elements. A total of four elements ($N_3 = 4$) are used through the thickness of the laminate. Because of low-velocity impact, the maximum impact force occurred at time $t = 620 \mu\text{sec}$, corresponding well to the time at which the central deflection of the plate reaches the maximum. After the rebound of the impactor, the plate vibrates harmonically.

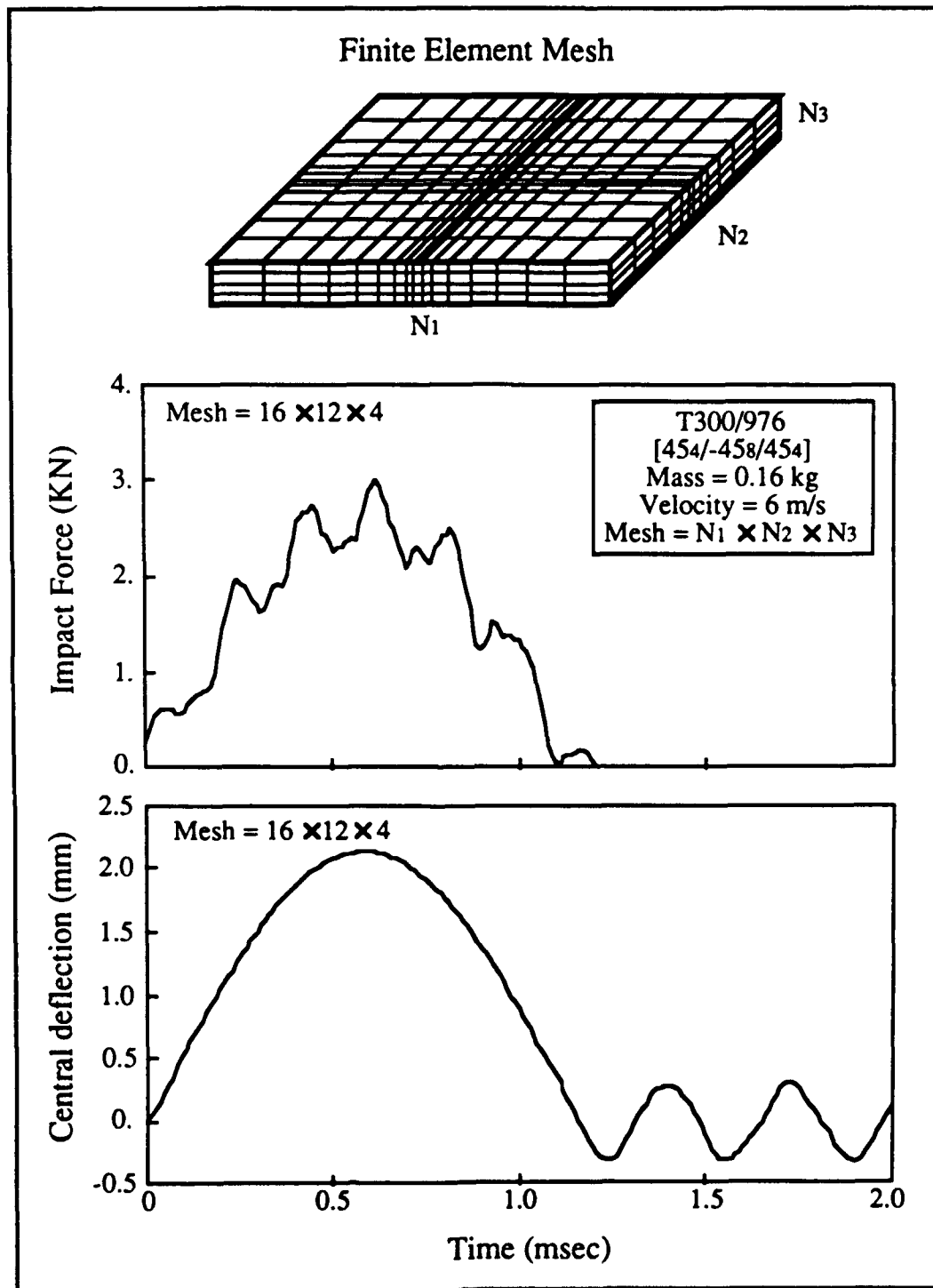


Figure 6.1: The finite element calculations of the impact force and the central deflection of a [45₄/ - 45₈/45₄] composite plate subjected to transverse impact.

6.3.2 Failure Analysis

Once the stresses are obtained from the finite element analysis, two failure criteria are proposed to predict the initiation of the impact damage and the extent of the delaminations in the composites resulting from the impact. Since impact damage is a very complicated phenomenon, predicting such damage requires a thorough understanding of the basic damage mechanisms and mechanics governing the impact damage event. Based on the previous line-loading impact study (Chapter 3, 4 and 5), the following are concluded for line-loading impact damage:

1. Intraply matrix cracking (referred to as the critical matrix cracks) is the initial impact damage mode.
2. Delaminations initiate from the critical matrix cracks which propagate into the nearby interface with the dissimilar materials.
3. If a critical crack is located within the inner plies of the laminates, the delamination along the bottom interface of the cracked ply propagates away from the location of the impact (see Figure 6.2).
4. If a critical crack is located at the surface ply of the laminate, a delamination propagates from the critical crack away from the center of the impact along the first interface of the crack ply (see Figure 6.2).

Although the results of the study are obtained from the line-loading impact, it is believed that similar phenomena occur in point-loading impact. Therefore, it is postulated that the damage mechanisms of laminated composites resulting from point-loading impact follow the same sequences as are found from line-loading impact as follows:

Transverse impact first initiates matrix cracks in a layer within the laminate. Immediately, delaminations are produced along the bottom or upper interface of the cracked layer, depending on the position of the cracked layer in the laminate. As

the duration of impact proceeds, additional matrix cracks occur subsequently in the other layers and produce additional delaminations along the other interfaces.

Critical Matrix Cracking Criterion

In order to predict the occurrence of the matrix cracking, the matrix failure criterion proposed previously for the line-loading impact is adopted here; the criterion can be expressed as

$$\left(\frac{{}^n\bar{\sigma}_{yy}}{{}^nY_t}\right)^2 + \left(\frac{{}^n\bar{\sigma}_{yz}}{{}^nS_i}\right)^2 = e_M^2 \quad \begin{cases} e_M \geq 1 & \text{Failure} \\ e_M < 1 & \text{No failure} \end{cases} \quad (6.6)$$

which is the same as Eq. (4.45) in Chapter 4.

Whenever the calculated averaged stresses in any one of the plies in the laminate first satisfy the criterion ($e_M = 1$) during impact, initial impact damage is predicted. The time t corresponding to the initial damage is designated as t_M . A delamination could immediately follow from the location of the matrix crack. As the time increases ($t > t_M$) during impact, additional matrix cracking could be produced in the other layers. Hence, the criterion should continuously be applied at the other layers for determining any additional matrix failure. It is noted that, if no additional matrix cracking is found at any other layers during impact, then the impactor's velocity associated with the only matrix cracking is defined here as the impact velocity threshold which is the velocity required to just cause the initial impact damage of the laminate.

Delamination Growth Criterion

Once a critical matrix crack is predicted in a ply within the laminate, a delamination can be initiated from the crack. To accurately simulate delamination propagation is very difficult and complicated, involving multiple dynamic crack propagation and delamination surfaces interaction. Hence, it is a formidable task to undertake. Therefore, in the investigation, a semi-empirical model is proposed to estimate the extent of delaminations in the composites after impact. Basically, there are two types of critical cracks initiating delamination resulting from impact: one can be referred to

as the shear crack generated within the laminates and the other can be referred to as the bending crack produced from the bottom surface of the laminates as shown in Figure 6.2. In order to effectively estimate the extent of the delamination growth, it is necessary to include in the model the basic governing parameters controlling the delamination propagation, once it is initiated.

It is well reported [14,30,31,33,46,53] that the delamination resulting from point-nose loading quasi-statically or dynamically appears generally in a peanut shape, as shown in Figure 6.3. The longitudinal axis of the delamination tends to orient itself in the direction parallel to the fiber direction of the bottom layer below the interface. It has also been shown that, under a quasi-static loading condition, the growth of a delamination induced by a shear crack is controlled by both Mode I and Mode II fractures due to excessive interlaminar shear stresses such as reported in [43,72,73]. The growth of the delamination along the fiber direction of the bottom layer at the interface is very unstable once it begins to propagate [73]. From the previous two-dimensional line-loading impact study (Chapters 3 and 4), it is observed empirically that the shear cracks and interface delamination always appear simultaneously and delamination always extends fully to the boundary from the matrix crack tips as shown in Figure 6.4.

However, several investigators [43,73,74] have also demonstrated recently that delamination growth induced by a bending crack is governed primarily by Mode I tensile fracture due to in-plane bending stress (transverse stress). The growth of the delamination induced by a bending crack is quite stable in the direction normal to the fiber direction of the bottom layer beneath the interface [73]. The previous two-dimensional study also reveals a stable delamination growth due to a bending crack, as shown in Figure 6.5. Hence, once a delamination is initiated from a critical matrix crack, it can grow much more extensively along the fiber direction than in the transverse direction of the bottom layer at the interface. This may provide an explanation why delamination appears to be in a peanut shape in laminated composites.

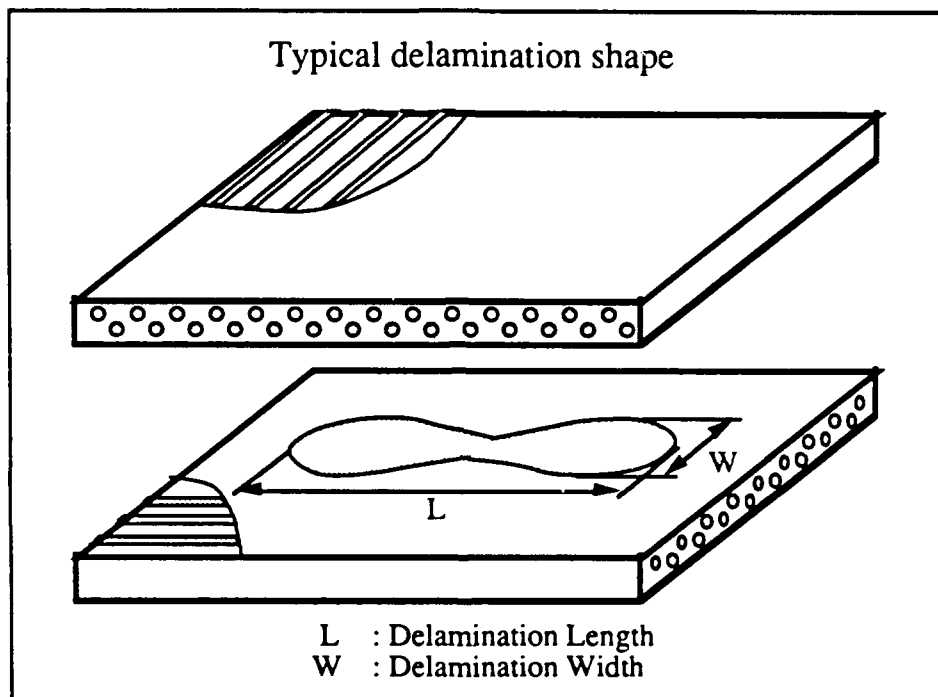


Figure 6.3: A typical delamination shape in laminated composites induced by a point nose impact.

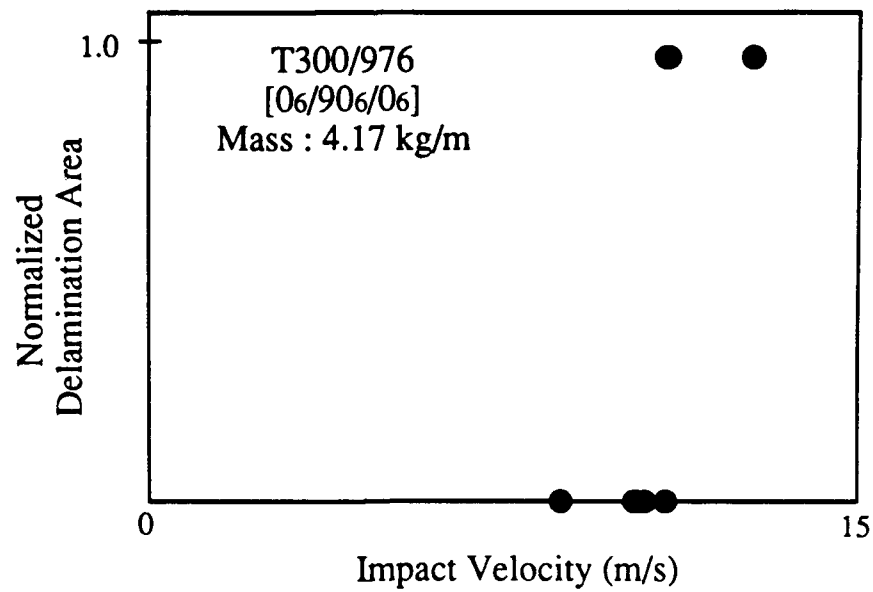


Figure 6.4: Measured delamination area within the $[0_6/90_6/0_6]$ laminated composite plates resulting from 2-dimensional line loading impact at different impact velocities. Delamination area was normalized with respect to the corresponding plate area.

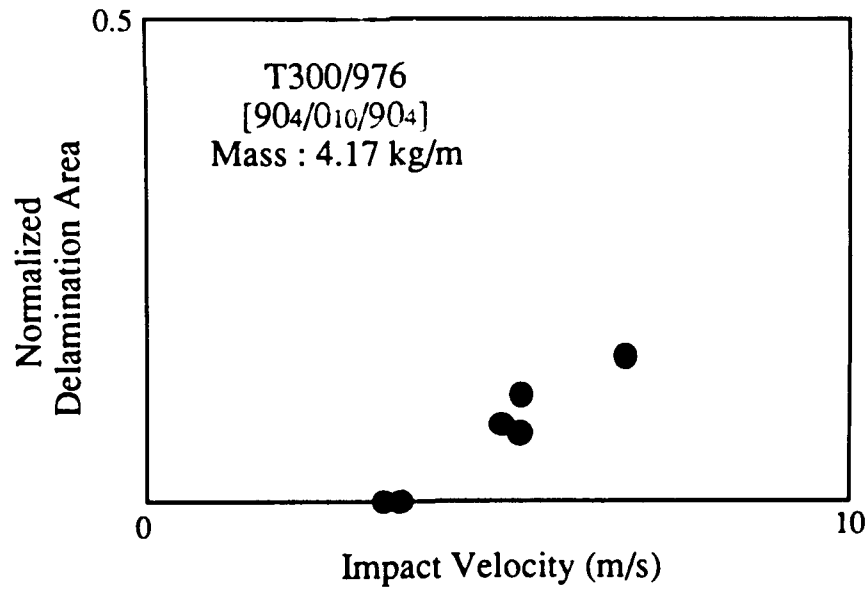


Figure 6.5: Measured delamination area within the $[90_4/0_{10}/90_4]$ laminated composite plates resulting from 2-dimensional line loading impact at different impact velocities. Delamination area was normalized with respect to the corresponding plate area.

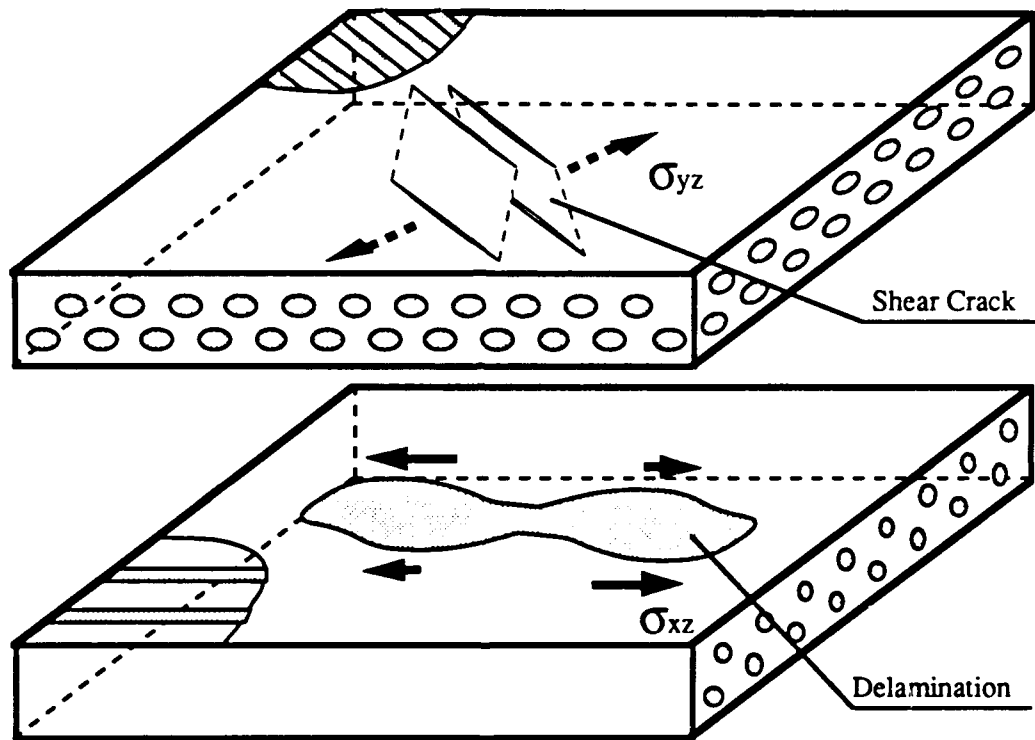
Therefore, it is believed that, for a shear-crack induced delamination, the interlaminar longitudinal shear stress (along the fiber direction) σ_{xz} in the layers right below the interface governs the major delamination growth, while the interlaminar transverse shear stress σ_{yz} in the layers right above the interface could also enhance the delamination propagation depending on the direction of its ply orientation. A schematic description of the delamination growth mechanism induced by a shear crack is shown in Figure 6.6. However, for a bending crack-induced delamination, the interlaminar longitudinal shear stress σ_{xz} in the layers right below the interface still controls the major delamination growth, but the in-plane bending stress σ_{yy} in the layers right below the interface advances the delamination propagation in the secondary direction (normal to the fiber direction). A schematic description of the delamination growth mechanism is shown in Figure 6.7.

Accordingly, by taking both failure mechanisms into consideration, it is considered that the distributions of the interlaminar longitudinal shear stress σ_{xz} and transverse in-plane stress σ_{yy} throughout the thicknesses of the bottom layer beneath the interface and the interlaminar transverse shear stress σ_{yz} in the upper layer, contribute primarily to the delamination growth resulting from point-nose impact. Therefore, it is postulated that delamination growth due to low-velocity impact occurs only when the following two sequential conditions are met:

1. one of the ply groups intimately above or below the concerned interface has failed due to matrix cracking and
2. the combined stresses governing the delamination growth mechanisms through the thicknesses of the upper and lower ply groups of the interface reach a critical value.

Based on the hypothesis, the following delamination growth criterion for low-velocity impact is proposed

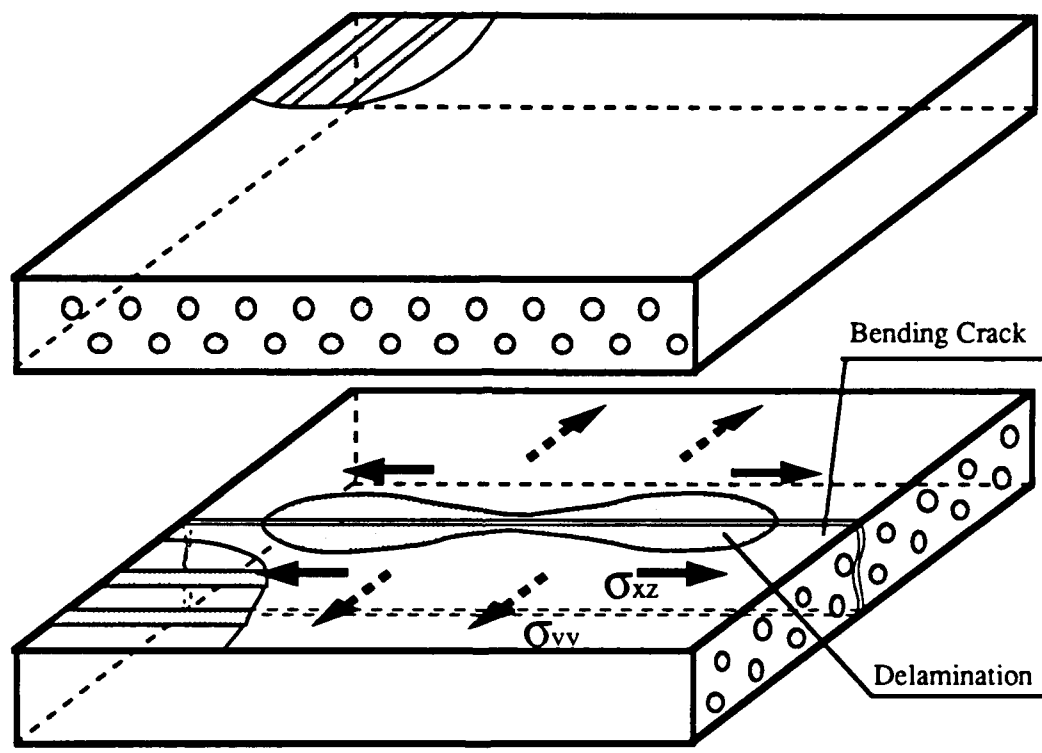
Impact Damage Growth Mechanism



Delamination induced by Shear Cracking

Figure 6.6: A schematic description of the delamination growth mechanism induced by a shear crack in a laminated composite subjected to point nose impact.

Impact Damage Growth Mechanism



Delamination induced by Bending Cracking

Figure 6.7: A schematic description of the delamination growth mechanism induced by a bending crack in a laminated composite subjected to point nose impact.

$$D_a \left[\left(\frac{{}^n \bar{\sigma}_{yz}}{{}^n S_i} \right)^2 + \left(\frac{{}^{n+1} \bar{\sigma}_{xz}}{{}^{n+1} S_i} \right)^2 + \left(\frac{{}^{n+1} \bar{\sigma}_{yy}}{{}^{n+1} Y} \right)^2 \right] = e_D^2 \quad \begin{cases} e_D \geq 1 & \text{Failure} \\ e_D < 1 & \text{No failure} \end{cases} \quad (6.7)$$

where

$$\begin{aligned} {}^{n+1} Y &= {}^{n+1} Y_t \quad \text{if } {}^{n+1} \bar{\sigma}_{yy} \geq 0 \\ {}^{n+1} Y &= {}^{n+1} Y_c \quad \text{if } {}^{n+1} \bar{\sigma}_{yy} < 0 \end{aligned} \quad (6.8)$$

D_a is an empirical constant which has to be determined from the experiments described in the Experiments section. Once D_a is chosen, it is found to be quite insensitive to the ply orientation and thickness of the laminates, and primarily dependent only on the material system used. The subscripts x , y , and z are the local material coordinates of an individual ply within the laminate, and the superscripts n and $n+1$ correspond to the upper and lower ply groups of the n -th interface, respectively. $\bar{\sigma}_{yz}$ and $\bar{\sigma}_{yy}$ are the averaged interlaminar and in-plane transverse stresses within the n -th and $n+1$ -th ply, respectively, defined in Eq. (4.46) and (4.47). $\bar{\sigma}_{xz}$ is the averaged interlaminar longitudinal stresses within the $n+1$ -th ply which can be expressed as

$${}^{n+1} \bar{\sigma}_{xz} = \frac{1}{h_n} \int_{t_{n-1}}^{t_n} \sigma_{xz} dz \quad (6.9)$$

where t_n and t_{n-1} are the upper and lower interfaces of the n -th ply or ply group in the laminate and h_n is the thickness of the ply or the ply group.

Accordingly, once a critical matrix crack is predicted in a layer, the delamination growth criterion is then applied to estimate the extent of the delamination along the interface of the cracked ply in the laminate. The procedure for determining the extent of the impact damage can be described as follows:

1. Calculating transient dynamic stresses within each layer as a function of time.
2. Applying the matrix failure criterion for predicting the critical matrix cracks in each layer.

3. If matrix cracking is predicted in a layer of the laminate, applying the delamination criterion subsequently in the upper and bottom layer of the interface during the entire period of impact.

The above procedure is repeated at the other layers during impact for determining any additional matrix cracking and delaminations. The final size of each delamination is determined by the area within which the stress components satisfy the delamination growth criterion during the entire duration of impact. No material degradation was considered in the model, and it is also noted that the model does not take into account the delamination interaction during impact which may be important for multiple delaminations.

6.4 EXPERIMENTS

In order to verify the proposed model, numerical predictions from the model were compared with the data generated by the tests performed during the investigation. The same impact testing facility described in Chapter 3 was used for the experiments. A spherical-nosed impactor was selected for the study (see Figure 3.2). The radius of the spherical nose head made of steel was 0.635 cm. The specimens were firmly clamped along two parallel edges as shown in Figure 3.1.

T300/976 composites were selected for the study. Numerous different ply orientations were chosen. The dimensions of each specimen were 10 cm long and 6.6 cm wide. Table 6.1 lists the ply orientations and the configurations of the specimens used in the tests. All the specimens were cured under the cure cycle previously mentioned in Chapter 3 which was found to produce finished composites of fairly good quality, without thermal-induced pre-matrix cracks. All the specimens were cut by a diamond coated saw and X-rayed after the cutting to inspect any internal damage due to manufacturing and cutting. No apparent damage was found after cutting the specimens.

Ply Orientation	Thickness (h) (mm)	Span length (L) (cm)	Width (W) (cm)
[454/-458/454]	2.30	10.0	7.6
[03/903/03/903/03]	2.16	10.0	7.6
[04/452/-454/452/04]	2.30	10.0	7.6
[04/454/-454/904/-454/454/04]	4.03	10.0	7.6

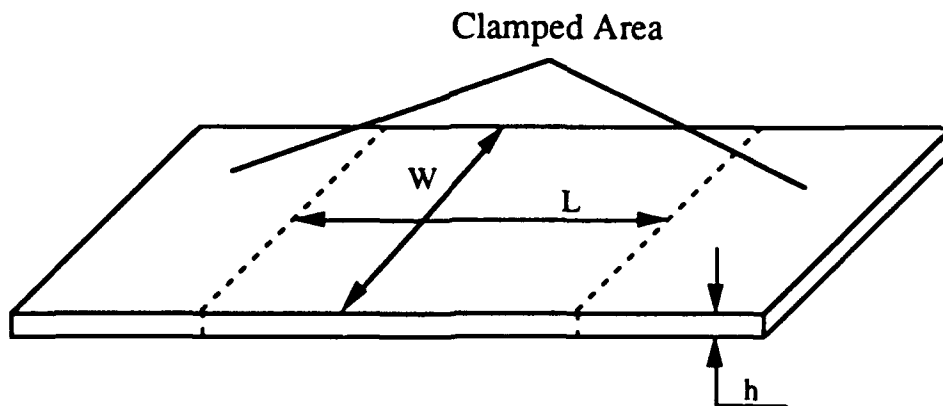


Table 6.1: Ply orientations and geometries of the test specimens.

Fifteen replicants were prepared for the three ply orientations: $[45_4/ - 45_8/45_4]$, $[0_3/90_3/0_3/90_3/0_3]$, and $[0_4/45_2/ - 45_4/45_2/0_4]$. Each specimen was impacted only once at a selected impact velocity. Specimens were then X-rayed using enhanced dye-penetrant. For some specimens without any visual surface damage, dye might not have penetrated effectively into the specimens to produce maximum effect. In these cases, a small hole was drilled at the impacted location and dye-penetrant was applied through the hole. An X-Radiograph was then taken. For a given configuration, the velocity of the impactor was started at a very low level and gradually increased until a considerable amount of damage was visualized from X-Radiographs.

The velocity just causing the initial matrix cracking was recorded and considered as the impact velocity threshold for the test specimen under the given boundary condition. A peanut shape as given in Figure 6.4 was found to be the typical shape for the delaminations from the X-Radiographs. This is also consistent with the findings observed by other investigators [14,30,31,33,46,53]. The sizes of the delaminations shown in the X-radiographs were then measured and recorded in terms of their length (longitudinal direction) and width (transverse direction) as a function of the impactor's velocity. Although the delamination size would be estimated from the X-Radiographs indicated by the white color area, the actual size of the delamination was still very difficult to determine, especially when the delamination size was small. In order to confirm the direct measurement of the delamination size from the X-Radiographs, selected specimens were also sliced along the longitudinal or transverse axis of the relevant delamination, and the sliced cross-section of the specimens was then X-rayed. The length and width were then remeasured to compare with the previous measurements. Overall, both types of measurements were quite consistent with each other. However, an error of about ± 10 percent in the measurement from the actual size could possibly have been introduced. The measured delamination sizes are summarized in the Appendix C.

6.5 SENSITIVITY STUDY

Determining the value of D_a in the delamination growth criterion requires the use of impact test results. The measured delamination sizes and shapes from X-radiographs were used for determining the value. The test results of $[0_3/90_3/0_3/90_3/0_3]$ composites were first selected and compared with numerical simulations based on the model. A value of 1.8 was chosen for D_a because the prediction of the delamination sizes would best fit the measured test data.

In order to determine the sensitivity of the empirical constant D_a to lamination configuration, the delamination lengths of the laminates with three tested ply orientations were calculated from the values of D_a varying in a wide range. The calculated lengths were then compared with the corresponding data from the experiments. A formula [75] was selected to estimate the discrepancies between the predictions and measurements based on various of D_a . The error formula is expressed as

$$Err^2 = \frac{1}{L^2 N_t} \sum_{i=1}^{N_t} (L_c^i - L_t^i)^2 \quad (6.10)$$

where

$$\begin{aligned} L_c &= \text{Calculated Delamination Length} \\ L_t &= \text{Tested Delamination Length} \\ L &= \text{Specimen Length (10 cm)} \\ N_t &= \text{Number of Test points} \end{aligned} \quad (6.11)$$

The comparison of the study is presented in Figure 6.8. As can be seen clearly, the value of D_a which best matched to the data varied from 1.2 to 2.0 for the ply orientations studied. An average value of 1.8 would be a fair selection for T300/976 composites. The effect of the variation of D_a values on the prediction of the delamination size can also be seen from the Figure 6.8. Depending upon the location of the delamination in laminates, Figure 6.8 shows that a change of the parameter by up to $\pm 50\%$ from the averaged value does not affect significantly the predicted delamination size. Therefore, it seems that the value of D_a is insensitive to the change of ply

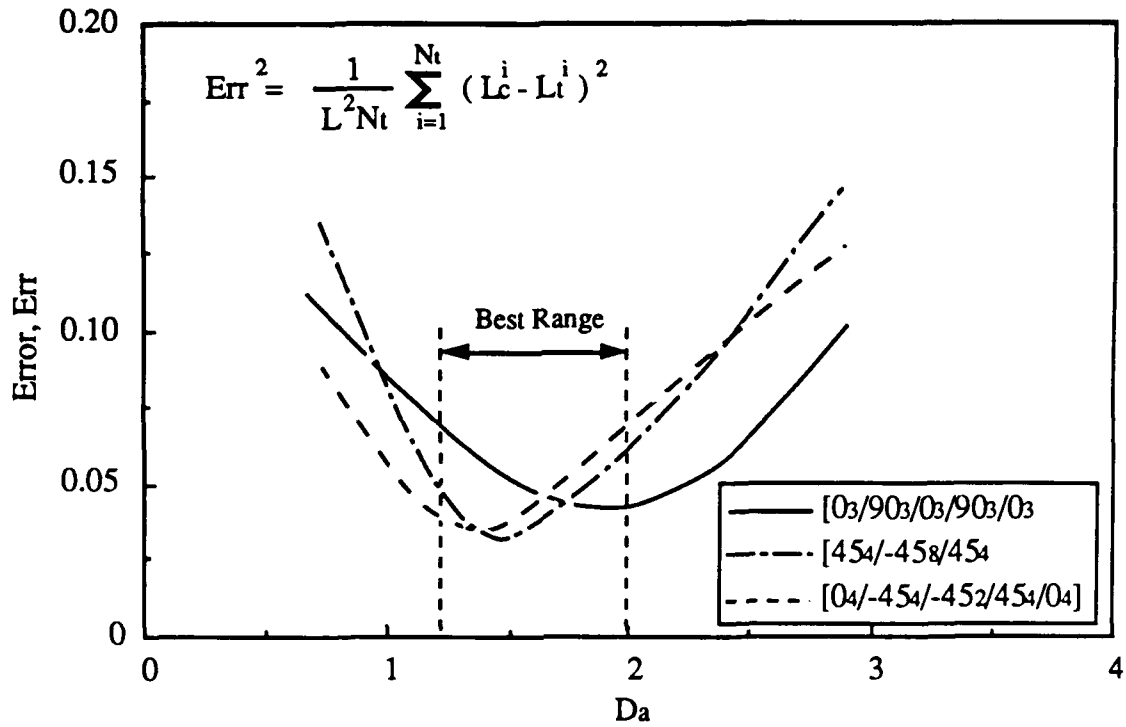


Figure 6.8: The sensitivity evaluation of the effect of D_a value on the predicted delamination size as compared to the experiments.

orientation and thickness, but may depend on the material system chosen. However, a study may be needed to further evaluate the characteristic of the parameter. In this investigation, once the value of D_a was determined, it was then used as a constant in the model for the T300/976 composites. The material properties of T300/976 composites used in the calculations are listed in Table 4.1. The results of the predictions compared with experiments are presented in the next section.

In order to evaluate the effect of finite element mesh size on the stability of the numerical predictions based on the model, numerical calculations are obtained based on different meshes, ranging from very fine to rather coarse. Figure 6.9 shows the comparisons of the calculations in which the meshes were generated by proportionally decreasing or increasing the number of elements along length (N_1) and width (N_2) direction of the laminate while keeping the number of total elements (N_3) through the

thickness fixed. It can be seen that the predicted delamination sizes quickly converged as the number of the elements was more than 192 ($N_1(= 16) \times N_2(= 12)$), beyond which the calculated maximum impact force and maximum deflection of the plate were also fairly stabilized. The results indicate that the proposed failure analysis does not require the use of an extensively fine mesh. Therefore, a regular mesh of 768 ($N_1(= 16) \times N_2(= 12) \times N_3(= 4)$) was used in the numerical calculations for generating the results in comparison with the test data.

6.6 RESULTS AND DISCUSSIONS

[45₄/ - 45₈/45₄]

Figure 6.10 shows three X-Radiographs of [45₄/ - 45₈/45₄] composites in series after being hit each at a different velocity by an impactor. The top X-radiograph was taken from the laminate subjected to impact at a velocity slightly above the impact velocity threshold of the laminate. Two distinct, parallel, short matrix cracks which are located near the impacted area within the middle -45 degree ply group of the laminate are clearly shown in Figure 6.10. A long matrix crack aligned in the 45 degree fiber direction and located in the bottom 45 degree ply group is also clearly indicated. These cracks are most likely associated with the critical matrix cracks from which delamination is initiated. A white color area in a peanut shape oriented along the 45 degree fiber direction shows that a delamination exists at the interface between the middle -45 degree ply group and the bottom 45 degree ply group.

As the impactor's velocity increased, the first delamination found at the last interface between -45/45 ply groups was substantially increased, as shown in the X-Radiograph located at the middle of Figure 6.10. Meanwhile, a relatively smaller delamination at the first interface between 45/ - 45 ply groups was also spotted, in addition to a considerable number of microcracks in the 45 and -45 degree ply groups. At a much higher velocity, as given in the X-Radiograph at the bottom of Figure 6.10, the first delamination at the last interface always governed the major

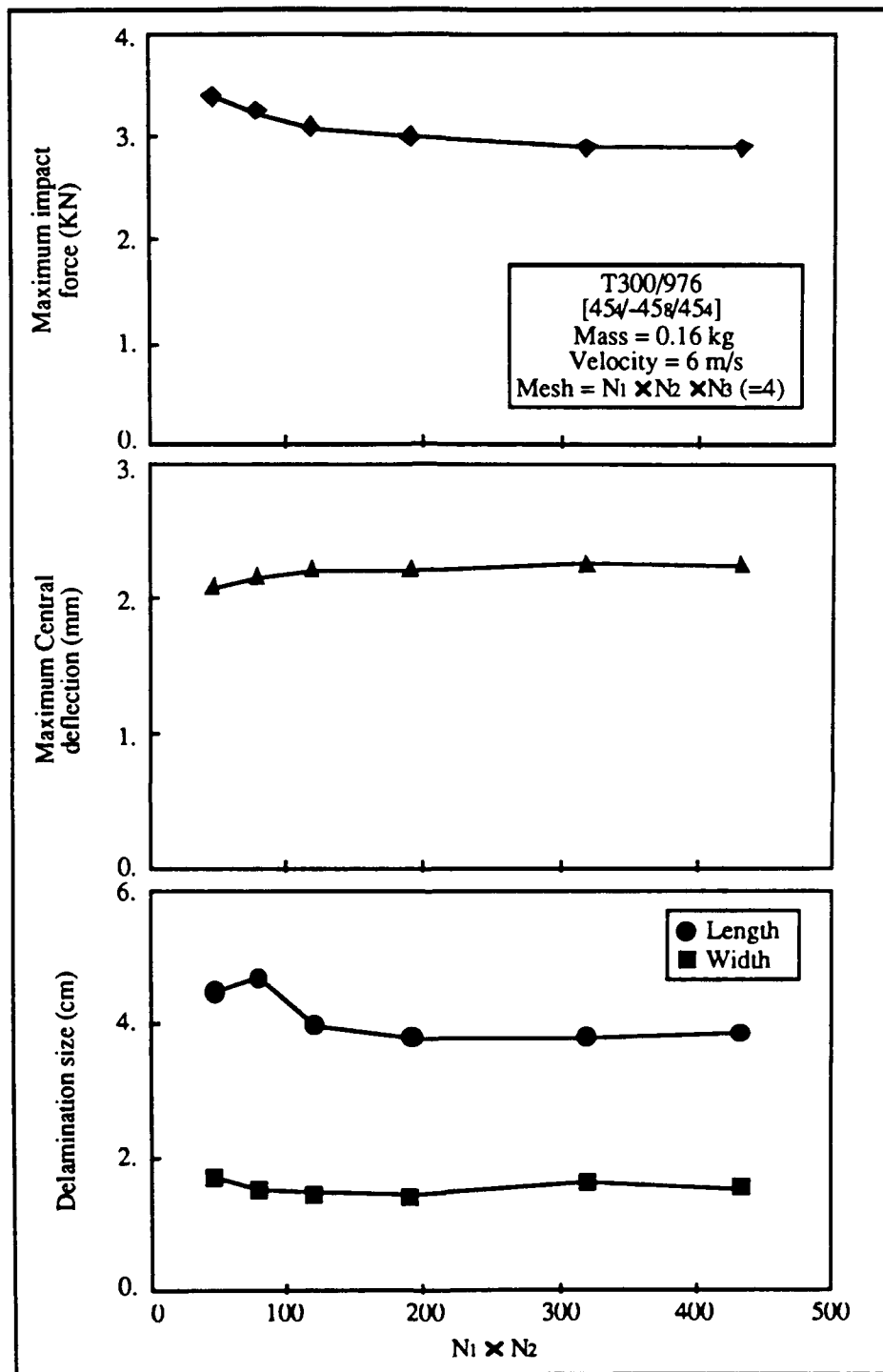
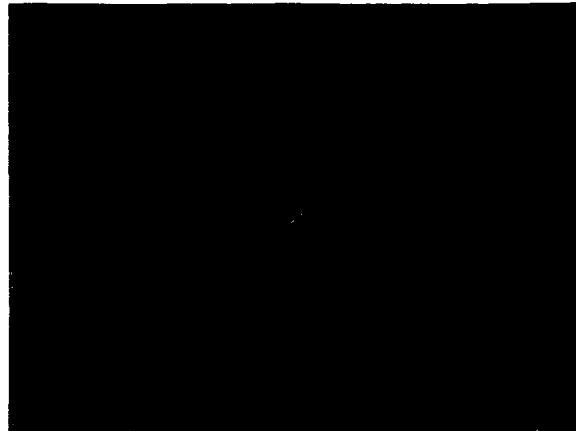
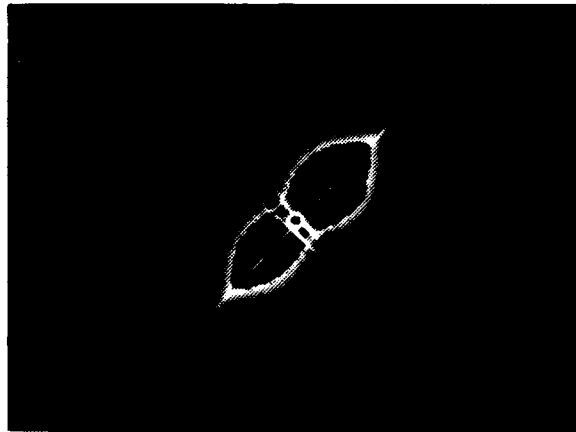


Figure 6.9: The sensitivity evaluation of the effect of finite element mesh size on the calculated delamination sizes based on the proposed model.

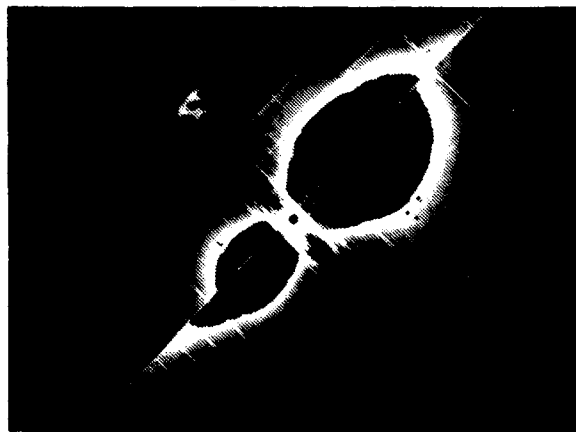
T300/976 [45₄/-45₈/45₄]



Mass = 0.16 kg Velocity = 4.15 m/s



Mass = 0.16 kg Velocity = 5.89 m/s



Mass = 0.16 kg Velocity = 9.02 m/s

Figure 6.10: Three X-Radiographs of [45₄/ - 45₈/45₄] composites in series subjected to impact by a spherical nosed projectile at three different velocities.

delamination size, which was considerably larger than the second delamination.

A summary of the measured delamination sizes in $[45_4 / -45_8 / 45_4]$ composites as a function of the velocity of the impactor with 0.16 kg is shown in Figure 6.11. Solid circular and rectangular symbols represent the measured delamination length and width in the longitudinal and transverse directions as a function of the impactor's velocity, respectively. The upper figure corresponds to the first delamination along the $-45/45$ degree plies interface, and the bottom one relates to the second delamination which occurred at the upper $45 / -45$ degree plies interface.

Clearly, there exists an impact velocity threshold for the laminate. The first delamination apparently appears much earlier than the second delamination. There also seems to be a velocity threshold for the occurrence of each delamination. It is worth noting that no matrix cracks or delaminations were found in the laminate in the X-Radiographs when the impactor's velocity was less than 3.3 m/s.

The predicted delamination size at each interface as a function of the impactor's velocity is presented by the solid and dashed lines in Figure 6.11. The impact velocity threshold is slightly underestimated but still agrees with the data reasonably well. The first critical matrix cracking is predicted at the middle -45 degree layer of the laminate. The predicted delamination length and width also correlate well with the data. Not only does the prediction match with the size of the first delamination, but also it correlates very well with the initiation and the size of the second delamination.

Although the test data is quite scattered, a relationship which is quite consistent with the predictions seems to exist between the delamination size and the velocity of the impactor. The longitudinal length of the delamination seems to be more sensitive than the transverse width to the increase in the impactor's velocity. The longitudinal length of the delamination is always oriented along the fiber direction of the bottom ply below the delamination interface.

As a comparison, the numerical simulations of the delamination size of the composites subjected to impact at the velocities corresponding to those given in Figure

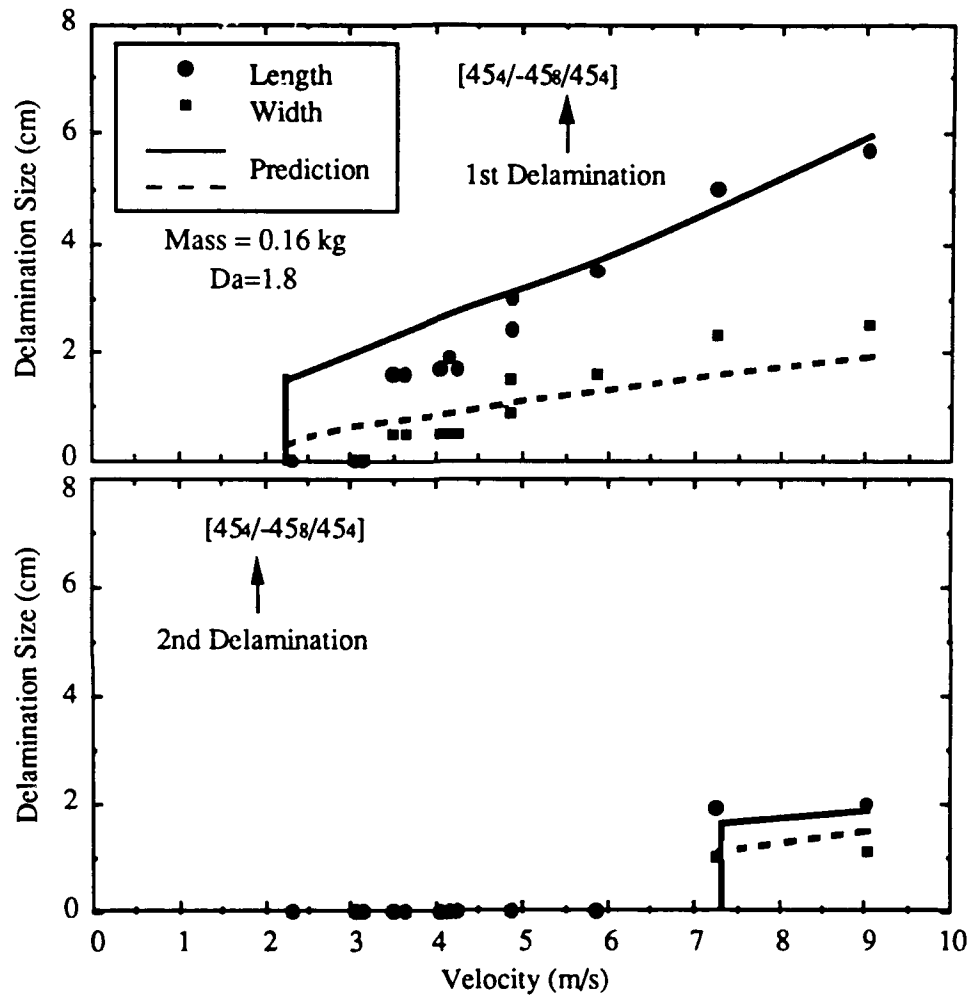


Figure 6.11: Comparison of the delamination sizes of T300/976 [45₄/ - 45₈/45₄] composites between the measurements from the experiments and the calculations based on the model.

6.10 are generated, and the results of the predictions are plotted in Figure 6.12. The delamination contours shown in Figure 6.12 bound the area of the predicted delamination. Corresponding to each velocity given in Figure 6.10, the predicted shape and size of each delamination shown in Figure 6.12 are quite consistent with the results of the X-Radiographs given in Figure 6.10.

$[0_3/90_3/0_3/90_3/0_3]$

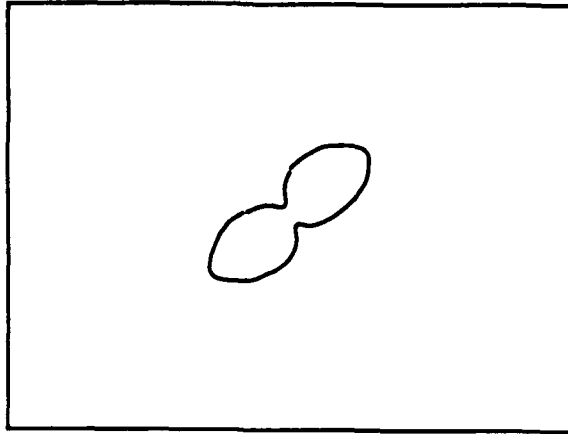
The X-Radiographs of three $[0_3/90_3/0_3/90_3/0_3]$ composites impacted by an impactor at three different velocities are shown in Figure 6.13. Again, the impact damage shown in the top X-Radiograph given in the figure corresponds to the impact velocity threshold. Differing from $[45_4/-45_8/45_4]$ composites, only a single matrix crack located along the center line of the bottom 0 degree plies was found. A small peanut-shaped delamination was also found located at the interface between the last 90 degree ply group and the cracked outermost 0 degree ply group.

Multiple delaminations occurred in the laminates as shown in the middle and bottom X-Radiographs of Figure 6.13, as the impactor's velocity increased. Again, each delamination oriented itself along the fiber direction of the bottom ply of the delaminated interface. Three delaminations were found in the X-Radiographs which were also confirmed by a X-Radiograph taken from a cross-section of a sliced specimen. The major delamination size was still governed by the first delamination which occurred at the bottom interface.

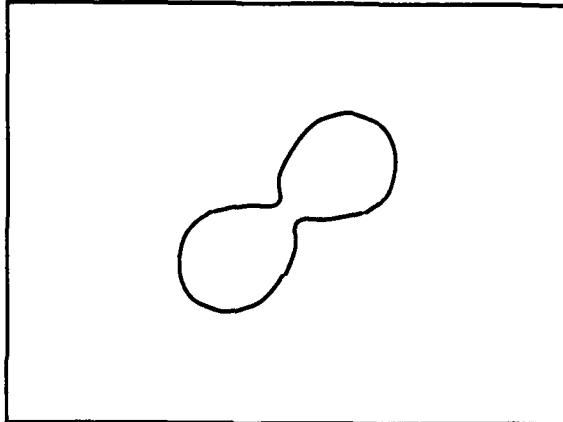
The measured length and width of each delamination in $[0_3/90_3/0_3/90_3/0_3]$ composites as a function of impactor's velocity are presented in Figure 6.14. Since only three delaminations occurred in the laminates, no delamination was found at the first $0_3/90_3$ interface. The first delamination which occurred at the last interface appeared earlier than the others. The results of the test indicate that the size of the first delamination is much more sensitive to the impactor's velocity than are the other delaminations.

The predicted delamination length and width for each delamination as a function

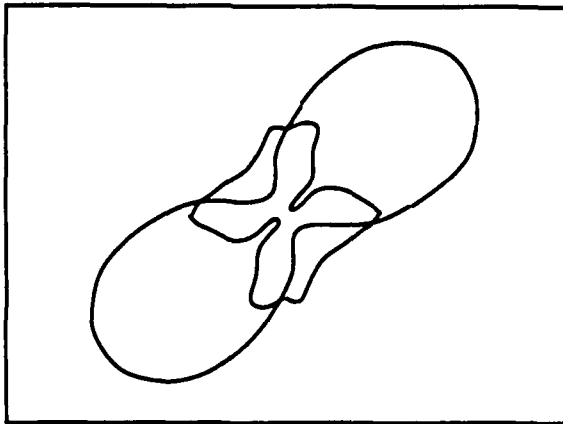
T300/976 [45₄/-45₈/45₄]



Mass = 0.16 kg Velocity = 4.15 m/s



Mass = 0.16 kg Velocity = 5.89 m/s



Mass = 0.16 kg Velocity = 9.02 m/s

Figure 6.12: The predicted delamination sizes of [45₄/ - 45₈/45₄] composites corresponding to the impact condition given in Figure 6.10.

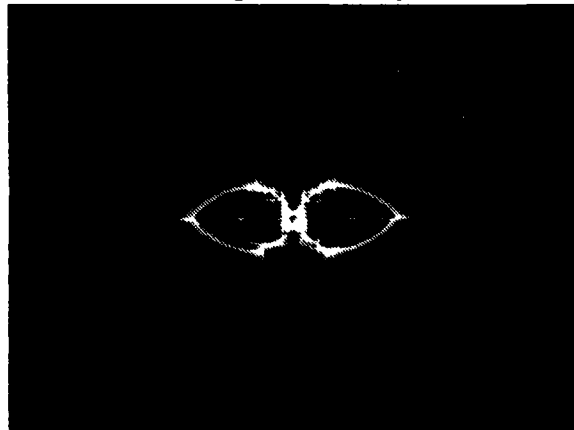
T300/976 [0₃/90₃/0₃/90₃/0₃]



Mass = 0.16 kg Velocity = 3.22 m/s



Mass = 0.16 kg Velocity = 4.0 m/s



Mass = 0.16 kg Velocity = 6.70 m/s

Figure 6.13: Three X-Radiographs of [0₃/90₃/0₃/90₃/0₃] composites in series subjected to impact by a spherical nosed projectile at three different velocities.

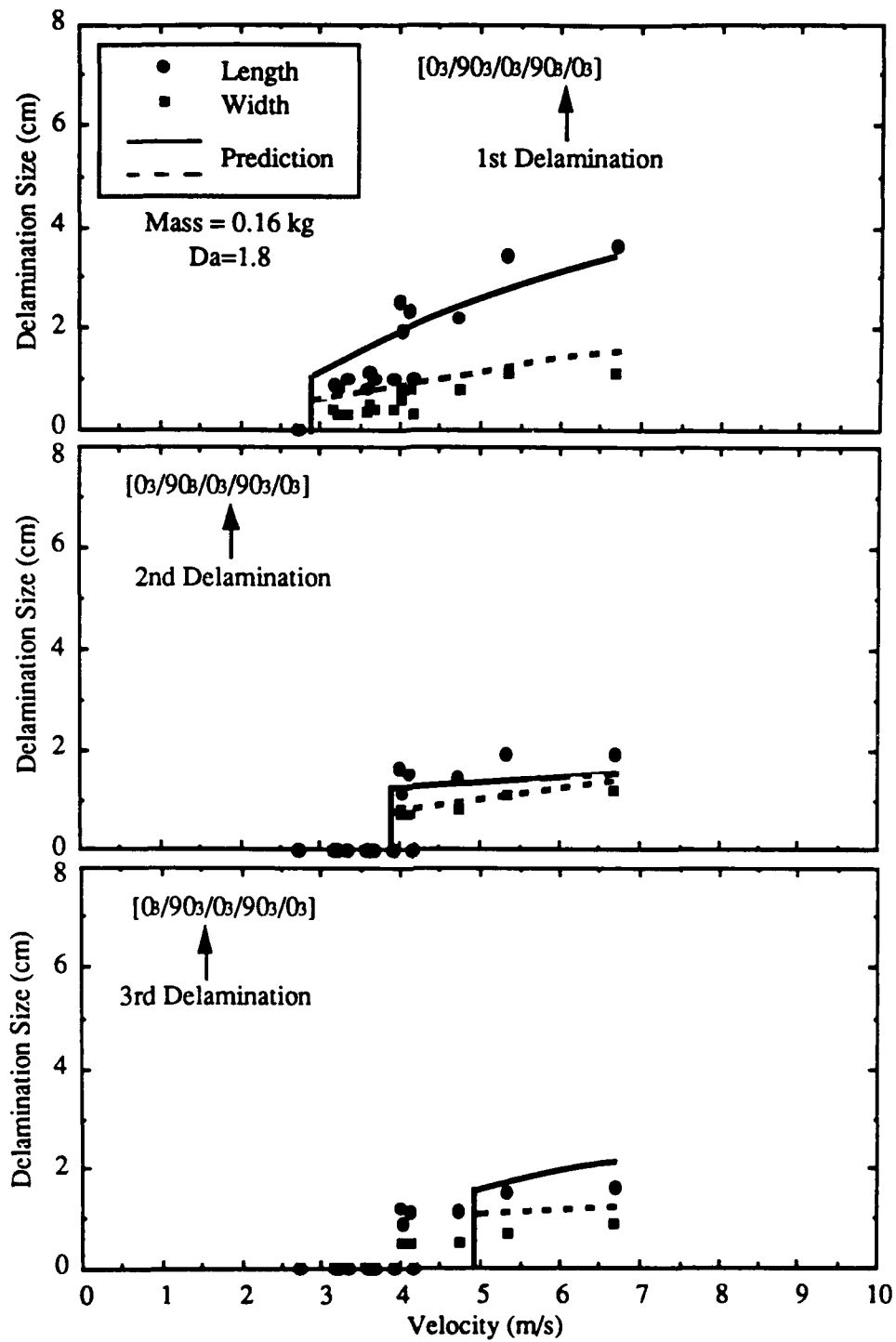


Figure 6.14: Comparison of the delamination sizes of T300/976 $[0_3/90_3/0_3/90_3/0_3]$ composites between the measurements from the experiments and the calculations based on the model.

of the impactor's velocity are also indicated in Figure 6.14 by solid and dashed lines. It is worth noting that the model predicts matrix cracking at the bottom 0 degree plies as the initial failure mode, which correlates very well with the X-Radiograph's finding, shown in Figure 6.13. The predicted impact velocity threshold is also very close to the measured one. A delamination is predicted to be generated at the last interface between 90₃/0₃ ply groups immediately after the occurrence of matrix cracking.

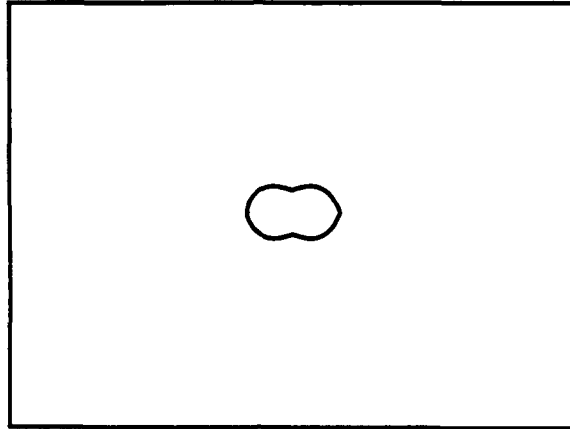
Matrix cracking is also predicted afterward in the inner 90 and 0 degree plies which initiates second and third delaminations as shown in Figure 6.14. Overall, the predicted delaminations are quite consistent with the measured ones. No matrix cracking is predicted in the top surface 0 degree ply group, hence there is no delamination predicted to occur at the first interface between the surface 0 degree ply group and the second 90 degree ply group. This prediction is also confirmed by the experiment.

The experimental results shown by the X-Radiographs given in Figure 6.13 are numerically simulated by the model. The numerical simulations of the delamination sizes corresponding to the test conditions are shown in Figure 6.15. Compared to Figure 6.13, the prediction slightly overestimates the initial size of the first delamination. However, the overall correlations between the predictions and the results of the X-Radiographs are fairly good, especially at higher velocities.

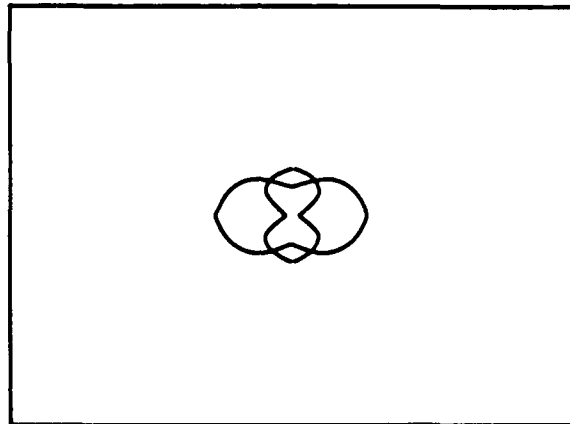
[0₄/45₂/ - 45₄/45₂/0₄]

Figure 6.16 shows the X-Radiographs of [0₄/45₂/ - 45₄/45₂/0₄] composites resulting from impact by an impactor with a mass of 0.16 kg at three different velocities. The lowest velocity corresponded to the impact velocity threshold of the composites. Only a long 0 degree matrix crack in the bottom ply group was found from the X-Radiograph as well as by the eye inspection of the surface of the specimen. Apparently, this matrix crack was the initial failure mode. No delamination was found from the X-Radiograph of this particular specimen, but an X-Radiograph taken from a specimen impacted at slightly higher velocity shows a sign of delamination near the impacted area in Figure 6.16. Except for the first interface between the 0 degree

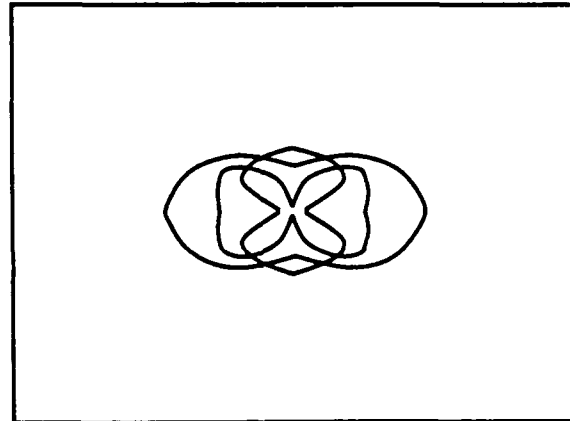
T300/976 [0₃/90₃/0₃/90₃/0₃]



Mass = 0.16 kg Velocity = 3.22 m/s



Mass = 0.16 kg Velocity = 4.0 m/s



Mass = 0.16 kg Velocity = 6.70 m/s

Figure 6.15: The predicted delamination sizes of [0₃/90₃/0₃/90₃/0₃] composites corresponding to the impact condition given in Figure 6.13.

surface ply group and the second 45 degree ply group, delaminations were found at the rest of the interfaces.

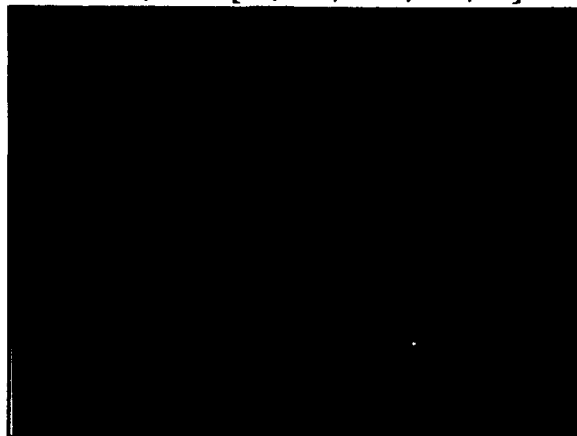
The measured delamination lengths and widths as a function of the impactor velocity are presented in Figure 6.17. The first delamination was initiated at the last interface between the $45_2/0_4$ ply groups and appeared earlier than the other delaminations. Delaminations with relatively smaller sizes were also found at the second and third interfaces of the laminates at higher impactor velocities. Again, it seems that the first delamination governed the overall delamination size and was much more sensitive to the impactor's velocity than the other delaminations. No delamination was found at the first interface between the surface 0 degree ply group and the second 45 degree ply group.

The predictions of the delamination length and width of the composites as a function of the impactor's velocity are also shown in Figure 6.17 along with the test data. According to the prediction, matrix cracking at the bottom 0 degree layer group is the initial failure mode which initiated the first delamination at the last interface between $45_2/0_4$ ply groups. This prediction is consistent with the finding from the X-Radiograph shown in Figure 6.16. The model slightly underestimated the impact velocity threshold of the laminate and the threshold velocity corresponding to the occurrence of the second delamination, but the predictions are correlated fairly well with the measured first and second delamination sizes.

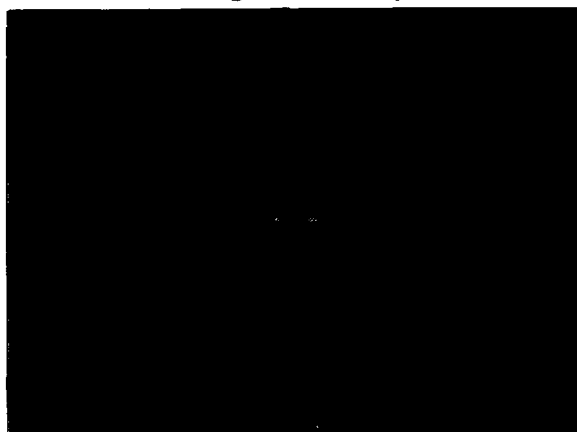
However, the model considerably overestimated the velocity threshold corresponding to the occurrence of the third delamination. The test data shows that both the second and third delaminations initiate at roughly the same time, but the prediction indicates that the third delamination will occur at a much later time than the second. In order to initiate the third delamination, the model predicts that matrix cracking in the 45 degree ply group would occur much later than the matrix cracking in the -45 ply group which initiates the second delamination.

The early occurrence of the matrix cracking in the 45 degree ply group from the

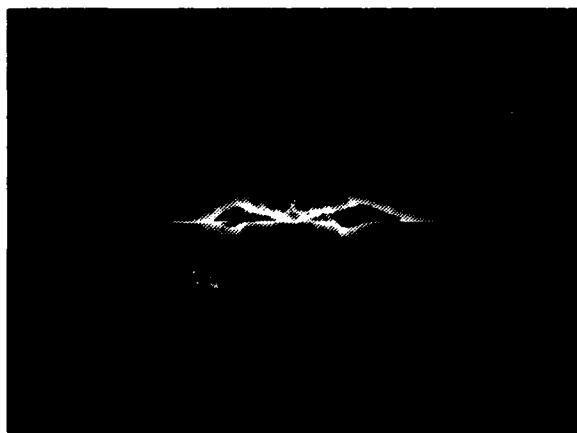
T300/976 [0₄/45₂/-45₄/45₂/0₄]



Mass = 0.16 kg Velocity = 2.51 m/s



Mass = 0.16 kg Velocity = 3.90 m/s



Mass = 0.16 kg Velocity = 5.90 m/s

Figure 6.16: Three X-Radiographs of [0₄/45₂/ - 45₄/45₂/0₄] composites in series subjected to impact by a spherical nosed projectile at three different velocities.

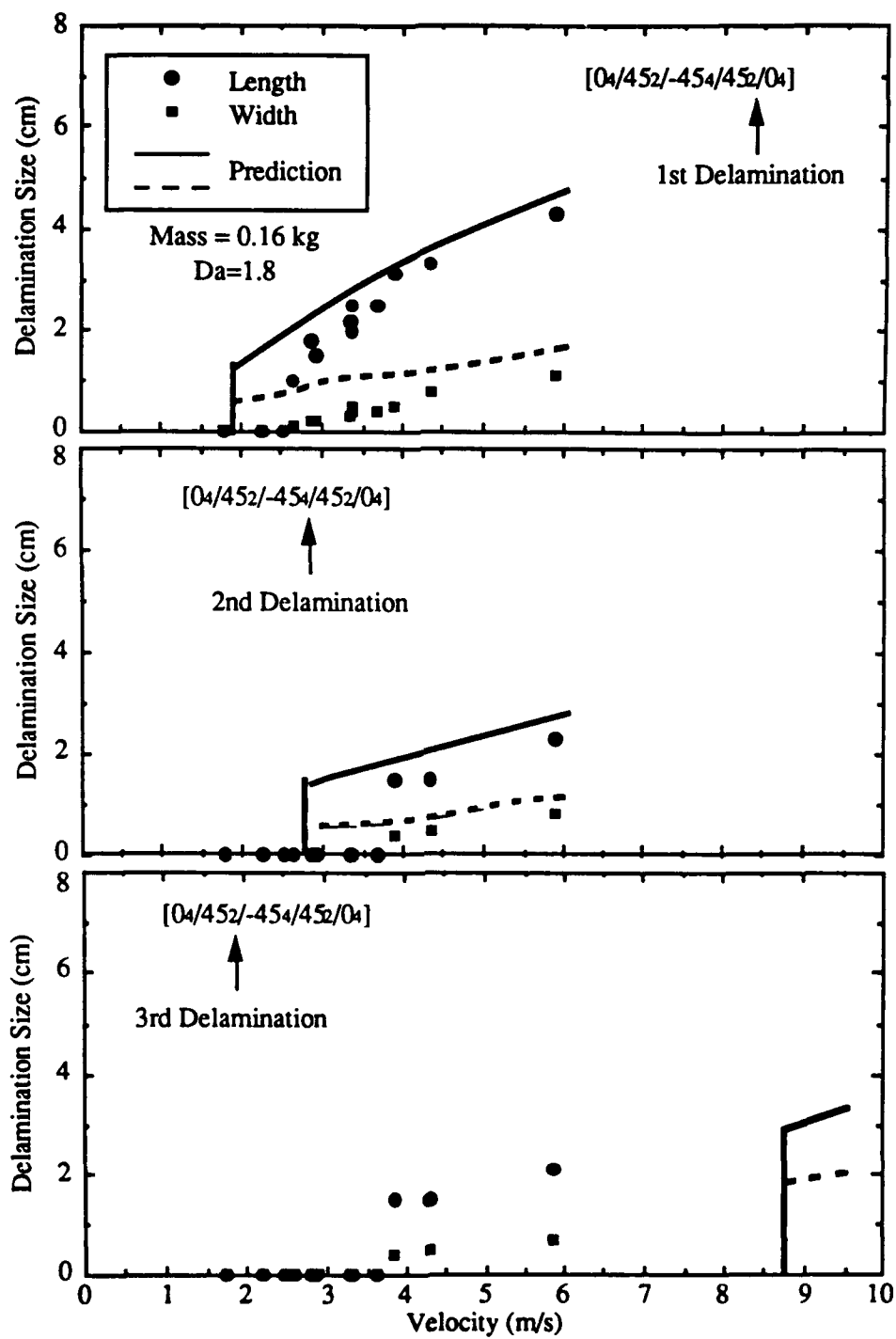


Figure 6.17: Comparison of the delamination sizes of T300/976 $[0_4/45_2/-45_4/45_2/0_4]$ composites between the measurements from the experiments and the calculations based on the model.

experiment may have been caused by the loss of material properties in the neighborhood of the impacted area due to the combined damage of the cracking in the -45 degree ply groups and the first and second delaminations. Such interaction among delaminations and matrix cracks, apparently significant in $[0_4/45_2/-45_4/45_2/0_4]$ composites, is not considered in the model. Therefore a progressive failure analysis taking into account material degradation due to damage would be necessary to accurately model the damage interaction during impact.

In Figure 6.18, the numerical simulations of the delaminations of the test results given in Figure 6.16 are presented. Overall, the predicted delamination sizes are quite consistent with the results of X-Radiographs shown in Figure 6.16.

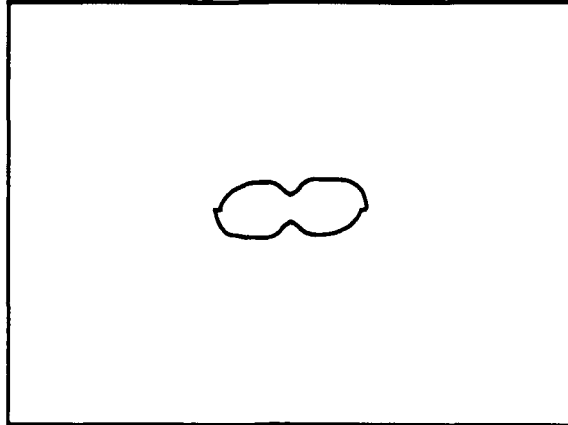
$[0_4/45_4/-45_4/90_2]_S$

Quasi-isotropic laminates were also tested at two selected velocities, and the results of the test are shown by X-Radiographs in Figure 6.19. Delaminations were found at each interface, and each delamination also oriented itself along the fiber direction of the bottom ply group below the delaminated interface. The predicted delamination sizes of the composites corresponding to the test condition are also presented in Figure 6.19. The model predicts a delamination occurring at each interface, consistent with the test results. The predicted overall size and shape of the delaminations compared to the X-Radiograph pictures both given in Figure 6.19 are fairly accurate. The predicted delamination size and shape at each interface within the laminate subjected to impact at velocity of 7.8 m/s are presented in Figure 6.20.

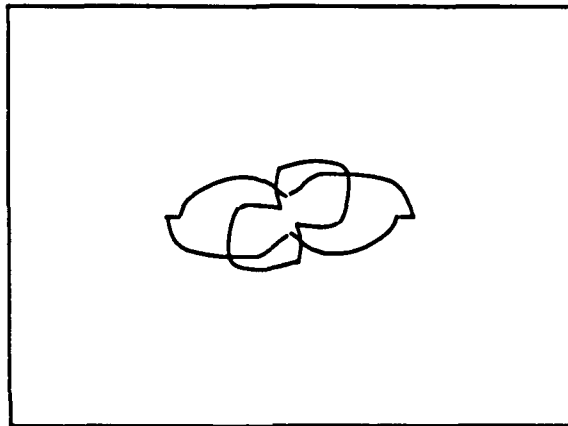
6.7 CONCLUSION

An investigation was performed to study impact damage in Graphite/Epoxy laminated composites resulting from point-nose impact. A model was developed for predicting the initiation of the damage and the extent of the delaminations in Graphite/Epoxy laminated composites resulting from the impact. Experiments were also performed to verify the model and the computer simulations. Based on the model, a user-friendly

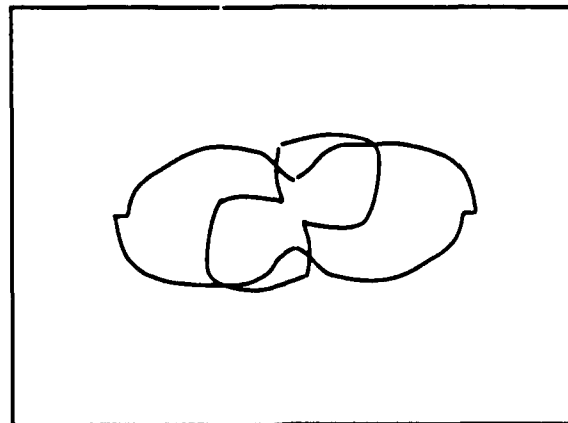
T300/976 [0₄/45₂/-45₄/45₂/0₄]



Mass = 0.16 kg Velocity = 2.51 m/s



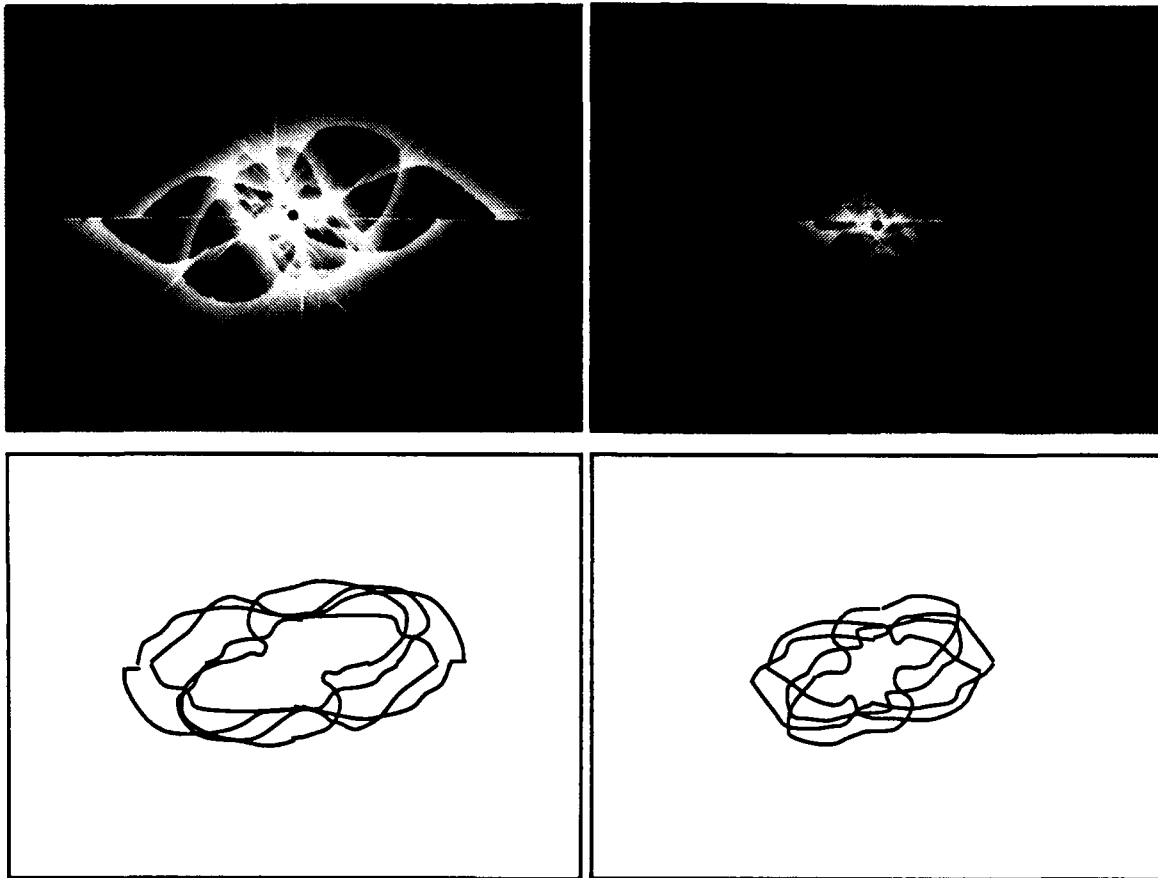
Mass = 0.16 kg Velocity = 3.90 m/s



Mass = 0.16 kg Velocity = 5.90 m/s

Figure 6.18: The predicted delamination sizes of [0₄/45₂/ - 45₄/45₂/0₄] composites corresponding to the impact condition given in Figure 6.16.

T300/976
[0₄/45₄/-45₄/90₄/-45₄/45₄/0₄]



Mass = 0.16 kg
Velocity = 7.8 m/s

Mass = 0.16 kg
Velocity = 5.2 m/s

Figure 6.19: Comparison of delamination sizes and shapes of [0₄/45₄/ - 45₄/90₂]_S composites between X-Radiographs taken from the tested specimen and predictions.

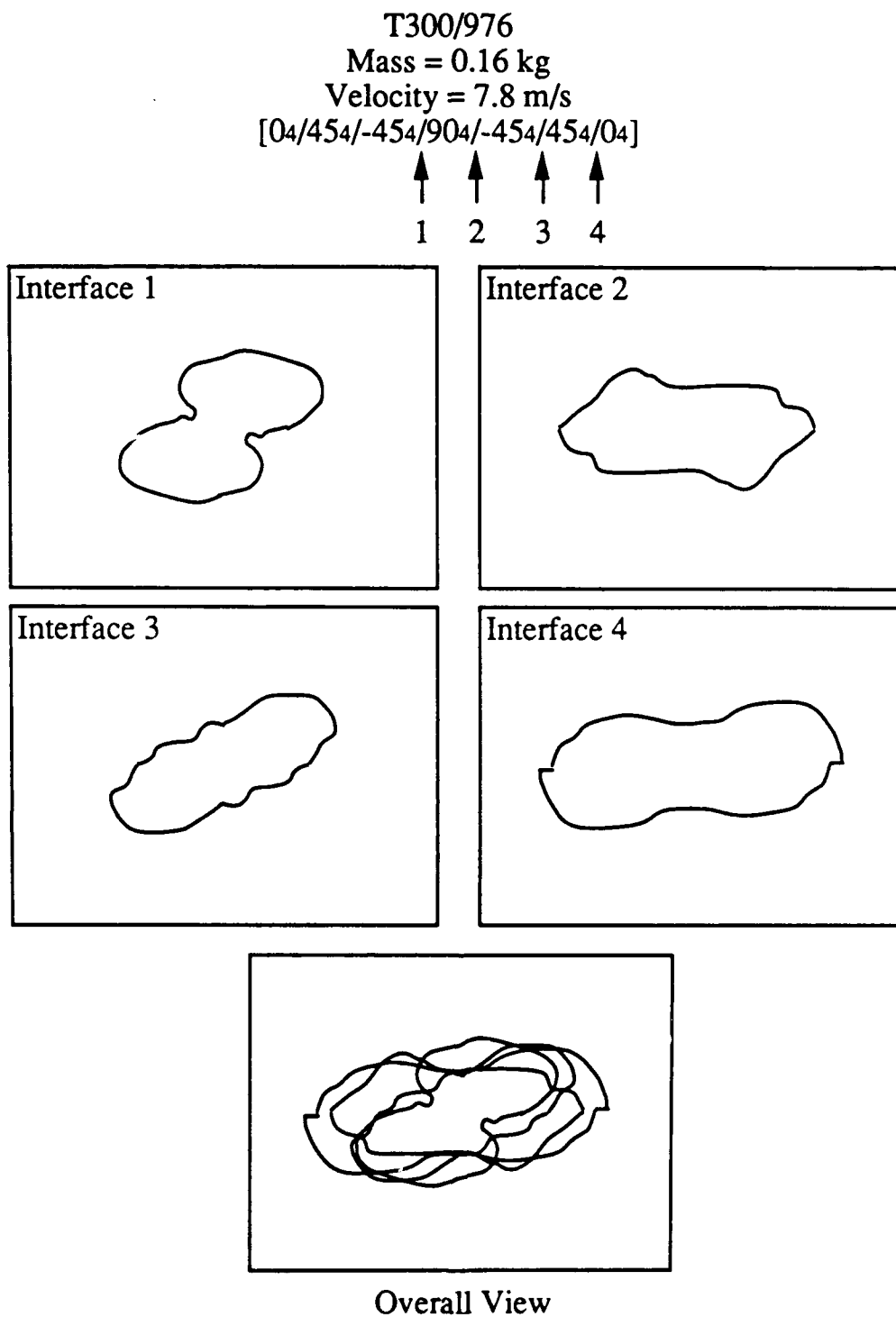


Figure 6.20: Predicted delamination sizes and shapes of [0₄/45₄/ - 45₄/90₂]_S composites at different interfaces.

computer code was developed. Overall, the predictions based on the model agreed with the test data very consistently. Based on the study, the following remarks can be made:

1. An impact velocity threshold exists for Graphite/Epoxy laminated composites below which no delamination occurs, but above which significant damage can be produced.
2. Matrix cracking is the initial failure mode.
3. Matrix cracking in composites can lead to interface delaminations.
4. The occurrence of the critical matrix cracks is primarily due to the interlaminar transverse shear stress and transverse in-plane stress of the concerned layer.
5. Delamination growth is governed by the interlaminar longitudinal shear stress and transverse in-plane stress in the layer below the delaminated interface and the interlaminar transverse shear stress in the upper layers directly above the interface.

Chapter 7

COMPUTER CODE

During the investigation, a computer code, designated as "3DIMPACT," was developed based on the proposed analysis. The user-friendly code can be used to provide the following information:

1. Stresses and strains as a function of time up to the initial damage during impact.
2. The contact force as a function of time.
3. The impact velocity threshold corresponding to the initial impact damage.
4. The extent of final delaminations after impact.

The material properties, laminate ply orientation, thickness, and the mass of the impactor can be input arbitrarily. In Appendix D, the user-friendly INPUT-OUTPUT of the "3DIMPACT" code is presented.

LIST OF PUBLICATIONS RESULTING FROM THE ARO SUPPORT

- 1) Chang, F. K., H. Y. Choi and S. T. Jeng, "Characterization of Impact Damage in Laminated Composites," *SAMPE Journal*, Vol. 26, No. 1, January/February 1990, pp. 18-26.
- 2) Chang, F. K., H. Y. Choi and S. T. Jeng, "Study on Impact Damage in Laminated Composites," *J. of Mechanics of Materials*, (to appear).
- 3) Chang, F. K., H. Y. Choi and R. J. Downs, "A New Approach Toward Understanding Impact Damage Mechanisms and Mechanics of Laminated Composites, Part I - Experiment," *J. of Composite Materials*, (accepted).
- 4) Choi, H. Y. and F. K. Chang, "A New Approach Toward Understanding Impact Damage Mechanisms and Mechanics of Laminated Composites, Part II - Analysis," *J. of Composite Materials*, (accepted).
- 5) Choi, H. Y., H. S. Wang, and F. K. Chang, "Effect of Laminated Configuration and Impactor's Mass on the Initial Impact Damage of Composite Plates Due to Line-Loading Impact," *J. of Composite Materials*, (accepted).
- 6) Choi, H. Y. and F. K. Chang, "A Model for Predicting Impact Damage of Graphite/Epoxy Laminated Composites Due to Point-Nose Impact," *J. of Composite Materials*, (submitted).
- 7) Choi, H. Y. and F. K. Chang, "Impact Resistance of Laminated Composites to Low-Velocity Impact," *J. of Polymer Composites*, (to appear).
- 8) Chang, F. K., H. Y. Choi and H. S. Wang, "Damage of Laminated Composites Due to Low Velocity Impact," 31st AIAA/ASME/ASCE/AHS/ASC Structures, Structural Dynamics and Materials (SDM) Conference, April 2-4, 1990, Long Beach, CA.

LIST OF ALL PARTICIPATING SCIENTIFIC PERSONNEL

1. Fu-Kuo Chang (P.I.), Assistant Professor of Aeronautics and Astronautics.
2. Hyung-Yun Choi (Graduate Student): received his Ph.D. degree in September 1990 based on his work on the project.
3. Hong-Sheng Wang (Visiting Scholar)
4. R. J. Downs (Graduate Student)

REFERENCES

- [1] Chai, H., Babcock, C. D. and Knauss, W., "One-Dimensional Modeling of Failure in Laminated Plates by Delamination Buckling," *Int'l. J. of Solids and Structures*, Vol. 17, (1981), pp. 1069-1083.
- [2] Whitcomb, J. D., "Finite Element Analysis of Instability Related Delamination Growth," *J. of Composite Materials*, Vol. 15, (1981), pp. 403-426.
- [3] Chang, F. K. and Kutlu, Z., "Delamination Effects on Composite Shells," *Recent Advances in Macro- and Micro-mechanics of Composite Structures*, ASME AD Vol. 13, (D. Hui and J. R. Vinson, eds.), (1988), pp. 71-77.
- [4] Chang, F. K. and Kutlu, Z., "Collapse Analysis of Composite Panels with Multiple Delaminations," *Proceedings of the AIAA/ASME/SAE 30th Structures, Structural Dynamics and Materials Conference (SMD)*, Mobile, AL, (1989), pp. 989-1011.
- [5] Rothschilds, R. J., Gillespie, J. W., Jr. and Carlsson, L. A., "Instability-Related Delamination Growth in Thermoset and Thermoplastic Composites," *Composite Materials: Testing and Design (8th Conference)*, ASTM STP 972, (J. D. Whitcomb, ed.), American Society for Testing and Materials, Philadelphia, PA, (1988), pp. 161-179.
- [6] Wang, S. S., "An Analysis of Delamination in Angle-ply Fiber-Reinforced Composites," *J. of Applied Mechanics*, Vol. 17, (1980), pp. 64-70.

- [7] Sun, C. T. and Jen, K. C., "On the Effect of Matrix Cracks on Laminate Strength," J. of Reinforced Plastics and Composites, Vol. 16, (1987), pp. 208-222.
- [8] Aronsson, C. and Bäcklund, J., "Tensile Fracture of Laminates with Cracks," J. of Composite Materials, Vol. 20, (1986), pp. 287-307.
- [9] Manders, P. W., Chou, T., Jones, F. R. and Rock, J. W., "Statistical Analysis of Multiple Fracture in 0°/90°/0° Glass Fiber/Epoxy Resin Laminates," J. of Material Science, Vol. 18, (1983), pp. 2876-2889.
- [10] Parvizi, A. and Bailey, J. E., "On Multiple Transverse Cracking in Glass Fibre Epoxy Cross-Ply Laminates," J. of Material Science, Vol. 13, (1978), pp. 2131-2136.
- [11] Parvizi, A., Garrett, K. W. and Bailey, J. E., "Constrained Cracking in Glass Fibre-Reinforced Epoxy Cross-Ply Laminates," J. of Material Science, Vol. 13, (1978), pp. 195-201.
- [12] Allen, D. H., Harris, C. E. Groves, S. E. and Norvell, R. G., "Characterization of Stiffness Loss in Crossply Laminates with Curved Matrix Cracks," J. of Material Science, Vol. 22, (1988), pp. 71-80.
- [13] Wu, H. T. Ph.D Dissertation, Aero. and Astro. Department, Stanford University (1987).
- [14] Wu, H. T. and Springer, G. S., "Measurements of Matrix Cracking and Delamination Caused by Impact on Composite Plates," J. of Composite Materials, Vol. 22, (1988), pp. 518-532.
- [15] Wu, H. T. and Springer, G. S., "Impact Induced Stresses, Strains and Delaminations in Composite Plates," J. of Composite Materials, Vol. 22, (1988), pp. 533-560.

- [16] Wu, H. T. and Chang, F. K., "Transient Dynamic Analysis of Laminated Composite Plates Subjected to Transverse Impact," *J. of Computers and Structures*, Vol. 31, (1989), pp. 453-466.
- [17] Ross, C. A. Malvern, L. E., Sierakowski, R. L. and Taketa, N., "Finite-Element Analysis of Interlaminar Shear Stress Due to Local Impact," *Recent Advances in Comp. in the United States and Japan*, ASTM STP 864, (J. P. Vinson and M. Taya, Eds.) American Society for Testing and Materials, Philadelphia, PA, (1985), pp. 335-367.
- [18] Aggour, H. and Sun, C. T., "Finite Element Analysis of a Laminated Composite Plate Subjected to Circularly Distributed Central Impact Loading," *J. of Computers and Structures*, Vol. 28, (1988), pp. 729-736.
- [19] Poe, Jr., C. C., "Simulated Impact Damage in a Thick Graphite /Epoxy Laminate using Spherical Indenters," NASA TM-100539, January, (1988).
- [20] Kim, B. S. and Moon, F. C., "Transient Wave Propagation in Composite Plates Due to Impact," *Proceedings of the AIAA/ASME 18th Structures, Structural Dynamics and Materials Conference*, Vol. B, San Diego, CA, March (1977), pp. 43-50.
- [21] Kubo, J. T. and Nelson, R. B., "Analysis of Impact Stresses in Composite Plates," American Society for Testing and Materials, Special Technical Publication 568, Philadelphia, Pa, (1975), pp. 228-244.
- [22] Sun, C. T. and Yang, S. H., "Contact Law and Impact Responses of Laminated Composites," NASA CR-159884, National Aeronautical and Space Administration, Washington, D.C., (1980).
- [23] Tan, T. M. and Sun, C. T., "Use of Statistical Indentation Laws in the Impact Analysis of Laminated Composite Plates," *J. of Applied Mechanics*, Vol. 52, March (1985), pp. 6-12.

- [24] Bostaph, G. M. and Elber, W., "Static Indentation Tests of Composite plates for Impact Susceptibility Evaluation," A research report, NASA-Langley Research Center, Hampton, VA
- [25] Sjöblom, P. O., Hartness, J. T. and Cordell, T. M., "On Low-Velocity Impact Testing of Composite Materials," *J. of Computers and Structures*, Vol. 22, (1988), pp. 30-52.
- [26] Lal, K. M., "Low Velocity Transverse Impact Behavior of 8-ply Graphite-Epoxy Laminates," *J. of Reinforced Plastics and Composites*, Vol. 2, Oct. (1983), pp. 216-225.
- [27] Greszczuk, L. B., "Foreign Objects Damage to Composites," ASTM STP 568, (1973).
- [28] Chamis, C. C. and Sinclair, J. H., "Impact Resistance of Fiber Composites: Energy-Absorbing Mechanisms and Environmental Effects," *Recent Advances in Composites in the United States and Japan*, ASTM STP 864, (Vinson and Taya, Eds.), (1983), pp. 326-345.
- [29] Chamis, C. C., Hanson, M. P. and Serafini, T. T., "Designing for Impact Resistance with Unidirectional Fiber Composites," NASA TND-6463, National Aeronautical and Space Administration, Washington, D.C., (1971).
- [30] Gosse, J. H. and Mori, P. B. Y., "Impact Damage Characterization of Graphite/Epoxy Laminates," *Proceedings of the Third Technical Conference of the American Society for Composites*, Seattle, WA, (1988), pp. 334-353.
- [31] Joshi, S. P., "Impact-Induced Damage Initiation Analysis: An Experimental Study," *Proceedings of the Third Technical Conference of the American Society for Composites*, Seattle, WA, (1988), pp. 325-333.
- [32] Sun, C. T. and Rechak, S., "Effect of Adhesive Layers on Impact Damage in Composite Laminates," *Composite Materials: Testing and Design (Eighth Conf.)*, ASTM STP 972 (J. D. Whitcomb, Ed.), American Society for Testing and Materials, Philadelphia, PA, (1988), pp. 97-123.

- [33] Clark, G., "Modelling of Impact Damage in Composite Laminate," *Composites*, Vol. 20, (1988), pp. 209-214.
- [34] Reed, P. E. and Turner, S., "Flexed Plate Impact, Part 7. Low Energy and Excess Energy Impacts on Carbon Fiber-Reinforced Polymer Composites," *Composites*, Vol. 19, (1988), pp. 193-203.
- [35] Liu, D. and Malvern, L. E., "Matrix Cracking in Impacted Glass/Epoxy Plates," *J. of Computers and Structures*, Vol. 21, (1987), pp. 594-609.
- [36] Gu, Z. L. and Sun, C. T., "Prediction of Impact Damage Region in SMC Composites," *Composite Structures*, Vol. 7, (1987), pp. 179-190.
- [37] Sun, C. T. and Chattopadhyay, S., "Dynamic Response of Anisotropic Laminated Plates Under Initial Stress to Impact of a Mass," *J. of Applied Mechanics*, Vol. 42, (1975), pp. 693-698.
- [38] Chen, J. K. and Sun, C. T., "Analysis of Impact Response of Buckled Composite Laminates," *Composite Structures*, Vol. 3, (1985), pp. 97-118.
- [39] Chen, J. K. and Sun, C. T., "On the Impact of Initially Stressed Composite Laminates," *J. of Composite Materials*, Vol. 19, Nov. (1985), pp. 490-504.
- [40] Stori, A. A. and Magnus, E., "An Evaluation of the Impact Properties of Carbon Fiber Reinforced Composites with Various Matrix Materials," *J. of Composite Structures*, Vol. 2, (1983), pp. 332-248.
- [41] Malvern, L. E., Sierakowski, R. L., Ross, L. A. and Cristescu, N., "Impact Failure Mechanisms in Fiber-Reinforced Composite Plates," *High Velocity Deformation of Solids*, (Kawata and Shiori, Eds.), Springer-Verlag, Berlin, (1978), pp. 120-130.
- [42] Jones, S., Paul, J., Tay, T. E. and Williams, J. F., "Assessment of the Effect of Impact Damage in Composites: Some Problems and Answers," *Composite Structures*, Vol. 10, (1988), pp. 51-73.

- [43] Sun, C. T. and Grady, J. E., "Dynamic Delamination Fracture Toughness of a Graphite/Epoxy Laminate Under Impact," *Composite Science and Technology*, Vol. 31, (1988), pp. 55-72.
- [44] Guynn, E. G., and O'Brien, T. K., "The Influence of Lay-up and Thickness on Composite Impact Damage and Compression Strength," *Proceedings of AIAA/ASME/ASCE/AHS, 26th SDM Conference*, Orlando, FL, (1985), pp. 187-196.
- [45] Elber, W., "Failure Mechanics in Low-Velocity Impacts on Thin Composite Plates," *NASA Technical Paper TP 2152*, NASA-Langley Research Center, Hampton, VA., (1983).
- [46] Joshi, S. P. and Sun, C. T., "Impact-Induced Fracture in Quasi-Isotropic Laminate," *J. of Composite Technology and Research*, Vol. 19, (1986), pp. 40-46.
- [47] Cantwell, W. J. and Morton, J., "Geometrical Effects in the Low Velocity Impact Response of CFRP," *Composite Structures*, Vol. 12, (1989), pp. 39-59.
- [48] Chang, F. K., Choi, H. Y. and Downs, R. J., "A New Approach Toward Understanding Damage Mechanisms and Mechanics of Laminated Composites Due to Low-Velocity Impact, Part I-Experiments," *J. of Composite Materials*, (accepted).
- [49] Chang, F. K., Choi, H. T. and Wu, H. Y. T., "A New Approach Toward Understanding Damage Mechanisms and Mechanics of Laminated Composites Due to Low-velocity Impact, Part II-Analysis," *J. of Composite Materials*, (accepted).
- [50] Choi, H. Y., Wang, H. S. and Chang, F. K., "Effect of Laminate Configuration and Impactor's Mass on the Initial Impact Damage of Composite Plates Due to Line-Loading Impact," *J. of Composite Materials*, (accepted).

- [51] Chang, F. K., Choi, H. Y. and Wang, H. S., "Damage of Laminated Composites Due to Low Velocity Impact," 31st AIAA/ASME/ASCE/AHS/ASC Structures, Structural Dynamics and Materials (SDM) Conference, April 2-4, (1990), Long Beach, CA.
- [52] Choi, H. Y. and Chang, F. K., "A Model for Predicting Impact Damage of Graphite/Epoxy Laminated Composites Due to Point-Nose Impact," J. of Composite Materials, (accepted).
- [53] Freeman, S. M., "Characterization of Laminar and Interlaminar Damage in Graphite/Epoxy Composites by the Deply Technique," Composite Materials: Testing and Design (Sixth Conference), ASTM STP 787, I. M. Daniel, ed., American Society for Testing and Materials, (1982), pp. 50-62.
- [54] Hashin, Z., "Failure Criteria for Unidirectional Fiber Composites," J. of Applied Mechanics, Vol. 47, (1980), pp. 329-334.
- [55] Griffin, O. H. Jr. and Roberts, J. C., "Numerical/Experimental Correlation of Three-Dimensional Thermal Stress Distributions in Graphite/Epoxy Laminates," J. of Composite Materials, Vol. 17, (1988), pp. 539-548.
- [56] Griffin, O. H. Jr., "Three-Dimensional Thermal Stresses in Angle-Ply Composite Laminates," J. of Composite Materials, Vol. 22, (1988), pp. 53-70.
- [57] Griffin, O. H. Jr., "Three-Dimensional Curing Stresses in Symmetric Cross-Ply Laminates with Temperature-Dependent Properties," J. of Composite Materials, Vol. 17, (1983), pp. 449-463.
- [58] Wu, C. H. and Tauchert, T. R., "Thermoelastic Analysis of Laminated Plates. 1: Symmetric Specially Orthotropic Laminates," J. of Thermal Stresses, Vol. 3, (1980), pp. 247-259.
- [59] Hughes, T. J. R., The Finite Element Method Linear Static and Dynamic Finite Element Analysis, Prentice-Hall, Inc., Englewood Cliffs, New Jersey, (1987).

- [60] Bathe, K. J. and Wilson, E. L., *Numerical Methods in Finite Element Analysis*, Prentice-Hall, Inc., Englewood Cliffs, New Jersey, (1976).
- [61] Goldsmith, W., *Impact, the Theory and Physical Behavior of Colliding Solids*, Edward Arnold Ltd., London, (1960), pp. 88.
- [62] Chang, F. K. and Lessard, L. B., "Damage Tolerance of Laminated Composites Containing an Open Hole and Subjected to Compressive Loading: Part I-Analysis," *J. of Composite Materials*, (accepted).
- [63] Chang, F. K. and Chen, M., "The In Situ Ply Shear Strength Distributions in Graphite/Epoxy Laminated Composites," *J. of Composite Materials*, Vol. 21, (1987), pp. 708-732.
- [64] Flaggs, D. L. and Kural, M. H., "Experimental Determination of In Situ Transverse Laminar Strength in Graphite/Epoxy Laminate," *J. of Composite Materials*, Vol. 16, (1982), pp. 103-116.
- [65] Peter, P. W. M., "The Strength Distribution of 90° plies in 0/90/0 Graphite-Epoxy Laminates," *J. of Composite Materials*, Vol. 18, (1984), pp. 545-556.
- [66] Chang, F. K. and Z. Kutlu, "Strength and Response of Cylindrical Composite Shells Subjected to Out-of-plane Loading," *J. of Composite Materials*, Vol. 23, No. 1, (1989), pp. 11-31.
- [67] Chang, F. K. and Chang, K. Y., "A Progressive Damage Model for Laminated Composites Containing Stress Concentrations," *J. of Composite Materials*, Vol. 21, (1987), pp. 834-855.
- [68] Pagano, N. J., "Exact Solutions for Composite Laminate in Cylindrical Bending," *J. of Composite Materials*, Vol. 3, (1969), pp. 398-411.
- [69] Warburton, G. B., *The Dynamical Behaviour of Structures*, Pergamon Press, (1976).

- [70] Zienkiewicz, O. C., The Finite Element Method, 3rd ed., McGraw-Hill, New York, (1977).
- [71] Hertz, O., "Über die Berührung fester elastischer Körper," J. für die Reine und Angewandte Mathematik, 92, pp. 156-171, (1982).
- [72] Williams, J. G., "On the Calculations of Energy Release Rates for Cracked Laminates," International J. of Fracture, Vol. 36, (1988), pp. 101-119.
- [73] Liu, S., Kutlu, Z. and Chang, F. K., "Matrix Cracking-Induced Delamination Propagation in Laminated Composites Subjected to Quasi-Static Transversely Concentrated Loading," J. of Composite Materials, (submitted).
- [74] Sun, C. T. and Manoharan, M. G., "Growth of Delamination Cracks Due to Bending in a $[90_5/0_5/90_5]$ Laminate," Composite Science and Technology, Vol. 34, (1989), pp. 365-377.
- [75] Cook, N. H. and Rabinowich, E., Physical Measurement and Analysis. Addison-Wesley Publishing Co., Reading, Mass., (1963)

Appendix A

THE STIFFNESS MATRIX

On-axis stress-strain relationship for a lamina, is given by:

$$\begin{Bmatrix} \sigma_{xx} \\ \sigma_{yy} \\ \sigma_{zz} \\ \sigma_{yz} \\ \sigma_{xz} \\ \sigma_{xy} \end{Bmatrix} = \begin{bmatrix} Q_{11} & Q_{12} & Q_{13} & 0 & 0 & 0 \\ Q_{21} & Q_{22} & Q_{23} & 0 & 0 & 0 \\ Q_{31} & Q_{32} & Q_{33} & 0 & 0 & 0 \\ 0 & 0 & 0 & Q_{44} & 0 & 0 \\ 0 & 0 & 0 & 0 & Q_{55} & 0 \\ 0 & 0 & 0 & 0 & 0 & Q_{66} \end{bmatrix} \begin{Bmatrix} \epsilon_{xx} \\ \epsilon_{yy} \\ \epsilon_{zz} \\ \gamma_{yz} \\ \gamma_{xz} \\ \gamma_{xy} \end{Bmatrix} \quad (\text{A.1})$$

where

$$\begin{aligned} Q_{11} &= E_{xx}(1 - \nu_{yz}\nu_{zy})/\Delta \\ Q_{22} &= E_{yy}(1 - \nu_{zx}\nu_{xz})/\Delta \\ Q_{33} &= E_{zz}(1 - \nu_{xy}\nu_{yx})/\Delta \\ Q_{44} &= G_{yz} \\ Q_{55} &= G_{xz} \\ Q_{66} &= G_{xy} \\ Q_{12} &= E_{xx}(\nu_{yx} + \nu_{zx}\nu_{yz})/\Delta \\ Q_{13} &= E_{xx}(\nu_{zx} + \nu_{yx}\nu_{zy})/\Delta \\ Q_{23} &= E_{yy}(\nu_{zy} + \nu_{xy}\nu_{xz})/\Delta \\ \Delta &= 1 - \nu_{xy}\nu_{yx} - \nu_{yz}\nu_{zy} - \nu_{zx}\nu_{xz} - 2\nu_{yx}\nu_{zy}\nu_{xz} \end{aligned} \quad (\text{A.2})$$

The off-axis material property matrix is then given by:

$$\begin{Bmatrix} \sigma_1 \\ \sigma_2 \\ \sigma_3 \\ \sigma_4 \\ \sigma_5 \\ \sigma_6 \end{Bmatrix} = \begin{bmatrix} \bar{Q}_{11} & \bar{Q}_{12} & \bar{Q}_{13} & 0 & 0 & 2\bar{Q}_{16} \\ \bar{Q}_{21} & \bar{Q}_{22} & \bar{Q}_{23} & 0 & 0 & 2\bar{Q}_{26} \\ \bar{Q}_{31} & \bar{Q}_{32} & \bar{Q}_{33} & 0 & 0 & 2\bar{Q}_{36} \\ 0 & 0 & 0 & 2\bar{Q}_{44} & 2\bar{Q}_{45} & 0 \\ 0 & 0 & 0 & 2\bar{Q}_{45} & 2\bar{Q}_{55} & 0 \\ \bar{Q}_{16} & \bar{Q}_{26} & \bar{Q}_{36} & 0 & 0 & 2\bar{Q}_{66} \end{bmatrix} \begin{Bmatrix} \epsilon_1 \\ \epsilon_2 \\ \epsilon_3 \\ \epsilon_4 \\ \epsilon_5 \\ \epsilon_6 \end{Bmatrix} \quad (\text{A.3})$$

where

$$\begin{aligned} \bar{Q}_{11} &= Q_{11}m^4 + 2(Q_{12} + 2Q_{66})m^2n^2 + Q_{22}n^4 \\ \bar{Q}_{12} &= (Q_{11} + Q_{22} - 4Q_{66})m^2n^2 + Q_{12}(m^4 + n^4) \\ \bar{Q}_{13} &= Q_{13}m^2 + Q_{23}n^2 \\ \bar{Q}_{16} &= -mn^3Q_{22} + m^3nQ_{11} - mn(m^2 - n^2)(Q_{12} + 2Q_{66}) \\ \bar{Q}_{22} &= Q_{11}n^4 + 2(Q_{12} + 2Q_{66})m^2n^2 + Q_{22}m^4 \\ \bar{Q}_{23} &= n^2Q_{13} + m^3Q_{23} \\ \bar{Q}_{33} &= Q_{33} \\ \bar{Q}_{26} &= -m^3nQ_{22} + mn^3Q_{11} + mn(m^2 - n^2)(Q_{12} + 2Q_{66}) \\ \bar{Q}_{36} &= (Q_{13} - Q_{23})mn \\ \bar{Q}_{44} &= Q_{44}m^2 + Q_{55}n^2 \\ \bar{Q}_{45} &= (Q_{55} - Q_{44})mn \\ \bar{Q}_{55} &= Q_{55}m^2 + Q_{44}n^2 \\ \bar{Q}_{66} &= (Q_{11} + Q_{22} - 2Q_{12})m^2n^2 + Q_{66}(m^2 - n^2)^2 \\ m &= \cos \theta \\ n &= \sin \theta \end{aligned} \quad (\text{A.4})$$

Applying plane strain condition such that

$$\epsilon_2 = \epsilon_4 = \epsilon_6 = 0 \quad (\text{A.5})$$

$$\begin{Bmatrix} \sigma_1 \\ \sigma_3 \\ \sigma_5 \end{Bmatrix} = \begin{bmatrix} \bar{Q}_{11} & \bar{Q}_{13} & 0 \\ \bar{Q}_{13} & \bar{Q}_{33} & 0 \\ 0 & 0 & 2\bar{Q}_{55} \end{bmatrix} \begin{Bmatrix} \epsilon_1 \\ \epsilon_3 \\ \epsilon_5 \end{Bmatrix} \quad (\text{A.6})$$

Appendix B

DETERMINATION OF THE DISPLACEMENT OF IMPACTOR

From the known displacement of impactor d_1 at time t , the displacement d_2 at time $t + \Delta t$ can be calculated as

$$d_2 = d_1 + \int_t^{t+\Delta t} v(\tau) d\tau \quad (\text{B.1})$$

where the $v(\tau)$ is velocity of impactor. From the known velocity v_1 at time t , the velocity at time τ is calculated as

$$v(\tau) = v_1 - \frac{1}{m} \int_t^{\tau} f(\tau) d\tau \quad (\text{B.2})$$

where the $f(\tau)$ is contact force between impactor and plate. The contact force at time t is given and equal to f_1 . Assuming the contact force is increasing or decreasing linearly between time t and $t + \Delta t$, the contact force f_2 at time $t + \Delta t$ can be expressed as

$$f(\tau) = f_1 + \frac{(f_2 - f_1)}{\Delta t}(\tau - t) : \quad t \leq \tau \leq t + \Delta t \quad (\text{B.3})$$

Eqs. (B.2) and (B.3) give

$$\begin{aligned}
v(\tau) &= v_1 - \frac{1}{m} \int_t^\tau \left\{ \left[f_1 - \frac{(f_2 - f_1)t}{\Delta t} \right] + \frac{(f_2 - f_1)}{\Delta t} \tau \right\} d\tau \\
&= v_1 - \frac{f_1}{m}(\tau - t) + \frac{(f_2 - f_1)t}{m\Delta t}(\tau - t) \\
&\quad - \frac{(f_2 - f_1)}{2m\Delta t}(\tau^2 - t^2); \quad t \leq \tau \leq t + \Delta t
\end{aligned} \tag{B.4}$$

At time $t + \Delta t$, the velocity v_2 becomes

$$v_2 = v_1 - \frac{(f_1 + f_2)}{2m} \Delta t \tag{B.5}$$

By combining Eqs. (B.1) and (B.4), the displacement of impactor d_2 at time $t + \Delta t$ is obtained as follows;

$$\begin{aligned}
d_2 &= d_1 + \frac{1}{m} \int_t^{t+\Delta t} \left[v_1 - f_1(\tau - t) + \frac{(f_2 - f_1)t}{\Delta t}(\tau - t) \right. \\
&\quad \left. - \frac{(f_2 - f_1)}{2\Delta t}(\tau^2 - t^2) \right] d\tau \\
&= d_1 + \frac{1}{m} \int_t^{t+\Delta t} \left\{ \left[v_1 + f_1 t - \frac{(f_2 - f_1)t^2}{2\Delta t} \right] \right. \\
&\quad \left. + \left[-f_1 + \frac{(f_2 - f_1)t}{\Delta t} \right] \tau - \left[\frac{(f_2 - f_1)}{2\Delta t} \right] \tau^2 \right\} d\tau \\
&= \left[d_1 + v_1 \Delta t + \frac{f_1 t \Delta t}{m} - \frac{(f_2 - f_1)t^2}{2m} \right] \\
&\quad + \left[-\frac{f_1}{m} + \frac{(f_2 - f_1)t}{m\Delta t} \right] \frac{(2t\Delta t + \Delta t^2)}{2} \\
&\quad - \left[\frac{(f_2 - f_1)}{2m\Delta t} \right] \frac{(3t^2\Delta t + 3t\Delta t^2 + \Delta t^3)}{3} \\
&= d_1 + v_1 \Delta t - \frac{(2f_1 + f_2)\Delta t^2}{6m}
\end{aligned} \tag{B.6}$$

Appendix C

DATA OF POINT-LOADING IMPACT EXPERIMENTS

T300/976 [45₄/-45₈/45₄]

↑ ↑
2 1

Mass (kg)	Test Velocity (m/s)	Delamination at the interface 1 (cm)		Delamination at the interface 2 (cm)	
		Length	Width	Length	Width
0.16	2.31	0.0	0.0	0.0	0.0
0.16	3.04	0.0	0.0	0.0	0.0
0.16	3.15	0.0	0.0	0.0	0.0
0.16	3.49	1.6	0.5	0.0	0.0
0.16	3.63	1.6	0.5	0.0	0.0
0.16	4.06	1.7	0.5	0.0	0.0
0.16	4.15	1.9	0.5	0.0	0.0
0.16	4.24	1.7	0.5	0.0	0.0
0.16	4.87	2.4	0.9	0.0	0.0
0.16	4.88	3.0	1.5	0.0	0.0
0.16	5.89	3.5	1.6	0.0	0.0
0.16	7.26	5.0	2.4	1.9	1.0
0.16	9.02	5.7	2.5	2.0	1.1

Table C.1: Measured delamination sizes of T300/976 [45₄/ - 45₈/45₄].

T300/976 [0₃/90₃/0₃/90₃/0₃]

↑ ↑ ↑
3 2 1

Mass (kg)	Test Velocity (m/s)	Delamination at the interface 1 (cm)		Delamination at the interface 2 (cm)		Delamination at the interface 3 (cm)	
		Length	Width	Length	Width	Length	Width
0.16	2.73	0.0	0.0	0.0	0.0	0.0	0.0
0.16	3.16	0.9	0.4	0.0	0.0	0.0	0.0
0.16	3.22	0.8	0.3	0.0	0.0	0.0	0.0
0.16	3.34	1.0	1.3	0.0	0.0	0.0	0.0
0.16	3.59	0.8	0.4	0.0	0.0	0.0	0.0
0.16	3.60	1.1	0.5	0.0	0.0	0.0	0.0
0.16	3.68	1.0	0.4	0.0	0.0	0.0	0.0
0.16	3.93	1.0	0.4	0.0	0.0	0.0	0.0
0.16	4.00	2.5	0.8	1.6	0.7	1.2	0.5
0.16	4.03	1.9	0.6	1.1	0.8	0.9	0.5
0.16	4.12	2.3	0.8	1.5	0.7	1.1	0.5
0.16	4.18	1.0	0.3	0.0	0.0	0.0	0.0
0.16	4.72	2.2	0.8	1.4	0.8	1.1	0.5
0.16	5.35	3.4	1.1	1.9	1.1	1.5	0.7
0.16	6.70	3.6	1.1	1.9	1.2	1.6	0.9

Table C.2: Measured delamination sizes of T300/976 [0₃/90₃/0₃/90₃/0₃].

T300/976 [0₄/45₂/-45₄/45₂/0₄]

↑ ↑ ↑
3 2 1

Mass (kg)	Test Velocity (m/s)	Delamination at the interface 1 (cm)		Delamination at the interface 2 (cm)		Delamination at the interface 3 (cm)	
		Length	Width	Length	Width	Length	Width
0.16	1.78	0.0	0.0	0.0	0.0	0.0	0.0
0.16	2.25	0.0	0.0	0.0	0.0	0.0	0.0
0.16	2.51	0.0	0.0	0.0	0.0	0.0	0.0
0.16	2.63	1.0	0.1	0.0	0.0	0.0	0.0
0.16	2.64	1.0	0.1	0.0	0.0	0.0	0.0
0.16	2.86	1.8	0.2	0.0	0.0	0.0	0.0
0.16	2.92	1.5	0.2	0.0	0.0	0.0	0.0
0.16	3.33	2.2	0.3	0.0	0.0	0.0	0.0
0.16	3.36	2.0	0.4	0.0	0.0	0.0	0.0
0.16	3.37	2.5	0.5	0.0	0.0	0.0	0.0
0.16	3.69	2.5	0.4	0.0	0.0	0.0	0.0
0.16	3.90	3.1	0.5	1.5	0.4	1.5	0.4
0.16	4.34	3.3	0.8	1.5	0.5	1.5	0.5
0.16	5.90	4.3	1.1	2.3	0.8	2.1	0.7

Table C.3: Measured delamination sizes of T300/976 [0₄/45₂/ - 45₄/45₂/0₄].

Appendix D

USER-FRIENDLY INPUT-OUTPUT OF "3DIMPACT" CODE

```

*****
**
** 333 DDD IIII MM MM PPPPPP A CCCC TTTTTT **
** 33 D D II MM MM PP PP AAA CC CC TT **
** 33 D D II MMM MM PP PP AAAAA CC TT **
** 3333 D D II MM MM MM PPPPPP AA AA CC TT **
** 33 D D II MM MM PP AAAAAAAA CC TT **
** 33 D D II MM MM PP AA AA CC CC TT **
** 333 DDD IIII MMM MMM PPPP AA AA CCCC TT **
**
*****

```

```

*****
**
**      -- << IMPACT DAMAGE OF COMPOSITE PLATES >> --
**
** THE PURPOSE OF THIS PROGRAM IS TO PREDICT THE
** DAMAGE IN COMPOSITE PLATES SUBJECTED TO LOW-VELOCITY
** FOREIGN OBJECT IMPACT.
**
** HYUNG YUN CHOI & FU-KUO CHANG
** DEPARTMENT OF AERONAUTICS AND ASTRONAUTICS
** STANFORD UNIVERSITY
** STANFORD, CA 94305
** (415) 723-3466
**
** CREATED: JUNE. 1989
** MODIFIED: NOVEMBER. 1990
**
** THIS PROGRAM FOLLOWS THE NUMERICAL STRUCTURE
** OF THE "IMPACT" BY H-Y T. WU & G. S. SPRINGER
**
** © COPYRIGHT 1990, H.Y. CHOI & F.K. CHANG
**
*****

```

```

*****
**
** IN ORDER TO MAKE THE INPUT EASIER, YOU MAY SAVE THE
** INPUT PARAMETERS IN THE DATA FILE "INPUT.DAT".
** THE PROGRAM WILL INPUT THE NUMBERS AUTOMATICALLY.
**
** IF YOU ARE THE FIRST TIME USER, YOU SHOULD USE THE
** INTERACTIVE PROCEDURE TO INPUT YOUR DATA.
**
** WHEN YOU ARE USING THE INTERACTIVE PROCEDURE, THE PROGRAM
** WILL GENERATE A DATA FILE NAMED "INPUT.DAT" ACCORDING
** TO YOUR INTERACTIVE INPUT.
**
** ONCE THE INPUT DATA FILE "INPUT.DAT" HAS BEEN CREATED,
** YOU MAY INPUT THE DATA EITHER BY THE INTERACTIVE
** PROCEDURE OR DIRECTLY FROM THE DATA FILE.
**
*****

```

```

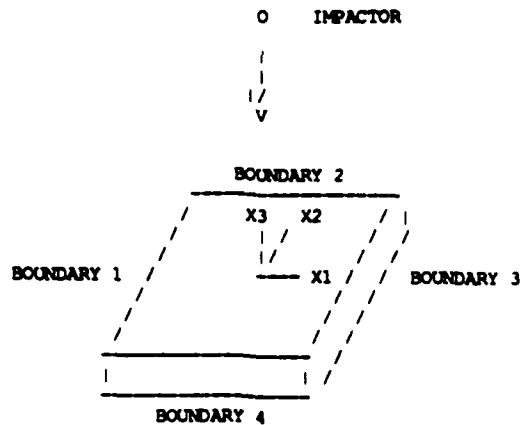
DO YOU WANT TO INPUT DATA FROM THE DATA FILE OR DO YOU WANT TO
INPUT DATA INTERACTIVELY ?
ENTER 0 FOR DATA FILE
ENTER 1 FOR INTERACTIVELY
0

```

```

----- PROBLEM STATEMENT:
----- THE PROBLEM IS SHOWN IN THE FOLLOWING FIGURE:

```



— IN THIS PROGRAM, THE FOLLOWING PARAMETERS ARE SPECIFIED BY THE USER:

- (1) IMPACTOR:
 - (A) MASS
 - (B) RADIUS
 - (C) DENSITY
 - (D) YOUNG'S MODULUS
 - (E) POISSON'S RATIO
 - (F) VELOCITY
- (2) COMPOSITE PLATE:
 - (A) GEOMETRY
 - (I) LENGTH
 - (II) WIDTH
 - (III) THICKNESS
 - (B) PLY-ORIENTATIONS
 - (C) MATERIAL PROPERTIES
 - (D) BOUNDARY CONDITIONS ON BOUNDARIES 1, 2, 3, AND 4
 - (I) SIMPLY SUPPORTED
 - (II) CLAMPED
 - (III) FREE

— OBJECTIVES:

- (1) TO FIND THE FOLLOWING INFORMATION:
 - (A) IMPACTOR
 - (I) VELOCITY AS A FUNCTION OF TIME
 - (II) DISPLACEMENT AS A FUNCTION OF TIME
 - (B) COMPOSITE PLATE
 - (I) CONTACT FORCE AS A FUNCTION OF TIME
 - (II) DISPLACEMENT AS A FUNCTION OF POSITION & TIME
 - (III) STRESSES AS A FUNCTION OF POSITION & TIME
 - (IV) STRAINS AS A FUNCTION OF POSITION & TIME
- (2) TO FIND THE SIZES AND LOCATIONS OF DAMAGES FROM THE FOLLOWING FAILURE CRITERIA:
 - (A) MATRIX CRACK CRITERION FROM CHOI & CHANG(1988)
 - (B) DELAMINATION GROWTH CRITERION FROM CHOI & CHANG(1990)

— ANALYSIS:

THE STRESS HISTORY IS CALCULATED USING A TRANSIENT FINITE ELEMENT METHOD FORMULATED ON THE BASIS OF THREE DIMENSIONAL ELEMENT MESHES.

—— INPUT INSTRUCTIONS:

WHENEVER YOU SEE THE QUESTION MARK " ? ",
YOU MUST INPUT THE DESIRED VALUE.

#ENTER THE NUMBER IDENTIFYING THIS RUN (A THREE DIGITS INTEGER) ?
116

#THE MESH OF THE PLATE IS 16 BY 12 BY 4 (LENGTH, WIDTH, THICKNESS).
DO YOU WANT TO CHANGE THE MESH ?
ENTER 0 FOR NO
ENTER 1 FOR YES
0

***** IMPACTOR *****

——THE PROPERTIES OF THE FOLLOWING IMPACTOR MATERIALS
ARE BUILT INTO THE PROGRAM:

	MAT. NO. 1:	MAT. NO. 2:
NAME	STEEL BALL	ALUMINUM BALL
MASS	0.842E-2	0.289E-2
RADIUS	0.635E-2	0.635E-2
DENSITY	7.85E3	2.70E3
YOUNG'S MODULUS	2.1E11	7.3E10
POISSON'S RATIO	0.3	0.3

#DO YOU WANT TO USE ONE OF THE ABOVE MATERIALS
AS IMPACTOR ?
ENTER 0 FOR NO
ENTER 1 FOR YES
0

#ENTER THE MASS (KG) ?
0.1610000E+00

#ENTER THE RADIUS (M) ?
0.6350000E-02

#ENTER THE DENSITY (KG/CUBIC M) ?
0.7850000E+04

#ENTER THE YOUNG'S MODULUS (PA) ?
0.2100000E+12

#ENTER THE POISSON'S RATIO ?
0.3000000E+00

——IMPACTOR'S VELOCITY:

#ENTER THE VELOCITY (M/SECOND) ?
0.5000000E+01

***** COMPOSITE PLATE *****

—— BOUNDARY CONDITIONS:

#ENTER THE BOUNDARY CONDITION ON BOUNDARY 1 ?
TYPE 0 FOR SIMPLY SUPPORTED
TYPE 1 FOR CLAMPED
TYPE 2 FOR FREE
1

#ENTER THE BOUNDARY CONDITION ON BOUNDARY 2 ?
TYPE 0 FOR SIMPLY SUPPORTED
TYPE 1 FOR CLAMPED
TYPE 2 FOR FREE
2

#ENTER THE BOUNDARY CONDITION ON BOUNDARY 3 ?
TYPE 0 FOR SIMPLY SUPPORTED
TYPE 1 FOR CLAMPED
TYPE 2 FOR FREE

1

ENTER THE BOUNDARY CONDITION ON BOUNDARY 4 ?
 TYPE 0 FOR SIMPLY SUPPORTED
 TYPE 1 FOR CLAMPED
 TYPE 2 FOR FREE

2

```

*****
*
*   REFERRING TO THE FIGURE SHOWN ABOVE, WE DEFINE THE
*   FOLLOWING:
*   (1) THE LENGTH OF THE PLATE IS IN THE X1-DIRECTION
*   (2) THE WIDTH OF THE PLATE IS IN THE X2-DIRECTION
*   (3) THE FIRST PLY IS THE ONE CLOSEST TO THE IMPACTOR
*   (4) THE PLY ORIENTATION IS DEFINED TO BE POSITIVE IN
*       THE COUNTERCLOCKWISE DIRECTION FROM THE X1-AXIS
*       WHEN LOOKING DOWNWARD FROM THE DIRECTION OF THE
*       IMPACT
*
*****

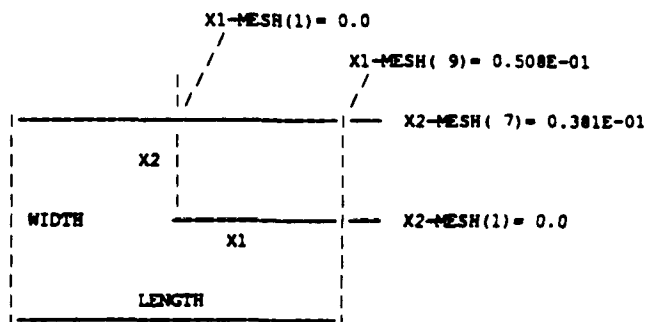
```

—— GEOMETRY:

ENTER THE LENGTH OF THE PLATE (M) ?
 0.1016000E+00

ENTER THE WIDTH OF THE PLATE (M) ?
 0.7620000E-01

***** COORDINATES OF THE MESH OF THE PLATE *****



—— THE COORDINATES OF THE MESH OF THE PLATE
 (X1 AND X2 DIRECTION) ARE INPUT BY THE USER.
 —— PLEASE INPUT THE VALUES OF X1-MESH AND X2-MESH.

***** X1 COORDINATE *****
 X1-MESH(1) = 0.0; ; ; X1-MESH(9) = LENGTH/2 = 0.508E-01

X1-MESH(1) = 0.0 (CENTER OF THE PLATE)
 ENTER THE VALUE OF X1-MESH(2) ? (POSITIVE REAL NUMBER)
 0.3175000E-02
 ENTER THE VALUE OF X1-MESH(3) ? (POSITIVE REAL NUMBER)
 0.6350000E-02
 ENTER THE VALUE OF X1-MESH(4) ? (POSITIVE REAL NUMBER)
 0.9525000E-02
 ENTER THE VALUE OF X1-MESH(5) ? (POSITIVE REAL NUMBER)
 0.1270000E-01
 ENTER THE VALUE OF X1-MESH(6) ? (POSITIVE REAL NUMBER)
 0.1905000E-01
 ENTER THE VALUE OF X1-MESH(7) ? (POSITIVE REAL NUMBER)
 0.2540000E-01
 ENTER THE VALUE OF X1-MESH(8) ? (POSITIVE REAL NUMBER)
 0.3810000E-01
 X1-MESH(9) = 0.508E-01 (RIGHT EDGE OF THE PLATE)

***** X2 COORDINATE *****
 X2-MESH(1) = 0.0; ; ; X2-MESH(7) = WIDTH/2 = 0.381E-01

X2-MESH(1) = 0.0 (MIDDLE OF THE PLATE)
 ENTER THE VALUE OF X2-MESH(2) ? (POSITIVE REAL NUMBER)
 0.3175000E-02

ENTER THE VALUE OF X2-MESH(3) ? (POSITIVE REAL NUMBER)
 0.6350000E-02
 ENTER THE VALUE OF X2-MESH(4) ? (POSITIVE REAL NUMBER)
 0.9525000E-02
 ENTER THE VALUE OF X2-MESH(5) ? (POSITIVE REAL NUMBER)
 0.1270000E-01
 ENTER THE VALUE OF X2-MESH(6) ? (POSITIVE REAL NUMBER)
 0.2540000E-01
 X2-MESH(7) = 0.381E-01 (TOP EDGE OF THE PLATE)

```

.....
*
*   DEFINITION OF PLY PROPERTIES:
*
*   EXX --- LONGITUDINAL YOUNG'S MODULUS (PA)
*   EYY --- TRANSVERSE YOUNG'S MODULUS (PA)
*   VXY --- POISSON'S RATIO IN THE X-Y DIRECTION
*   VYZ --- POISSON'S RATIO IN THE Y-Z DIRECTION
*   GXY --- SHEAR MODULUS IN X-Y DIRECTION (PA)
*   H --- PLY THICKNESS (M)
*   RHO --- DENSITY (KG/CUBIC M)
*   ACR --- CRITICAL INDENTATION (M)
*
*   LT --- LONGITUDINAL TENSILE STRENGTH (PA)
*   LC --- LONGITUDINAL COMPRESSIVE STRENGTH (PA)
*   TT --- TRANSVERSE TENSILE STRENGTH (PA)
*   TC --- TRANSVERSE COMPRESSIVE STRENGTH (PA)
*   IS --- IOSIPESCU SHEAR STRENGTH (PA)
*
.....
  
```

THE PROPERTIES OF THE FOLLOWING MATERIALS ARE BUILT INTO
 THE PROGRAM (PA OR M OR KG/CUBIC M) :

MATERIAL NO. 1:	CFRP T300/976
MATERIAL NO. 2:	CFRP T300/934
MATERIAL NO. 3:	CFRP T300/N5208
MATERIAL NO. 4:	BFRP B(4)/N5505
MATERIAL NO. 5:	CFRP AS/3501
MATERIAL NO. 6:	GFRP E-GLASS/EPOXY
MATERIAL NO. 7:	KFRP KEV 49/EPOXY
MATERIAL NO. 8:	CFRTP AS4/PEEK

THE PROPERTIES ARE:

	MAT. NO. 1	MAT. NO. 2	MAT. NO. 3	MAT. NO. 4
EXX	1.56E11	1.45E11	1.81E11	2.04E11
EYY	9.09E09	9.99E09	1.03E10	1.85E09
VXY	0.228	0.30	0.28	0.23
VYZ	0.400	0.30	0.28	0.23
GXY	6.96E09	5.68E09	7.17E09	5.59E09
H	1.44E-4	1.59E-4	1.25E-4	1.25E-4
RHO	1.54E03	1.54E03	1.60E03	2.00E03
ACR	8.03E-5	8.03E-5	8.03E-5	8.03E-5
LT	1.52E09	1.78E09	1.50E09	1.26E09
LC	1.59E09	1.73E09	1.50E09	2.50E09
TT	4.45E07	5.51E07	4.00E07	6.10E07
TC	2.52E08	2.94E08	2.46E08	2.02E08
IS	3.56E07	3.29E07	6.80E07	6.70E07

	MAT. NO. 5	MAT. NO. 6	MAT. NO. 7	MAT. NO. 8
EXX	1.38E11	3.86E10	7.59E10	1.34E11
EYY	8.96E09	8.26E09	5.50E09	8.89E09
VXY	0.30	0.26	0.34	0.28
VYZ	0.30	0.26	0.34	0.28
GXY	7.10E09	4.14E09	2.30E09	5.10E09
H	1.25E-4	1.25E-4	1.25E-4	1.25E-4
RHO	1.60E03	1.80E03	1.46E03	1.61E03
ACR	8.03E-5	1.02E-4	8.03E-5	8.03E-5
LT	1.45E09	1.06E09	1.40E09	2.13E09
LC	1.45E09	6.10E08	2.35E08	1.10E09
TT	5.20E07	3.10E07	1.20E07	7.99E09
TC	2.06E08	1.17E08	5.30E07	2.00E08
IS	9.29E07	7.19E07	3.40E07	1.60E08

— YOU MAY USE THE PROPERTIES OF ANY OTHER COMPOSITE.

#DO YOU WANT TO ENTER THE PROPERTIES OF ADDITIONAL MATERIALS ?

ENTER 0 FOR NO

ENTER 1 FOR YES

0

```

.....
*
*   PLIES MAY BE ENTERED INDIVIDUALLY OR IN GROUPS.
*
*   THE FIRST PLY GROUP IS THE ONE CLOSEST TO THE IMPACTOR.
*   THE PLY ANGLE IS MEASURED FROM THE X1-AXIS (SEE FIGURE
*   ABOVE) IN THE COUNTERCLOCKWISE DIRECTION
*   (LOOKING DOWNWARDS FROM THE DIRECTION OF THE IMPACT).
*
*
*
.....

```

— SPECIFY THE PLY ORIENTATION OF THE PLATE.

FOR EXAMPLE, 15 LAYERS, 4 INTERFACES, 5 PLY GROUPS:

[0(3)/90(3)/0(3)/90(3)/0(3)]

[THETA1(N1)/THETA2(N2)/....]

#ENTER THE NUMBER OF LAYERS OF THE PLATE (INTEGER) ?

15

#ENTER THE NUMBER OF PLY GROUPS OF THE PLATE (INTEGER) ?

5

#ENTER THE NUMBER OF PLIES IN PLY GROUP NO. 1 (INTEGER) ?

3

#ENTER THE ORIENTATION IN PLY GROUP NO. 1 (DEGREE) ?

0.0000000E+00

#ENTER THE NUMBER OF PLIES IN PLY GROUP NO. 2 (INTEGER) ?

3

#ENTER THE ORIENTATION IN PLY GROUP NO. 2 (DEGREE) ?

0.9000000E+02

#ENTER THE NUMBER OF PLIES IN PLY GROUP NO. 3 (INTEGER) ?

3

#ENTER THE ORIENTATION IN PLY GROUP NO. 3 (DEGREE) ?

0.0000000E+00

#ENTER THE NUMBER OF PLIES IN PLY GROUP NO. 4 (INTEGER) ?

3

#ENTER THE ORIENTATION IN PLY GROUP NO. 4 (DEGREE) ?

0.9000000E+02

#ENTER THE NUMBER OF PLIES IN PLY GROUP NO. 5 (INTEGER) ?

3

#ENTER THE ORIENTATION IN PLY GROUP NO. 5 (DEGREE) ?

0.0000000E+00

— SINCE THE MESH OF THE PLATE IS 16 BY 12 BY 4
(LENGTH, WIDTH, THICKNESS), THERE ARE 4 GROUPS

THROUGH THE THICKNESS OF THE PLATE.

#DO YOU WANT ALL THE PLYS IN EACH GROUP
HAVE DIFFERENT ORIENTATIONS ?
ENTER 0 FOR NO
ENTER 1 FOR YES
1

#ENTER THE MATERIAL NUMBER GIVEN ABOVE TO SPECIFY THE
MATERIAL USED IN GROUP NO. 1 (INTEGER) ?
1

#ENTER THE NUMBER OF PLYS IN GROUP NO. 1 (INTEGER) ?
3

#ENTER THE PLY-ORIENTATION OF THE PLY NO. 1
IN GROUP NO. 1 (DEGREES) ?
0.0000000E+00

#ENTER THE PLY-ORIENTATION OF THE PLY NO. 2
IN GROUP NO. 1 (DEGREES) ?
0.0000000E+00

#ENTER THE PLY-ORIENTATION OF THE PLY NO. 3
IN GROUP NO. 1 (DEGREES) ?
0.0000000E+00

#ENTER THE MATERIAL NUMBER GIVEN ABOVE TO SPECIFY THE
MATERIAL USED IN GROUP NO. 2 (INTEGER) ?
1

#ENTER THE NUMBER OF PLYS IN GROUP NO. 2 (INTEGER) ?
4

#ENTER THE PLY-ORIENTATION OF THE PLY NO. 1
IN GROUP NO. 2 (DEGREES) ?
0.9000000E+02

#ENTER THE PLY-ORIENTATION OF THE PLY NO. 2
IN GROUP NO. 2 (DEGREES) ?
0.9000000E+02

#ENTER THE PLY-ORIENTATION OF THE PLY NO. 3
IN GROUP NO. 2 (DEGREES) ?
0.9000000E+02

#ENTER THE PLY-ORIENTATION OF THE PLY NO. 4
IN GROUP NO. 2 (DEGREES) ?
0.0000000E+00

#ENTER THE MATERIAL NUMBER GIVEN ABOVE TO SPECIFY THE
MATERIAL USED IN GROUP NO. 3 (INTEGER) ?
1

#ENTER THE NUMBER OF PLYS IN GROUP NO. 3 (INTEGER) ?
4

#ENTER THE PLY-ORIENTATION OF THE PLY NO. 1
IN GROUP NO. 3 (DEGREES) ?
0.0000000E+00

#ENTER THE PLY-ORIENTATION OF THE PLY NO. 2
IN GROUP NO. 3 (DEGREES) ?
0.0000000E+00

#ENTER THE PLY-ORIENTATION OF THE PLY NO. 3
IN GROUP NO. 3 (DEGREES) ?
0.9000000E+02

#ENTER THE PLY-ORIENTATION OF THE PLY NO. 4
IN GROUP NO. 3 (DEGREES) ?
0.9000000E+02

#ENTER THE MATERIAL NUMBER GIVEN ABOVE TO SPECIFY THE
MATERIAL USED IN GROUP NO. 4 (INTEGER) ?
1

#ENTER THE NUMBER OF PLYS IN GROUP NO. 4 (INTEGER) ?
4

#ENTER THE PLY-ORIENTATION OF THE PLY NO. 1
IN GROUP NO. 4 (DEGREES) ?

0.9000000E+02

ENTER THE PLY-ORIENTATION OF THE PLY NO. 2
IN GROUP NO. 4 (DEGREES) ?
0.0000000E+00

ENTER THE PLY-ORIENTATION OF THE PLY NO. 3
IN GROUP NO. 4 (DEGREES) ?
0.0000000E+00

ENTER THE PLY-ORIENTATION OF THE PLY NO. 4
IN GROUP NO. 4 (DEGREES) ?
0.0000000E+00

.....
*
* SUMMARY OF THE INPUT DATA *
*
*.....

IMPACTOR:
MASS = 0.16100E+00 KG
RADIUS = 0.63500E-02 M
DENSITY = 0.78500E+04 KG/(CUBIC M)
YOUNG'S MODULUS = 0.21000E+12 PA
POISSON'S RATIO = 0.30000E+00
VELOCITY = 0.50000E+01 M/SECOND

COMPOSITE PLATE:
BOUNDARY 1 IS CLAMPED
BOUNDARY 2 IS FREE
BOUNDARY 3 IS CLAMPED
BOUNDARY 4 IS FREE

GEOMETRICAL CONFIGURATION:
LENGTH = 0.10160E+00 M
WIDTH = 0.76200E-01 M

GROUP NO. 1 :
MATERIAL NUMBER = 1
PLIES NUMBER = 3
PLY-ORIENTATION OF NO. 1 PLY = 0.00000E+00 DEGREES
PLY-ORIENTATION OF NO. 2 PLY = 0.00000E+00 DEGREES
PLY-ORIENTATION OF NO. 3 PLY = 0.00000E+00 DEGREES

GROUP NO. 2 :
MATERIAL NUMBER = 1
PLIES NUMBER = 4
PLY-ORIENTATION OF NO. 1 PLY = 0.90000E+02 DEGREES
PLY-ORIENTATION OF NO. 2 PLY = 0.90000E+02 DEGREES
PLY-ORIENTATION OF NO. 3 PLY = 0.90000E+02 DEGREES
PLY-ORIENTATION OF NO. 4 PLY = 0.00000E+00 DEGREES

GROUP NO. 3 :
MATERIAL NUMBER = 1
PLIES NUMBER = 4
PLY-ORIENTATION OF NO. 1 PLY = 0.00000E+00 DEGREES
PLY-ORIENTATION OF NO. 2 PLY = 0.00000E+00 DEGREES
PLY-ORIENTATION OF NO. 3 PLY = 0.90000E+02 DEGREES
PLY-ORIENTATION OF NO. 4 PLY = 0.90000E+02 DEGREES

GROUP NO. 4 :
MATERIAL NUMBER = 1
PLIES NUMBER = 4
PLY-ORIENTATION OF NO. 1 PLY = 0.90000E+02 DEGREES
PLY-ORIENTATION OF NO. 2 PLY = 0.00000E+00 DEGREES
PLY-ORIENTATION OF NO. 3 PLY = 0.00000E+00 DEGREES
PLY-ORIENTATION OF NO. 4 PLY = 0.00000E+00 DEGREES

.....
*
* INTEGRATION TIME STEP *
*
*.....

THE APPROXIMATE TIME TO REACH THE MAXIMUM CONTACT FORCE IS:

TIME = 0.6E-3 SECONDS

IMPACT CONDITION IS:
IMPACTOR MASS: 0.16 KG

IMPACTOR VELOCITY: 5 M/SEC
PLATE THICKNESS: 0.0022 M

IT IS RECOMMENDED TO CHOOSE 120 TIME STEPS OF INTEGRATION FOR THE END OF CONTACT.
AS IMPACTOR MASS INCREASED OR PLATE BECAME LESS STIFFER, THE TIME TO REACH THE MAXIMUM CONTACT FORCE WOULD BE LONGER.

—TIME STEPS OF INTEGRATION:

IF NO,

ENTER THE TOTAL INTEGRATION TIME TO BE USED (INTEGER) ?
0.1200000E-02

```

#ENTER THE NUMBER OF TIME STEPS TO BE USED
  (INTEGER) ?
      100

```

—FOR THE PRESENT PROBLEM, WE HAVE:

FINAL TIME OF INTEGRATION = 0.1200000E-02 SECONDS
ONE TIME STEP = 0.1200000E-04 SECONDS

```

.....
*
*              OUTPUT
*
.....

```

—THE FOLLOWING OUTPUTS CAN BE GENERATED BY THIS CODE.

OUTPUT GROUP #1:

MATRIX CRACK IN EACH PLY AT ANY TIME
DELAMINATION AREA AND SHAPE ALONG THE ANY INTERFACE AT ANY TIME

OUTPUT GROUP #2:

CONTACT FORCE BETWEEN PLATE AND IMPACTOR AT ANY TIME
DISPLACEMENT OF THE IMPACTOR AT ANY TIME
VELOCITY OF THE IMPACTOR AT ANY TIME

OUTPUT GROUP #3:

DISPLACEMENT OF ANY POINT AT ANY TIME
VELOCITY OF ANY POINT AT ANY TIME
STRAINS OF ANY POINT AT ANY TIME
STRESSES OF ANY POINT AT ANY TIME

NOTE:

- 1) THE OUTPUT OF GROUP #3 MIGHT OCCUPY LARGE SPACES OF STORAGE. IF YOU DO NOT REALLY NEED THIS INFORMATION, THEN DO NOT ASK FOR IT TO BE CALCULATED.
- 2) WHEN INPUTTING THE PLY NUMBERS, THE FIRST PLY IS THE ONE THAT IS CLOSEST TO THE IMPACTOR.

—OUTPUT GROUP #1:

—MATRIX CRACK AND DELAMINATION SHAPE/AREA FROM THE FAILURE CRITERIA PROPOSED BY CHOI AND CHANG

THE OUTPUT OF DAMAGE SHAPE/AREA IS STORED AND CAN BE PRINTED FROM THE FILE "DAMAGE.DAT" AFTER THE RUNNING OF THE PROGRAM.

DO YOU WANT TO CALCULATE GROUP NO. 1 ?

ENTER 0 FOR NO
ENTER 1 FOR YES

***** MATRIX CRACK *****

—THE LAMINATED PLATE OF THIS PROBLEM HAS 5 PLY GROUPS.
THUS, MATRIX CRACK CRITERION WOULD BE APPLIED AT THOSE
5 DIFFERENT PLY GROUPS AT EACH TIME STEP.

***** DELAMINATION *****

—DELAMINATION IS ASSUMED TO OCCUR ALONG THE INTERFACE BETWEEN
TWO ADJACENT PLIES WHEN A MATRIX CRACK OCCURS WITHIN ONE OR BOTH
ADJACENT PLIES.

THE LAMINATED PLATE OF THIS PROBLEM HAS 4 INTERFACES.
THUS, DELAMINATION GROWTH CRITERION WOULD BE APPLIED AT THE
INTERFACE WHERE THE MATRIX CRACK CRITERION IS SATISFIED FOR ANY
ADJACENT PLIES.

—DELAMINATION IS ILLUSTRATED BY "*" AND UNDEAMAGE AREA IS REMAINED
WITH "." IN THE OUTPUT FILE DAMAGE.DAT

—IF THE PLATE IS SYMMETRIC WITH RESPECT TO THE X1 OR X2 AXIS,
THE DELAMINATION AREA AND SHAPE WOULD BE ALSO SYMMETRIC.
THEREFORE, ONLY HALF OR QUARTER PORTION OF THE PLATE IS NEEDED TO
CALCULATE THE DELAMINATION AREA AND SHAPE.

CHOOSE ONE OF FOLLOWING NUMBERS FOR DELAMINATION SHAPE AND AREA.

- (1) FULL SIZE
- (2) HALF SIZE
- (3) QUATER SIZE

#DO YOU WANT TO HAVE 1 OR 2 OR 3 ?

1

—FOR MOST OF CASES, DELAMINATIONS ARE CONFINED WITHIN THE CENTER
REGION OF THE PLATE. FOR THE CLOSER VIEW OF THE PREDICTED DELAMINATIONS
FROM THE SCREEN, YOU MAY ZOOM IN THE IS ONLY NEEDED TO APPLY
DELAMINATION GROWTH CRITERION LOCAL AREA BY CHOOSING SCALING
PARAMETER, R, FROM 0 TO 1. IF R=1, THE ORIGINAL SCALE.

#ENTER THE SCALE FOR DELAMINATION AREA CALCULATION (0< R <=1.0) ?
0.7000000E+00

—DELAMINATION AREA AND SHAPE WILL PRINTED DURING INTERMEDIATE TIME.

#AFTER HOW MANY TIME STEPS DO YOU WANT THE RESULTS
TO BE PRINTED ?
ENTER AN INTEGER

1

—AN EMPIRICAL CONSTANT (Da) IS NEEDED FOR DELAMINATION GROWTH
CRITERION.
RECOMMENDED CONSTANT Da FOR GRAPHITE/EPOXY T300/976 MATERIAL
SYSTEM IS 1.8.
CONSTANTS FOR THE OTHER MATERIAL SYSTEMS ARE NOT CURRENTLY AVAILABLE.
FOR FURTHER INFORMATION, CONTACT DR. CHANG AT THE ADDRESS GIVEN ON
THE FIRST PAGE.

#ENTER THE CONSTANT FOR DELAMINATION GROWTH CRITERION ?
0.1800000E+01

—OUTPUT GROUP #2:
—CONTACT FORCE, IMPACTOR DISPLACEMENT/VELOCITY

THE OUTPUT OF CONTACT FORCE, IMPACTOR DISPLACEMENT/VELOCITY
IS STORED AND CAN BE PRINTED FROM THE FILE
"JGDP2.DAT" AFTER THE RUNNING OF THE PROGRAM.

#DO YOU WANT TO CALCULATE GROUP NO. 2 ?
ENTER 0 FOR NO
ENTER 1 FOR YES

1

IF YES,
#DO YOU WANT TO CALCULATE THE CONTACT FORCE BETWEEN THE PLATE
AND THE IMPACTOR DURING THE CONTACT ?
ENTER 0 FOR NO
ENTER 1 FOR YES

1

#DO YOU WANT TO CALCULATE THE DISPLACEMENT OF THE IMPACTOR
DURING THE CONTACT ?
ENTER 0 FOR NO
ENTER 1 FOR YES
1

#DO YOU WANT TO CALCULATE THE VELOCITY OF THE IMPACTOR
DURING THE CONTACT ?
ENTER 0 FOR NO
ENTER 1 FOR YES
1

---OUTPUT GROUP #3:
---DISPLACEMENT, VELOCITY, STRAIN, AND STRESS OF THE PLATE
---REMINDER: DO NOT CALCULATE GROUP #3 UNLESS IT IS
NECESSARY BECAUSE THE OUTPUT MIGHT OCCUPY
MANY SPACES TO STORE.

#DO YOU WANT TO CALCULATE GROUP NO. 3 ?
ENTER 0 FOR NO
ENTER 1 FOR YES
1

IF YES,
***** DISPLACEMENT AND VELOCITY *****

---THE COORDINATES OF THE PLATE ARE:
-0.508E-01 (BOUNDARY 1) < X1 < 0.508E-01 (BOUNDARY 3)
-0.381E-01 (BOUNDARY 4) < X2 < 0.381E-01 (BOUNDARY 2)
-0.108E-02 (BOTTOM) < X3 < 0.108E-02 (TOP)

PLEASE ENTER COORDINATES WITHIN THESE LIMITS.

THE OUTPUT OF DISPLACEMENT/VELOCITY OF THE PLATE IS STORED
AND CAN BE PRINTED FROM THE FILE "3DDV.DAT"
AFTER THE RUNNING OF THE PROGRAM.

#DO YOU WANT TO CALCULATE THE DISPLACEMENTS AND VELOCITIES
IN THE PLATE ?
ENTER 0 FOR NO
ENTER 1 FOR YES
1

IF YES,
#AT HOW MANY POINTS DO YOU WANT THE DISPLACEMENTS AND
VELOCITIES TO BE CALCULATED ?
ENTER AN INTEGER
1

INPUT THE COORDINATES OF EACH POINT ONE BY ONE.

#ENTER THE X1-COORDINATE OF POINT NO. 1 ?
0.1000000E-03
#ENTER THE X2-COORDINATE OF POINT NO. 1 ?
0.1000000E-03
#ENTER THE X3-COORDINATE OF POINT NO. 1 ?
0.1000000E-05

THE DISPLACEMENTS AND VELOCITIES WILL BE PRINTED
DURING INTERMEDIATE TIME.

#AFTER HOW MANY TIME STEPS DO YOU WANT THE RESULTS
TO BE PRINTED ?
ENTER AN INTEGER
1

***** STRAINS AND STRESSES *****

---THE COORDINATES OF THE PLATE ARE:
-0.508E-01 (BOUNDARY 1) < X1 < 0.508E-01 (BOUNDARY 3)
-0.381E-01 (BOUNDARY 4) < X2 < 0.381E-01 (BOUNDARY 2)
-0.108E-02 (BOTTOM) < X3 < 0.108E-02 (TOP)

SINCE THE STRAINS AND STRESSES ARE NOT ALWAYS CONTINUOUS
THROUGH THE THICKNESS, THE PLY NUMBER (COUNTED FROM TOP)

MUST BE INPUT TOGETHER WITH THE X3-COORDINATE.

PLEASE ENTER COORDINATES WITHIN THESE LIMITS.

THE OUTPUT OF THE STRAINS OF THE PLATE IS STORED AND CAN BE PRINTED FROM THE FILE "3DSTRAIN.DAT" AFTER THE RUNNING OF THE PROGRAM.

THE OUTPUT OF THE STRESSES OF THE PLATE IS STORED AND CAN BE PRINTED FROM THE FILE "3DSTRESS.DAT" AFTER THE RUNNING OF THE PROGRAM.

***** STRAINS *****

#DO YOU WANT TO CALCULATE THE STRAINS ?
ENTER 0 FOR NO
ENTER 1 FOR YES
1

IF YES,
#AT HOW MANY POINTS DO YOU WANT THE STRAINS TO BE CALCULATED ?
1

INPUT THE COORDINATES OF EACH POINT ONE BY ONE.

#ENTER THE X1-COORDINATE OF POINT NO. 1 ?
0.1000000E-03
#ENTER THE X2-COORDINATE OF POINT NO. 1 ?
0.1000000E-03
#ENTER THE X3-COORDINATE OF POINT NO. 1 ?
0.1000000E-05
#ENTER THE PLY NUMBER IN WHICH THIS POINT IS LOCATED ?
8

THE STRAINS WILL BE PRINTED DURING INTERMEDIATE TIME.

#AFTER HOW MANY TIME STEPS DO YOU WANT THE RESULTS
TO BE PRINTED ?
ENTER AN INTEGER
1

***** STRESSES *****

#DO YOU WANT TO CALCULATE THE STRESSES ?
ENTER 0 FOR NO
ENTER 1 FOR YES
1

IF YES,
#AT HOW MANY POINTS DO YOU WANT THE STRESSES TO BE CALCULATED ?
ENTER AN INTEGER
1

INPUT THE COORDINATES OF EACH POINT ONE BY ONE.

#ENTER THE X1-COORDINATE OF POINT NO. 1 ?
0.1000000E-03
#ENTER THE X2-COORDINATE OF POINT NO. 1 ?
0.1000000E-03
#ENTER THE X3-COORDINATE OF POINT NO. 1 ?
0.1000000E-05
#ENTER THE PLY NUMBER IN WHICH THIS POINT IS LOCATED ?
8

THE STRESSES WILL BE PRINTED DURING INTERMEDIATE TIME.

#AFTER HOW MANY TIME STEPS DO YOU WANT THE RESULTS
TO BE PRINTED ?
ENTER AN INTEGER
1

===== END OF INPUT AND OUTPUT INSTRUCTION =====

PROGRAM STARTS RUNNING #####
TIME STEP= 1: TIME= 0.120000E-04 PROGRAM IS RUNNING
TIME STEP= 1: TIME= 0.120000E-04 PROGRAM IS RUNNING
TIME STEP= 2: TIME= 0.240000E-04 PROGRAM IS RUNNING

```

** THE OUTPUT OF THE CONTACT FORCE, IMPACT BODY
   DISPLACEMENT/VELOCITY IS STORED IN FILE "3DGP2.DAT"

** THE OUTPUT OF THE DISPLACEMENTS/VELOCITIES OF THE PLATE
   IS STORED IN FILE "3DDV.DAT"

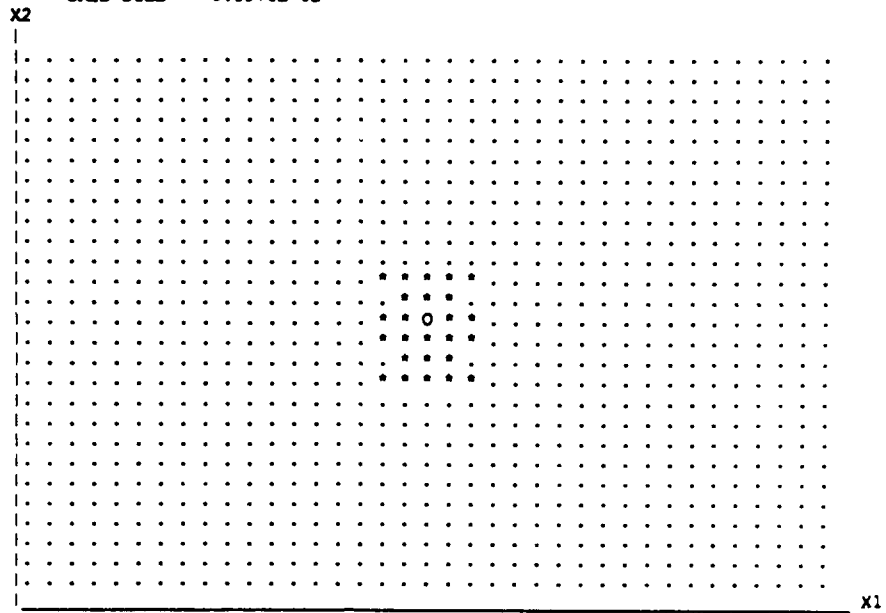
** THE OUTPUT OF THE STRAINS OF EVERY POINTS
   IS STORED IN FILE "3DSTRAIN.DAT"

** THE OUTPUT OF THE STRESSES OF EVERY POINTS
   IS STORED IN FILE "3DSTRESS.DAT"

```

*******END*******

DELAMINATION AREA AND SHAPE AT THE INTERFACE # 3
FULL SIZE (X1 * X2 = 0.7112E-01 * 0.5334E-01)
GRID SIZE = 0.1976E-02



DELAMINATION AREA AND SHAPE AT THE INTERFACE # 4
FULL SIZE (X1 * X2 = 0.7112E-01 * 0.5334E-01)
GRID SIZE = 0.1976E-02

